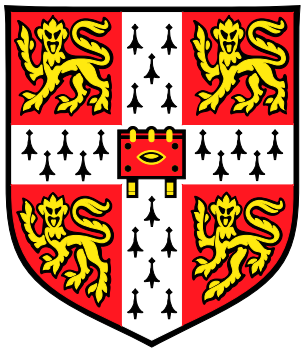

Freeze fracturing of elastic porous media

Ioanna Vlahou

This dissertation is submitted for the degree
of Doctor of Philosophy

Trinity College
and
Institute of Theoretical Geophysics
Department of Applied Mathematics and Theoretical Physics
University of Cambridge

This dissertation is the result of my own work and includes nothing which is the outcome of work done in collaboration except where specifically indicated in the text. No parts of this dissertation have been submitted for any other qualification.

Ioanna Vlahou

Freeze fracturing of elastic porous media

Ioanna Vlahou

Abstract

The physical motivation behind this thesis is the phenomenon of fracturing of rocks and other porous media due to ice growth inside pre-existing faults and large pores. My aim is to explain the basic physical processes taking place inside a freezing elastic porous medium and develop a mathematical model to describe the growth of ice and fracturing of ice-filled cavities.

There are two physical processes that can potentially cause high pressures inside a cavity of a porous medium. The expansion of the water by 9% as it freezes causes flow away from the freezing front and through the porous medium, resulting in a water pressure rise inside the cavity. Flow of water *towards* freezing cavities can occur during the later stages of freezing, when cavities are almost ice-filled, with a thin *premelted* film separating the ice from the medium. The pressure rise in this case is due to the flux of water into the cavities, which then freezes and increases the overall ice mass. The special geometry of a spherical cavity is initially considered, as a means of comparing how the different processes can contribute to pressure rise inside a cavity.

Having established that the expansion of water only contributes to the overall pressure rise in limited situations, I focus attention on the *premelting regime* and develop a model for the fracturing of a 3D penny-shaped cavity in a porous medium. Integral equations for the pressure and temperature fields are found using Green's functions, and a boundary element method is used to solve the problem numerically. A similarity solution for a warming environment is discussed, as well as a fully time-dependent problem. I find that the fracture toughness of the medium, the size of pre-existing faults and the undercooling of the environment are the parameters determining the susceptibility of a medium to fracturing. I also explore the dependence of the growth rates on the permeability and elasticity of the medium. Thin and fast-fracturing cracks are found for many types of rocks. I consider how the growth rate can be limited by the existence of pore ice, which decreases the permeability of a medium, and propose an expression for the effective "frozen" permeability.

An important further application of the theory developed here is the growth of ice lenses in saturated cohesive soils. I present results for typical soil parameters and find good agreement between our theory and experimental observations of growth rates and minimum undercoolings required for fracturing.

Acknowledgements

The work presented in this thesis would not have been possible without the support of my supervisor, Grae Worster. Throughout my doctoral years, he has taught me the importance of understanding the physical meaning behind the mathematics, and not losing track of the bigger picture when faced with problems or difficulties. I am grateful to him for his patience and encouragement.

Several other people have offered ideas and advice related to the work contained in this thesis. In particular, I would like to thank John Lister for being so generous with his time and helping me with many of my numerical and theoretical problems. Alexander Holyoake has been a constant help over the last four years, from solving technical issues, to encouraging me to improve my programming, and patiently listening whenever I had a problem. I am also grateful to John Willis, Colm Caulfield, Andrew Wells and Samuel Rabin for offering advice on different aspects of my work. My officemates Daisuke Takagi and Andrew Crosby, as well as all my friends and colleagues in DAMTP have made my time here productive and enjoyable.

I would like to thank the Engineering and Physical Sciences Research Council (EPSRC) for offering me a research grant to fund me through my studies, as well as Trinity College and DAMTP for their support.

Finally, this is a result of my family's encouragement and support, for which I am eternally grateful.

Contents

Chapter 1

Introduction

1.1 The geophysical problem

Large pressures can develop inside water-saturated porous media at sub-zero temperatures. These pressures can cause fracturing of pre-existing faults, degradation of rocks and soils, and displacement of the ground surface, and occur due to the solidification of the water inside the material. The results of such processes are of interest to both geologists and engineers. Frost-induced deformation of material can destroy building foundations, damage roads and statues as well as fracture water supplies and gas and oil pipelines. The importance of freezing in the development of landscapes is also widely recognized (Washburn, 1980). When soils freeze, segregated ice lenses consisting of ice blocks devoid of soil particles form, which cause upward movement of the ground above. While this process, called

Figure 1.1: *Circular patterned ground in Spitspergen (photo by B.Hallet). Circles are 1-2 metres in diameter.*

frost heave, continues over the course of weeks, objects such as large stones close to the surface are pushed upwards. In remote areas, the process can go on for months or years without much human intervention, and result in larger objects on the surface being organized in polygonal, circular or striped patterns, as seen in

Figure 1.2: *Exposed ice core of an eroded pingo (Schutter, 2004).*

figure 1.1. The phenomenon is called patterned ground and is a result of a combination of several processes, including particle self-organization and deformation of the soil during freezing (Kessler & Werner, 2003).

Other impressive features created by frost heave are pingos. Pingos are mounts with ice-filled cores, sometimes up to tens of metres high and hundreds of metres in diameter. There are two main types of pingo: the closed-system or hydrostatic pingos, and the hydraulic or open-system ones. The former are usually a result of a mass of water freezing inside a bounded space (e.g. with permafrost surrounding it) and pushing on the ground due to the water expanding. They are frequently found in locations of drained lakes which explains the existence of the water reservoir in the first place. The open-system pingos differ in that, as the name would suggest, they have an unlimited supply of water which flows towards the freezing front where it solidifies. The growing ice core deforms the upper surface and results in impressive features such as the one seen in figure 1.2. When the temperatures remain above melting point for a prolonged period of time, the

Figure 1.3: *Needle ice: millimetre thin ice emerging from the ground after freezing (Hilton Pond Center, 2000).*

ice can melt, resulting in collapse of the ground above.

When freezing occurs close to the surface, ice segregating immediately beneath the ground can be forced upwards through the pores, creating impressive columnar structures such as the one seen in figure 1.3. This phenomenon can have severe implications for agriculture, destroying vegetation, as well as engineering and geomorphology (Lawler, 1988).

Figure 1.4: *Large pothole in road (AA Ireland website, 2011).*

The effect of freezing is also evident in cities rather than just nature. We mentioned that buildings, stonework and pipelines suffer from freezing during the cold months. Another phenomenon most of us are familiar with is potholes on roads, which can be extremely hazardous to drivers and cyclists (see figure 1.4). During periods of sub-freezing temperatures, a pre-existing fault in the road, saturated with water, freezes over. More water is drawn from the surrounding soil, causing the ice to grow and push the overlying layer upwards. At this stage, the ice-rich soil is not tightly packed. When the temperatures rise above freezing again, either at the end of the winter or a warm day, the ice melts. In cases where the rehydration process is slow, this results in the soil consolidating, i.e. becoming tightly packed and hence the ground surface collapsing, creating a pothole.

The examples above demonstrate the importance of frost weathering and frost heave as geological phenomena that affect several aspects of our lives. The scientific motivation for studying these problems is equally fascinating and will be discussed in the following sections.

1.2 Frost heave

The geological features discussed above are all results of the pressures developed in water-saturated material during the solidification of water at sub-zero temperatures. In soils, the term *frost heave* is used to describe the upwards displacement of the ground surface, caused by the formation of particle-free ice blocks within the soil. Thin water films exist between the ice and the soil grains (Wettlaufer & Worster, 2006). This is an important feature of the processes discussed in this thesis and the physics behind this phenomenon is explained in chapter 2. Repelling intermolecular forces act through these water films between the ice and the soil. The balance between the resulting *disjoining pressure* and the other pressures acting on the system (overburden, hydrodynamic) can be used to describe the dynamics of deformation (Rempel *et al.*, 2004; Style *et al.*, 2011). As we will see, the maximum disjoining pressure is linearly related to the undercooling of the material, hence colder environments can produce larger forces. As more water freezes, *ice lenses* are formed, consisting of blocks of ice devoid of soil particles. The process by which the particles are rejected from the freezing front as it advances is described in Wettlaufer & Worster (2006) and is directly related to the existence of thin water films between the ice and the particle.

A common scenario during frost heave is the freezing of a block of material from above, resulting in a vertical temperature gradient. Ice lenses form perpendicular to the temperature gradient and they are separated by layers of soil which can be partially frozen. As ice lenses grow, they are pushed upwards, causing displacement of the upper surface. The overall amount of frost heave corresponds to the thickness and number of ice lenses, as can be seen in figure 1.5. If the solidification rate is slow enough, a single ice lens can form. Rempel *et al.* (2004) studied the rate of heaving at which single ice lenses grow, which is found to be a function of the temperature at their boundary.

1.2.1 Expansion resulting from solidification

As water freezes, it expands by about 9%. The volume change associated with solidification causes water to be pushed away from the freezing front. In a restricted environment, this can raise the pressure on the boundary as the water cannot escape. This phenomenon led scientists to assume that it was the expansion of water which developed high pressures in materials such as soils and caused deformation of the upper surface. Taber (1929; 1930) was first to challenge this idea, experimenting with freezing benzene in soils. Heave was observed, even though benzene contracts upon freezing. This showed that it is not the expansion of water that is responsible for heaving, a conclusion also supported by his findings that deformation of the ground surface substantially exceeds the relative expansion of the solidifying water. In addition to this, he was the first to observe flow of water towards the solidification front, rather than away from it as expansion would suggest. He also considered that frost damage requires an open system which allows for flow of unfrozen water towards the ice. This was further supported by Mellor (1970), who found that substantial amounts of water can remain unfrozen at -10° C, indicating the existence of continuous flow paths allowing the transport of water towards solidification fronts. Taber's work left scientists with two important questions to answer: Why does water flow towards the solidification front, i.e. from warmer to colder regions? And, what mechanism allows unfrozen water to exist between ice and soil particles?

1.2.2 Past studies

While the existence of unfrozen water films between the ice and the soil particles was established (first noted by Faraday, 1859; Tyndall, 1858; modelled by Gilpin, 1979), even at conditions where pressure melting isn't possible (Telford & Turner, 1963), scientists struggled to understand the exact physical nature of these films. Specifically, what couldn't be explained was how the films exerted positive pressure on the soil, causing heaving, while at the same time they attracted water from warmer regions, indicating a negative pressure relative to the bulk of water. This led some to suggest that water in thin films has different properties to water in bulk. The water films found in freezing soils are of the order of tens

of nanometres, which made it difficult to gather experimental evidence on water properties directly. Vignes-Adler (1977) suggested that the pressure tensor in thin water films is anisotropic, with an additional pressure component, the "extrastress", which acts only across the film and is interpreted as the disjoining pressure responsible for the deformation of the soil.

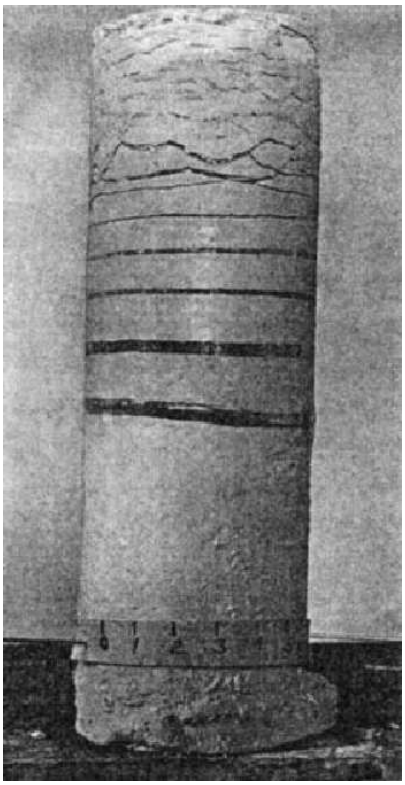

Figure 1.5: *A photograph, taken from Taber (1930), showing a series of dark lenses separated by lighter layers of partially frozen soil. The solidification process started from the top and proceeded downwards, with the warmest lens being the lowest. The surface is heaved by a distance equal to the combined thickness of the lenses. The scale bar at the bottom is given in centimetres.*

Also used to explain the flow of water from warm to cold regions was the idea that water transport in freezing soils is similar in nature to that in drying soils. Everett (1961) was the first to introduce the idea of the flow being driven by surface tension at ice–water interfaces. The same idea pervades the work of O'Neill & Miller (1985), Fowler (1989) and Fowler & Krantz (1994), who use the analogy with capillary wetting of dry soils to determine an expression for the pressure in the soil. This idea is consistent with the physics of the problem, as the

curvature is larger in colder regions and hence the pressure is lower. A slightly different explanation was suggested by Gilpin (1979) who simply assumed that the water in the thin films at solid–liquid interfaces experiences an attractive force by the solid boundary. This idea was used to develop a model for frost heave in soils in Gilpin (1980), where the flow of water towards the solidification front was attributed not to low pressure in the films but to gradients in the chemical potential. Rempel *et al.* (2004) found a qualitatively similar expression for the pressure but arrived at it through an integral force argument. In contrast, O'Neill & Miller (1985) assumed uniform ice pressure, an idea challenged by Rempel *et al.* who argued that ice can sustain large pressure gradients acting as an elastic medium. Although they recognized the wetting analogy in determining the volume fraction occupied by ice, they argued that it cannot be used to determine the pressure directly and showed that the curvature and surface energy play no role in driving the water flow. Instead, they claimed that it is the repelling forces between the ice and the rock that create the premelted films, while pushing the two substrates apart. The pressure in the water is lowered as a result of the forces tending to widen the gap, and more water gets sucked in.

Experimental results supporting the treatment of the thin water films in the same way as water in bulk (i.e. against assumptions of the films possessing an anisotropic stress tensor or other "strange" properties) were produced by Raviv & Klein (2002), who made direct measurements using atomic force microscopy and showed that water behaves as a Newtonian fluid down to scales of about two molecular diameters. Further experimental evidence supports Taber's results, with Mizusaki & Hiroi (1995) using helium in porous glass and Zhu *et al.* (2000) solidifying argon in silica powder. Even though helium and argon contract upon freezing, they both caused heave.

The concepts of flow of water towards the solidification front and the existence of thin water films at sub-freezing temperatures are now well understood, and can be used to model freezing in soils and rocks, as we will discuss in the next section. The work in this thesis is based on the idea that disjoining forces between the ice and the material give rise to thin *premelted* films, cause deformation of the soil or rock and draw more water in from warmer regions.

1.3 Frost fracturing of rocks

When water in rocks freezes, large pressures develop which can cause considerable damage to the rock. As discussed at the beginning of the introduction, this phenomenon has important consequences as it affects buildings, statues and pipelines, as well as contributing to landscape development.

It is natural to expect that frost fracturing is governed by similar mechanisms to frost heave. The connection is made through the assumption that ice-filled cavities in rocks play the role of ice lenses in soils. Similarly to soils, the early assumption about the cause of frost weathering of rocks was the expansion of water by 9% during solidification. This is the core of the volumetric-expansion model applied to porous rocks, and it implies that no fracturing can take place in a rock saturated with a fluid that contracts upon freezing. Many scientists used this model to try to explain frost weathering. As noted by Walder & Hallet (1985), several publications (see Embleton & King, 1975; Washburn, 1980; Tharp, 1983) considered volumetric expansion in sealed cracks the cause of damage to rocks. Although this is physically consistent, as the pressure build-up from the expansion would be considerable if the water had no means of escaping, it poses the question of how a sealed crack can be filled with water in the first place. The scenario would be relevant for a saturated rock being rapidly cooled from the outside from all sides, but its applications are limited.

The volumetric-expansion model is dependent on the idea that water is forced away from the solidification front and raises the pressure inside the medium, as the space that can be occupied by water is limited. This requires the medium to be completely (or, at least, considerably) saturated with water. If a large proportion of the pores were empty, the water would simply fill them and the pressure would be relaxed. Defining the saturation level as the percentage of the rock pores filled with water, and remembering that freezing water expands by about 9%, we see that a minimum saturation level of 91% would be required for fracturing to occur. This value hasn't been verified experimentally. For example, McGreevy & Whalley (1985) reported fracturing even for rocks only about 80% saturated but attributed the inaccuracy to heterogeneities in water concentration, which would make the accurate calculation of moisture levels difficult. Murton *et al.*

(2006) found that the saturation levels did not exceed 65% when the fracturing in their experiments began. Furthermore, the volumetric-expansion model predicts fracturing in bursts, and only during the freezing cycle, which isn't supported by experimental evidence (Murton *et al.*, 2006). As we saw in the previous section, the expansion of the water was shown to be unimportant by Taber (1929; 1930) during the freezing of soils. Taber (1950) extended his ideas to rocks, pointing our that several parameters, including pore space, particle size, permeability, availability of water and resistance to deformation, determined the extent of frost action in rocks.

The inability to support predictions of the volumetric-expansion model experimentally, coupled with advances in frost heave studies, where a deeper understanding of the governing processes was established and the idea of the water expansion causing fracturing was abandoned, led to the need for a new theory of frost fracturing. The migration of unfrozen water towards the solidifying centres of rocks was noted by Fukuda (1983), and strengthened the idea that parallels can be drawn with frost heave theory. More recent studies (Walder & Hallet, 1985; Murton *et al.*, 2006) have used the concept of ice-filled cavities acting as ice lenses. Disjoining (intermolecular) forces between the ice and the rock lower the pressure in unfrozen water films adjacent to the ice surface, which draws water in from the surrounding saturated medium. These disjoining forces cause the ice-filled cracks to grow. The difference between the process in soils and rocks lies in the way each medium deforms under the forces exerted by the ice: soil particles can be rejected from the solidification front if the freezing is slow enough. The cohesion of the rock means that the same is not possible. Instead, the pressure exerted on the rock deforms it elastically and can cause fracturing of the cavity if the stress at the tip is above a critical value. While in soils the pressure exerted by the ice is balanced by the overburden pressure, in rocks it is instead balanced by the elastic pressure of the medium. It is the relative magnitude of these two pressures that determines whether the cavity expands and the ice continues to grow.

The ideas discussed above were used by Walder & Hallet (1985) to develop a model for the fracture of a water-saturated rock during freezing. They recognized the importance of the flow of water towards the solidification front as well as the existence of thin films separating the ice and the rock. They discussed

how these films exert an "attractive force" on the pore water (hence the flow towards the ice front) and a disjoining pressure that pushes the ice and the rock apart. They showed that the fastest growth rate occurs at temperatures in the range -4 to $-15°$C as, in colder systems, the transport of water is limited owing to the large amount of pore ice reducing the permeability of the rock. For temperatures closer to 0°C, the maximum disjoining pressure (linearly related to the undercooling) is not large enough to cause the stress at the tip of the crack to exceed the "stress–corrosion" limit, the value above which Walder & Hallet predict fracturing. A similar fracture model was used by Murton *et al.* (2006) for their numerical simulations, coupled with a more complicated mass and heat transfer model.

While significant advances in the study of frost fracturing have been made, there is still a need for a more complete model. Matsuoka & Murton (2008) recently noted that the migration of water towards the freezing interface is now recognized as an important feature of frost cracking, and attributed it to flow induced by temperature gradients due to the suction developing in the unfrozen water in capillaries. As we saw, Rempel *et al.* (2004) have shown that the water flow is due to the disjoining pressure caused by intermolecular forces acting in the thin premelted film separating the ice and the rock. While their work was applied to soils, the same principles hold for freezing rocks. This idea will be further explored in this thesis and the pressure balance across the premelted films will form the basis of our work. The liquid pressure field can be related to the time evolution of the cavity, meaning that the propagation rate can then be directly determined through the pressure balance. In contrast, the two (different) growth laws for the fracturing of a crack used by Walder & Hallet (1985) and Murton *et al.* (2006) are based on empirical data, and they are required to close the system as subcritical fracturing is predicted for a range of tip stresses. Murton *et al.* discussed the limitations of the empirical growth law and recognized the need for a more fundamental model of fracturing. Our aim is to develop a model coupling the linear elastic behaviour of the medium with the water transport equations through the balance of pressures across the premelted film, using fracture mechanics to determine the behaviour of the crack tip. This will provide a theoretical model for the fracturing of a crack due to freezing based on fundamental physical ideas, without the need for empirical observations.

While the work presented in this thesis is predominantly applied to rocks, which exhibit approximately elastic behaviour under stress, recent work indicates that similar arguments can be used to model the growth of ice lenses in soils and colloidal suspensions, which also demonstrate cohesive properties when water-saturated. Recently, Style *et al.* (2011) developed a theory for ice lens growth which, unlike Rempel *et al.* (2004), does not require a frozen fringe and uses linear elasticity and fracture mechanics to describe the "crack-like" behaviour of ice lenses. This new approach is similar to ours and demonstrates how the work presented here can be used to describe the freezing of an extensive range of materials.

Developing a model that can predict the deformation and fracturing of material under freezing, incorporating all the important physical effects, is also vital when it comes to understanding experimental data or field observations. Much experimental work has focused on the analysis of the parameters which determine the susceptibility of materials to frost degradation, but the lack of a rigorous model has made it difficult for findings to be explained accurately. For example, a lot of field observations were initially limited to studying temperature cycles and freezing rates, which were believed to be the important parameters determining the existence and amount of frost damage (for relevant studies see McGreevy, 1981). As relevant findings were discussed in the context of the volumetric-expansion model, fast freezing rates were thought to be necessary for damage to occur (Battle, 1960), since they would cause rapid freezing from the outside, effectively "sealing" the material, but these conclusions have not had much experimental support (McGreevy, 1981). Water content was also considered to be important (Mellor, 1970) due to the volumetric-expansion model requiring high levels of saturation to predict a pressure rise. Since the need for flow towards the solidification front was not captured by the volumetric-expansion model, the structure of the rock was not believed to be a defining feature of frost damage, and hence was frequently ignored during experimental work.

In the model developed in this thesis, we will show that it is the maximum value of undercooling rather than the rate of freezing which determines the maximum pressures applied on the medium. We hence mainly consider situations of constant background undercooling, although a warming environment is discussed in chapter 5. We also know that the saturation of the material is an important

factor, since water needs to flow towards the freezing interfaces in order for the pressure to increase. Material properties such as permeability and porosity also contribute to the flow of water, hence they need to be taken into account when studying the susceptibility of materials to frost damage. Finally, the ability of the medium to withstand pressures without failing is described by fracture mechanics through the fracture toughness parameter, which we will show to be just as important as the undercooling in determining the susceptibility of a material. Similarly to Walder & Hallet (1985), we will find that linear elasticity predicts cracks with small aspect ratios, usually around 10^{-3}. This means that, for a real medium like a clay pot, we do not expect to see a distribution of short, fat, ice-filled cracks, but rather a few thin, long ones, causing it to fracture from one end to the other. Of course, if complete fracturing has occurred (for example in a column of material like the one in figure 1.5), the ice can keep growing in thickness if the temperature remains low.

1.4 Structure of the thesis

The aim of the thesis is to develop a complete model for rock fracturing during freezing, coupling linear elasticity and fracture mechanics with fluid dynamics. We begin by discussing some background theory, including the dynamics of premelted films, in chapter 2. Chapter 3 uses a simple geometry for freezing inside a spherical cavity in a porous, elastic medium, and studies the balance of the different processes contributing to the pressure rise inside the cavity. We will find that there is a limited number of scenarios where expansion is important, with the main pressure contribution coming instead from premelting. In chapter 4, we develop the equations describing ice growth inside a penny-shaped crack. A simple analytic solution is developed which reveals some important physical balances and can be used to compare different numerical schemes. However, the growth rate cannot be determined when the supply of water is the only process limiting the fracturing. This indicates that the toughness of the material, i.e. its ability to withstand pressure without fracturing, needs to be taken into account. The full problem, which includes the fracture mechanics describing the toughness of the material, is addressed in chapter 5, and a similarity solution is found for a

special case of the environment warming according to a power law in time. While restricting the boundary conditions in this way limits the applicability of the results, the qualitative ideas we develop are extremely useful as we gain a deeper understanding of the dependence of fracturing on the different parameters of the problem. The full time-dependent problem is solved numerically in chapter 6 and the growth rate characteristics of a crack are analysed. The initial stage of ice build-up is also discussed, and the conditions required for a pre-existing fault to fracture are determined. Chapter 7 involves further analysis of the penny-shaped model, and a comparison with existing numerical data from other models. The susceptibility of different materials to frost-induced degradation is analysed. The model is also extended to include the effect of pore ice on the permeability of the medium, which can be important at low temperatures as it limits the water supply. Finally, we show how the model is suitable to describe ice lens formation in clays and soils.

Chapter 2

Background theory

The aim of this chapter is to introduce the main background ideas which govern the work presented in this thesis. The thermodynamics of the problem are discussed, and the equations which govern the freezing temperature and the heat release during solidification are derived. We also present the physics of the premelted films between rock and ice, which give us the pressure balance across them, as well as the equations for Darcy flow through the porous medium, which will be used to determine the liquid pressure field.

2.1 Thermodynamics

Classical thermodynamics can be used to describe the process of solidification, i.e. the change of state from liquid to solid. The melting/freezing point is defined

as the temperature at which the liquid and the solid phases can coexist. This temperature, T_m, is measured at a certain reference pressure p_m as it is affected by changes in pressure.

We first define some quantities that will be used to derive some basic equations relevant to the work in later chapters. The *specific enthalpy* H describes the energy of the system

$$H = U + pV, \tag{2.1}$$

where U is the *specific internal energy*, p the pressure and $V = \rho^{-1}$ the specific volume. Changes in the specific enthalpy H arise either from a change in the specific entropy S of the system or a change in pressure

$$dH = TdS + Vdp. \tag{2.2}$$

The specific energy available by the system for useful work is described by the specific Gibbs free energy

$$G = H - ST \tag{2.3}$$

hence a change in G can be expressed as

$$dG = dH - SdT - TdS = Vdp - SdT. \tag{2.4}$$

At a phase boundary in equilibrium, G is the same in the two phases, $G_s = G_l$. Hence, applying this at the reference state (T_m, p_m), equation (2.3) gives

$$H_l - H_s = (S_l - S_s)T_m \equiv \mathcal{L} \tag{2.5}$$

where $\mathcal{L}$ is the latent heat required to convert a unit mass of a solid into liquid at the melting temperature T_m.

The specific Gibbs free energy of the liquid, G_l, is equal to that of the solid, G_s, when the two phases coexist. Any change of temperature and pressure that preserves the phase coexistence, will have

$$dG_l = dG_s. \tag{2.6}$$

By considering small departures from a reference state (T_m, p_m) to a state that has (T, p_s) in the solid state and (T, p_l) at the liquid state (since the temperature

is continuous across the boundary), and using equation (2.4) we find

$$V_s(p_s - p_m) - S_s(T - T_m) = V_l(p_l - p_m) - S_l(T - T_m). \tag{2.7}$$

Re-arranging the expression above for $S_l - S_s$ and using the definition of the latent heat $\mathcal{L}$, we can re-write it as

$$\rho_s \mathcal{L} \frac{T_m - T}{T_m} = (p_s - p_l) + (p_l - p_m)\left(1 - \frac{\rho_s}{\rho_l}\right), \tag{2.8}$$

which is known as the Gibbs-Duhem equation (Reif, 1965). The densities of the solid and liquid state are ρ_s and ρ_l respectively. This equation describes the effect that a difference of pressures across the liquid–solid interface (first term on right-hand-side of equation) or a change from the reference pressure p_m (second term of right-hand-side of equation) have on the freezing temperature of a substance. Next, we look at how each of the two terms can cause a change in the freezing temperature.

2.1.1 Pressure melting

Across a planar interface the liquid and solid pressures are equal, $p_l = p_s = p$, say. In that case, equation (2.8) can be differentiated to show that

$$\frac{\mathrm{d}p}{\mathrm{d}T} = -\frac{\rho_s \rho_l \mathcal{L}}{T_m \, \Delta\rho}, \tag{2.9}$$

where $\Delta\rho = \rho_l - \rho_s$. This is known as the Clausius-Clapeyron equation and describes the effect of pressure on the melting temperature of a substance. Liquids that are denser in the solid state, i.e. contract upon freezing, solidify at a higher temperature under pressure because the pressure helps to hold the molecules together. However, water is special in that it expands when it freezes ($\rho_l > \rho_s$). An increased pressure, trying to compress it, causes it to remain in the liquid state. Similarly, increased pressure on ice causes melting by lowering the freezing temperature. This phenomenon is called *pressure melting*.

2.1.2 Curvature melting

A phase boundary with curvature $\kappa = \nabla.\mathbf{n}$, where $\mathbf{n}$ is the normal pointing into the liquid, experiences a difference in the pressure of the solid and liquid phase on either side of it, caused by the surface tension

$$p_s - p_l = \kappa\gamma, \tag{2.10}$$

where γ is the surface energy per unit area. If we take the reference pressure to be that in the liquid state in (2.8), i.e. $p_l = p_m$, we find

$$\rho_s \mathcal{L} \frac{T_m - T}{T_m} = \kappa\gamma, \tag{2.11}$$

which describes the effect of curvature on the melting temperature of a solid–liquid interface, known as the Gibbs-Thompson effect. While we will see that this is negligible in comparison to the effect of premelting (see section 2.1.3), it will play an important role in some cases described in chapters 5 and 6.

2.1.3 Premelting dynamics

The definition of the melting temperature T_m implies that at temperatures $T < T_m$, the bulk of a mass of substance remains in the solid state. The process of melting begins at the surface and here we will discuss how that can occur at $T < T_m$. We have already discussed the Gibbs-Thompson effect, where the freezing temperature is depressed on a curved surface and films of melt can exist on the surface at temperatures below the melting point T_m.

Similar effects can be observed on the boundaries of solids due to intermolecular interactions with the bounding material. The term *interfacial premelting* describes the existence of these microscopic films of melt on the surfaces of substances which are frozen in bulk, at temperatures below the melting temperature of the substance. These films can occur either at the vapour interface (surface melting), against a foreign substrate (interfacial melting) or at the interface between two crystallites of the same substance (grain-boundary melting) as described in Wettlaufer & Worster (2006). Interfacial premelting can be induced

by a variety of intermolecular forces. Here, we will consider the case of van der Waals forces as a specific example and concentrate on interfacial melting, where the solid is bounded by a foreign substrate, since this is the type of situation that we will be dealing with later.

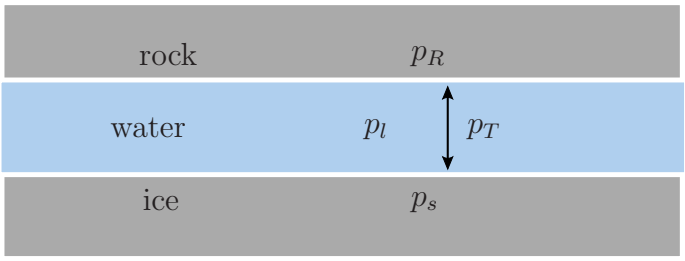

Figure 2.1: *Water fills the gap between ice and rock. The disjoining pressure p_T plus the water pressure p_l balance the solid pressure $p_s = p_R$.*

When a solid and a foreign substrate are separated by a thin film of melt of thickness h, non-retarded van der Waals forces between molecules give rise to a pressure between them of the form (see de Gennes, 1985)

$$p_T = \frac{\mathcal{A}}{6\pi h^3}. \tag{2.12}$$

The effective Hamaker constant $\mathcal{A}$ depends on the dielectric properties of all three materials involved and can have either sign. A negative sign leads to an attraction force and rupturing of any intervening liquid film. We are interested in the cases where $\mathcal{A}$, as defined in equation (2.12), is positive and hence the pressure between the solid and the substrate is disjoining. This pressure together with the liquid pressure p_l have to balance the solid pressure p_s

$$p_R = p_s = p_l + p_T, \tag{2.13}$$

as shown in figure 2.1.

The thickness of the premelted film increases with temperature and becomes macroscopically thick for $T \geq T_m$. In the van der Waals frame we are working in, an expression describing this dependence can be found using equation (2.8). We ignore pressure melting by setting $\rho_s = \rho_l$, in order to focus attention on the role of disjoining forces. Using this together with equations (2.12) and (2.13), we

then find that the equilibrium thickness of the premelted liquid film is given by

$$h = \left(\frac{\mathcal{A} T_m}{6\pi \rho_s \mathcal{L} \Delta T} \right)^{1/3}. \tag{2.14}$$

The Hamaker constant for rock–water–ice interfaces is in the region of $\mathcal{A} = 10^{-18} - 10^{-21}$ J (Watanabe & Flury, 2008). For an undercooling of $\Delta T = 1$ K, this results in a premelted film of thickness of the order of 10 nm.

This variation in the film thickness gives rise to many interesting phenomena where there is a temperature variation imposed. Examples include thermodynamic buoyancy and thermal regelation where a foreign particle in ice that is subjected to a uniform temperature gradient ∇T experiences a net force similar to a thermodynamic buoyancy force and moves up the temperature gradient (Rempel, Wettlaufer & Worster, 2001). Materials confined within capillary tubes premelt against the boundaries and when imposed to temperature gradients, they can cause large deformation over a small region towards the cold end of the capillary (Wettlaufer & Worster, 1995). Marangoni-like flows along thin films of water on ice surfaces are caused by the thermomolecular disjoining pressure and have been studied by Wettlaufer & Worster (2006).

2.1.4 Stefan condition

In a system with an unlimited supply of liquid, the freezing rate is simply determined by the temperature field, as temperature gradients determine the rate of transport of heat away from the solidification front. During a change of phase, energy called latent heat is released or absorbed by the object. When water solidifies, moving molecules become incorporated in the solid lattice and lose their entropy. This causes the release of latent heat of fusion which has to be transported away in order for the process to continue. This balance of heat is described by the Stefan condition (e.g. Worster, 2000), which states that the rate of release of latent heat per unit area is equal to the net heat flux away from the interface, i.e.

$$\rho_s \mathcal{L} V_n = \mathbf{n}.\mathbf{q}_l - \mathbf{n}.\mathbf{q}_s, \tag{2.15}$$

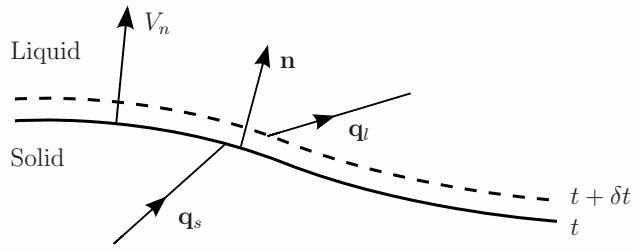

Figure 2.2: *Diagram explaining the balance of heat across the solidifying interface. The latent heat released per unit area in time δt is $\rho_s \mathcal{L} \delta t$ while the heat transported away is $(\mathbf{n}.\mathbf{q}_l - \mathbf{n}.\mathbf{q}_s)\delta t$.*

where $k_{s,l}$ is the thermal conductivity of the corresponding material and $\mathbf{q}_{s,l} = -k_{s,l}\nabla T$, evaluated on the freezing boundary, is the local heat flux vector in the solid and liquid phases respectively. The local rate of solidification is denoted by V_n as seen in figure 2.2, and $\mathcal{L}$ is the latent heat per unit mass.

2.2 Darcy flow

As we saw in the introduction, a lot of discussion has been based around the flow of water through the porous medium during frost heave or frost fracturing. While expansion predicts flow of water away from the solidification front, experiments have indicated that the flow is reversed, from the porous medium towards the ice (see chapter 1 for more details). In either case, it is important to understand the equations describing the flow through the rock or soil.

The flow through a porous medium is described by the equation derived by Darcy, relating the flux per unit area to the pressure gradient. Only a fraction of the total volume is free for water to flow through it, hence it makes sense to use an averaged value of the velocity. We use the symbol $\mathbf{u}$ for the Darcy flux, which has units of length per time, for consistency with the flow of water inside a cavity, as we will see in chapter 3. The real velocity of the water through the

pores can be related to the Darcy flux through the porosity ϕ of the medium

$$\mathbf{u}_{\text{pore}} = \frac{\mathbf{u}}{\phi}. \tag{2.16}$$

The Darcy equation for flow through the porous medium is

$$\mu\mathbf{u} = -\Pi\nabla p, \tag{2.17}$$

where p is the pressure, μ the viscosity and Π the permeability of the porous medium. The mass continuity is the second equation describing the flow

$$\nabla.\mathbf{u} = 0 \tag{2.18}$$

and, used together with equation (2.17), gives a useful equation for the pressure of the water

$$\nabla^2 p = 0. \tag{2.19}$$

As we are interested in obtaining an expression for the liquid pressure inside the premelted film, an important part of solving the problems presented in the next chapters will be to derive a solution to Laplace's equation (2.19) for the relevant geometries.

Chapter 3

The spherical cavity

As discussed in the introduction of this thesis, the physical mechanisms of frost fracturing are not very well understood and no complete mathematical model exists. In particular, while experiments (Taber, 1929; 1930; Mizusaki & Hiroi, 1995; Zhu *et al.*, 2000) have shown that the expansion of the freezing liquid is not a necessary condition for fracturing, several studies assumed that large pressures develop owing to the increasing volume of ice. In reality, both expansion and premelting can cause large pressures inside rocks. The aim of this chapter is to create a simple model that incorporates both features and allows us to compare the relative magnitude of their effects.

The two regimes are characterized by contrasting features. When expansion dominates, water flows away from the freezing front and into the medium. In contrast, when premelting is important, the flow reverses. We will attempt to

reproduce these features. We shall find that the effect of expansion is negligible in most cases. Therefore, when we want to restrict attention to the effect of disjoining forces we ignore expansion by setting the density of the ice ρ_s equal to the density of the water ρ_l. We concentrate on the physical mechanisms associated with disjoining pressure, modelling it based on van der Waals forces, and show that it has to balance the pressure difference between the ice and the water. The results of this study give us a useful insight into the mechanisms that are involved in the fracturing of rocks and how they contribute to the pressure fields within rocks and ice-filled cavities within them.

3.1 Governing equations

As a means to illustrate and understand the different physical mechanisms involved when ice forms inside a cavity of a porous, elastic rock, we start by considering the geometrically simple case of a spherical cavity of radius $R(t)$, as illustrated in Figure 3.1. We consider a system supercooled to some uniform temperature $T_\infty < T_m$, where T_m is the melting temperature of the ice measured at pressure $p_m = p_\infty$. We are interested in finding out how the radius of the solid ice and the pressure in the cavity evolve with time and also how the different parameters of the problem affect the solidification process.

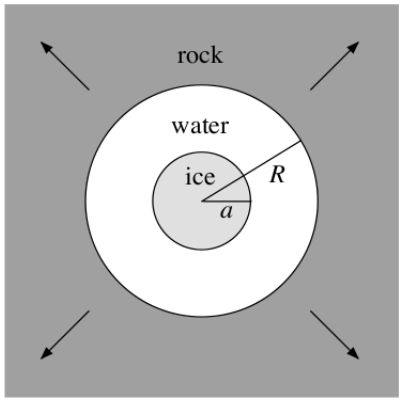

Figure 3.1: *Ice growing inside a water-saturated spherical cavity.*

As the water-saturated rock is supercooled, ice starts forming inside the cavity. We assume that the solidification begins from the centre of the supercooled

cavity and that the solid ice grows as a sphere of radius $a(t)$. As the water freezes it expands, causing water to flow away from the solidification front, as shown in figure 3.1. The water tries to escape the cavity through the porous medium in which the flow is controlled by the permeability. Flow through the porous medium requires a pressure gradient which can be substantial if the permeability of the medium is low. This results in a pressure increase in the cavity, which depresses the freezing temperature. This process describes how the flow through the porous medium controls the rate of solidification. We assume the flow in the cavity is slow, and the temperature field is quasi-steady (see Davis, 2001, pg. 26-29) so that

$$\nabla^2 T = 0. \tag{3.1}$$

The temperature is bounded at the origin and $T \to T_\infty$ as $r \to \infty$. The spherically symmetric solution to this is

$$T_s = T^I(t) \quad \text{and} \quad T_l = T_\infty + \frac{T^I(t) - T_\infty}{r}\, a(t), \tag{3.2}$$

where T_s, T_l are the temperature fields in the solid ice and the liquid water respectively, and T^I is the temperature at the solidifying interface.

The interface temperature is given by the Gibbs-Duhem relation (2.8), which describes the effect of pressure differences across the solid–liquid interface or departures from the reference pressure p_m on the freezing temperature. This can be re-arranged to give an expression for the temperature at the freezing interface

$$T^I(t) = T_m \left[1 - \frac{1}{\rho_s \mathcal{L}} \left(p_s(a,t) - p_l(a,t)\right) - \frac{\Delta\rho}{\rho_s \rho_l \mathcal{L}} \left(p_l(a,t) - p_m\right)\right], \tag{3.3}$$

where $\Delta\rho = \rho_l - \rho_s$ is the density difference between the two phases. For water, we have $\Delta\rho > 0$. The conservation of heat during solidification is described by the Stefan condition (see section 2.1.4). In the situation we are considering, taking into account the solution for the temperature field given by equation (3.2), the Stefan condition can be written in the form

$$\rho_s \mathcal{L} \dot{a} a = k_l (T^I - T_\infty). \tag{3.4}$$

The flow of the water through the porous medium is described by the equations

of Darcy flow and continuity (see section 2.2 for more details). The pressure field p_l then satisfies Laplace's equation in the porous medium

$$\nabla^2 p_l = 0 \quad \text{for} \quad r > R, \tag{3.5}$$

while $p_l \to p_\infty = p_m$ as $r \to \infty$ and is continuous across the cavity boundary $r = R(t)$. The Darcy flux $\mathbf{u}$ in the porous medium can be found in terms of the pressure field

$$\mu \mathbf{u} = -\Pi \nabla p_l, \tag{3.6}$$

where μ the viscosity and Π the permeability of the porous medium. The flow in the cavity is described by the Navier-Stokes equations but we expect it to be slow enough that the pressure gradient is negligible compared to that in the porous medium and hence we assume the cavity pressure to be constant. Since the problem is spherically symmetric, we can write $\mathbf{u} = u\mathbf{e_r}$. Mass conservation inside a sphere of radius $r > a$ can then be written as

$$\text{mass flux out of sphere} = -\text{rate of change of mass in sphere}, \tag{3.7}$$

or,

$$4\pi\rho_l r^2 u = \begin{cases} -\dfrac{d}{dt}\left[\dfrac{4\pi}{3}\rho_s a^3 + \dfrac{4\pi}{3}\rho_l(r^3 - a^3)\right] & a < r < R, \\ -\dfrac{d}{dt}\left[\dfrac{4\pi}{3}\rho_s a^3 + \dfrac{4\pi}{3}\rho_l(R^3 - a^3) + \phi\dfrac{4\pi}{3}\rho_l(r^3 - R^3)\right] & r > R, \end{cases} \tag{3.8}$$

where $\phi > 0$ is the porosity of the medium, i.e. the pore fraction. This gives an expression for the liquid velocity (volume flux per unit area) at any point in the cavity or the rock in terms of the radius of the solid ice:

$$u(r,t) = \begin{cases} \dfrac{\Delta\rho}{\rho_l}\dfrac{a^2\dot{a}}{r^2} & a < r < R, \\ \dfrac{\Delta\rho}{\rho_l}\dfrac{a^2\dot{a}}{r^2} - (1-\phi)\dfrac{R^2\dot{R}}{r^2} & r > R, \end{cases} \tag{3.9}$$

In the pores, the water pressure is related to the flow velocity via Darcy's equation

(3.6). The water pressure in the cavity is assumed constant and can be found from the value at the cavity boundary. This gives

$$p_l(r,t) = \begin{cases} \dfrac{\mu}{\Pi}\left[\dfrac{\Delta\rho}{\rho_l}\dfrac{a^2\dot{a}}{R} - (1-\phi)R\dot{R}\right] + p_m & a < r < R. \\ \dfrac{\mu}{\Pi}\left[\dfrac{\Delta\rho}{\rho_l}\dfrac{a^2\dot{a}}{r} - (1-\phi)\dfrac{R^2\dot{R}}{r}\right] + p_m & r > R. \end{cases} \tag{3.10}$$

The second term, involving $\dot{R}$, represents the opening of the cavity under pressure. Water flows freely through the area previously occupied by the porous medium, hence the water pressure is relaxed.

3.1.1 The premelting regime

When ice has almost filled the cavity, a thin premelted film of water exists between the ice and the rock. The distance from the grains is small enough for intermolecular forces between the two substrates to become important. These forces give rise to a disjoining pressure p_T, the magnitude of which depends on the thickness h of the water film between the ice and the rock. Here, as in section 2.1.3, we use non-retarded van der Waals forces to model this disjoining pressure, and write

$$p_T = \frac{\mathcal{A}}{6\pi h^3}, \tag{3.11}$$

where $\mathcal{A}$ is the Hamaker constant. The disjoining pressure contributes to the difference in the ice and water pressures across the freezing interface. The curvature of the ice also has an effect on the pressure difference, as described in section 2.1.2. The pressure balance across the solidifying interface can then be written as

$$p_i - p_l = p_T + \kappa\gamma, \tag{3.12}$$

where p_i is the ice pressure, κ is the curvature of the interface and γ is the ice–water surface energy.

As shown in figure 3.2, the ice boundary is highly curved when it is close to the grains, as the ice freezes into the pores of the medium. While the curvature

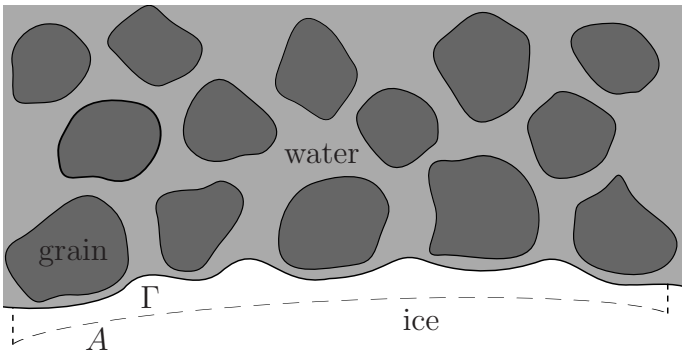

Figure 3.2: *A cross-section near the cavity-porous medium boundary. The ice is expanding into the free space of the porous medium, while it is separated from the grains by a thin film of premelted water. The ice boundary* Γ *is closed by the addition of the smooth surface* A*.*

κ will be a complicated function of position, we will see that it doesn't affect the disjoining forces applied on the rock. The net thermomolecular force on the rock, arising from intermolecular interactions, can be computed as

$$\mathbf{F}_T = -\int_\Gamma p_T \, d\mathbf{\Gamma} = -\int_\Gamma \left(\rho_s \mathcal{L} \frac{T_m - T^I}{T_m} - \gamma\kappa \right) d\mathbf{\Gamma} \tag{3.13}$$

(see Rempel *et al.*, 2001), where we have used the Gibbs-Duhem relation (3.3), ignoring the pressure melting term, to substitute for the pressure difference $p_s - p_l$ in the pressure balance (3.12). The surface Γ is the real surface of the ice. We can close Γ by adding the dashed surface of area A, as seen in figure 3.2, which we assume is at $r = R$. It can be shown (Rempel *et al.*, 2001) that the integral of the curvature over a closed surface vanishes. Defining the surface stress tensor as $\sigma^S \equiv \gamma(\mathbf{I} - \mathbf{nn})$ and applying the divergence theorem, we have

$$\int_S \gamma\kappa \, d\mathbf{S} = \int_S \nabla^S . \sigma^S \, d\mathbf{S} = \int_{\partial S} \mathbf{n}^S . \sigma^S \, d(\partial S) = 0, \tag{3.14}$$

since the integral is over zero length as the surface $S = \Gamma + A$ is closed. In the above expression we have taken $\nabla^S = (\mathbf{I} - \mathbf{nn}).\nabla$ to be the surface gradient operator, and $\mathbf{n}^S$ the normal to ∂S. We assume that the contribution of the curvature integral over the surface A will be negligible compared to that of Γ, which is the highly curved ice surface. This implies that the curvature term in equation (3.13) disappears. Then, implementing the divergence theorem for the

remaining term, we find

$$\mathbf{F}_T = -\frac{\rho_s \mathcal{L}}{T_m} \int_V \nabla(T_m - T^I)\, dV + \frac{\rho_s \mathcal{L}}{T_m} \int_A (T_m - T^I)\, d\mathbf{A}. \tag{3.15}$$

Since the temperature in the ice is constant, the first term on the RHS vanishes, while the second one simply gives

$$\mathbf{F}_T = \rho_s \mathcal{L} A \frac{T_m - T^I}{T_m} \hat{\mathbf{r}}. \tag{3.16}$$

The important conclusion here is that the net thermomolecular force is independent of the curvature and independent of the type and strength of interactions that give rise to the disjoining pressure p_T (see Rempel *et al.*, 2001). Moreover, it depends only on the approximated boundary A and not on the microscopically complicated surface Γ, hence we are justified to treat the ice–water–rock boundary as macroscopically smooth. We will ignore the curvature term in the pressure balance across the freezing front from now on and the effect of the curvature on the pressure applied on the rock will be discussed in section 3.2.1.

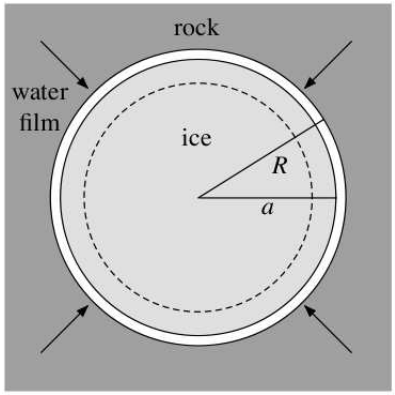

Figure 3.3: *The later stage, where disjoining forces are pushing the rock and the ice apart. Water flow has been reversed (contrast with figure 3.1).*

The disjoining forces between rock and ice push the two apart, causing the cavity to expand and more water to be drawn into the opening gap and freeze. This results in the reversal of the flow, as can be seen in figure 3.3 (contrast with figure 3.1). The pressure on the rock p_R is a combination of the disjoining forces

and the liquid pressure in the thin premelted film and hence is given by

$$p_R - p_l = p_T. \tag{3.17}$$

Since we are ignoring the curvature of the ice, the balance of pressures across the premelted film becomes

$$p_R = p_i \equiv p_s = p_l + p_T, \tag{3.18}$$

i.e. the ice pressure p_i and the rock pressure p_R are equal.

To model the deformation of the cavity under pressure we use isotropic linear elasticity with spherical symmetry which gives

$$p_s(R,t) = 4G\left(\frac{R}{R_0} - 1\right), \tag{3.19}$$

where R_0 is the initial radius of the cavity and G is the shear modulus of the material. The cavity starts expanding under the pressure that the growing ice is exerting on its boundary. As the gap opens up, the disjoining pressure is relaxed. More water flows towards the solidification front and freezes, increasing the pressure applied on the cavity. Ultimately, the system reaches an equilibrium where the disjoining pressure is balanced by the restoring force exerted by the deformed rock.

While the analysis of the pressure balance has been done for the late-time scenario, when the gap between the ice and the rock is very small, the pressure balance described by equation (3.18) holds throughout the solidification process. When the gap is large enough for disjoining forces to be negligible, i.e. $p_T \approx 0$, the only pressure applied on the rock is the pressure of the liquid, i.e. $p_R = p_l$. Across the freezing boundary we also have $p_i = p_l$, as we have ignored the effect of the curvature of the boundary. Therefore, the balance of pressures can be described by equation (3.18) at all times.

3.1.2 The dimensionless problem

We scale lengths with the initial cavity radius R_0 and temperatures with the undercooling temperature $\Delta T = T_m - T_\infty$. We also take temperatures and pressures

to be relative to the corresponding values at infinity so that the scaled values vanish at $r \to \infty$. A scale for velocities comes from the rate of solidification from equation (3.4),

$$u_0 = \frac{k_l \Delta T}{\rho_s \mathcal{L} R_0}. \tag{3.20}$$

A time scale can be written as $t_0 = R_0/u_0 = \rho_s \mathcal{L} R^2/k_l \Delta T$. The pressure scale comes from the left-hand side of the Gibbs-Thompson equation (2.8),

$$p^* = \frac{\rho_s \mathcal{L} \Delta T}{T_m} \tag{3.21}$$

and describes the pressure difference across an interface that causes depression of the freezing temperature by ΔT. We denote the scaled ice radius by $x(t) = a(t)/R_0$ while, to keep notation simple, we use the same symbols for the scaled versions of each variable. We can now also non-dimensionalize the flow velocity

$$u(r,t) = \begin{cases} \epsilon \dfrac{x^2 \dot{x}}{r^2} & x < r < R \\ \\ \epsilon \dfrac{x^2 \dot{x}}{r^2} - (1-\phi)\dfrac{R^2 \dot{R}}{r^2} & r > R \end{cases} \tag{3.22}$$

and the liquid pressure

$$p_l(r,t) = \begin{cases} \dfrac{x^2 \dot{x}}{\epsilon \tilde{\Pi} R} - \dfrac{1-\phi}{\epsilon^2 \tilde{\Pi}} R\dot{R} & x < r < R, \\ \\ \dfrac{x^2 \dot{x}}{\epsilon \tilde{\Pi} r} - \dfrac{1-\phi}{\epsilon^2 \tilde{\Pi}} \dfrac{R^2 \dot{R}}{r} & r > R, \end{cases} \tag{3.23}$$

where $\epsilon = \Delta\rho/\rho_l$ and $\tilde{\Pi}$ is the dimensionless parameter

$$\tilde{\Pi} = \frac{\rho_s^2 \mathcal{L}^2 \Pi}{\mu k_l \epsilon^2 T_m}, \tag{3.24}$$

which can be thought of as a dimensionless permeability. Values for parameters relating to water and ice can be found in table 3.1. The dimensionless heat balance equation is simply given by

$$x(t)\dot{x}(t) = T^I(t), \tag{3.25}$$

Parameter	Value
Latent heat, $\mathcal{L}$	334×10^7 cm^2·s^{-2}
Density of ice, ρ_s	0.92 g · cm^{-3}
Density of water, ρ_l	1 g · cm^{-3}
Thermal conductivity, k_l	2×10^5 g·cm · s^{-3}· K^{-1}
Dynamic viscosity, μ	1.79×10^{-2} g · cm^{-1}·s^{-1}
Melting temperature, T_m	273 K

Table 3.1: *Values for parameters relating to water and ice.*

while the interface temperature is given by the dimensionless version of equation (3.3)

$$T^I(t) = 1 - p_s + (1-\epsilon)p_l = 1 - \epsilon p_s - (1-\epsilon)p_T. \tag{3.26}$$

In the above expression, we have used the pressure balance (3.18) to derive the second equality. The disjoining and solid dimensionless pressures given by expressions (3.11) and (3.19) can be written in dimensionless terms as

$$p_T = \frac{F}{(R-x)^3} \quad \text{and} \quad p_s = E(R-1), \tag{3.27}$$

where $F = \mathcal{A}/p^* R_0^3$ is a dimensionless effective Hamaker constant and $E = 4G/p^*$ a dimensionless elastic modulus for the rock. The disjoining pressure p_T balances the pressure difference across the interface, $p_s - p_l$, which gives a first equation for the system:

$$\frac{F}{(R-x)^3} = E(R-1) - \frac{x^2\dot{x}}{\epsilon\tilde{\Pi}R} + \frac{1-\phi}{\epsilon^2\tilde{\Pi}}R\dot{R}. \tag{3.28}$$

The Gibbs-Duhem relation (3.26) together with the dimensionless heat balance (3.25) give a second equation for x and R

$$x\dot{x} = 1 - E(R-1) + \frac{(1-\epsilon)F}{(R-x)^3}. \tag{3.29}$$

3.2 The expansion regime

The initial stage of the process is the expansion stage, during which the solid ice is still small compared to the cavity size so there is no interaction between the ice and rock. While equations (3.28) and (3.29) will need to be solved numerically to describe the full problem, we can use some approximations to derive some important conclusions about this early regime analytically.

During the expansion stage, the disjoining forces are negligible, since the gap $R - x$ is large. Hence, we can ignore the $F/(R-x)^3$ term on the left-hand-side of equation (3.28) and the right-hand-side of equation (3.29). Then, we can eliminate the $E(R-1)$ term between the two equations to find

$$x\dot{x} + \frac{x^2\dot{x}}{\tilde{\Pi}R} - \frac{1-\phi}{\epsilon\tilde{\Pi}}R\dot{R} = 1. \tag{3.30}$$

The first term on the left-hand-side of equation (3.30) comes from the heat balance and represents the flow of latent heat away from the solidification front, while the second and third terms represent the pressure melting effect. They all affect the rate of solidification: the transport of latent heat away from the freezing front is necessary for the solidification to continue while a high pressure applied on the ice will cause depression of the freezing temperature and hence the process to slow down. The third term in particular expresses the relaxation in the liquid pressure which is caused by the opening of the cavity. For stiff materials like rocks, we expect the growth of the ice to be much faster than that of the rock, at least during the early stages of freezing when the ice is not close enough to the rock for the disjoining forces to be important, hence we can ignore the $\dot{R}$ term and take $R \approx 1$ for the rest of this section.

The first two terms are comparable when $x \sim \tilde{\Pi}R \sim 10^{15} \times \Pi$ cm^{-2}. Typical permeability values vary from 10^{-3} cm^2 for very permeable media such as highly fractured rocks to 10^{-12} cm^2- 10^{-15} cm^2 for rocks like limestone, granite etc. Even for very impermeable rocks (e.g. granite), the radius of the ice needs to be of the order of the radius of the cavity for the two contributions to be comparable, so the

pressure melting term is only important for large ice radii and small permeabilities. If we ignore the $x^2\dot{x}$ term, we end up with

$$x\dot{x} = 1 \quad \Rightarrow \quad x^2 - x_0^2 = 2t. \tag{3.31}$$

Hence, in most cases the solidification happens without experiencing an effect from the porous medium, and the ice grows proportional to $t^{1/2}$.

The pressure in the cavity during the expansion regime can be written as

$$p_{\text{expansion}} = \frac{x}{\epsilon(1+\tilde{\Pi})} \approx \frac{11x}{1 + 1.4 \times \Pi \times 10^{15}\text{cm}^{-2}}, \tag{3.32}$$

combining equation (3.23) with (3.30) and ignoring the $\dot{R}$ term. When $x \approx R$ we enter a regime not covered by the approximations made in this section. If we consider x large but not large enough for disjoining forces to become important, we can have dimensional pressures varying from around $10^{-4}p^*$ (e.g. in sandstone) to around $10p^*$ in granite. How large is p^*? For an undercooling of $\Delta T = 1^\circ\,\text{K}$ we have

$$p^* = \frac{\rho_s \mathcal{L} \Delta T}{T_m} \approx 11 \text{ atm}, \tag{3.33}$$

where we have taken the far-field pressure to be $p_m = 1\,\text{atm}$. Hence, the additional pressure in the cavity varies from 10^{-3} atmospheres, which is negligible, to 10^2 atmospheres which is more than sufficient to fracture a rock. This shows us that the expansion effect is very much dependent on the permeability of the medium. For a water-saturated granite for example, the flow of water away from the solidification front during the expansion stage can raise the pressure inside the cavity significantly.

3.2.1 Curvature effect and critical nucleation radius

We can include the effect of curvature on the freezing temperature in the Gibbs-Duhem equation (3.26) which becomes

$$T^I = 1 - \frac{\Gamma}{x} - \frac{x^2\dot{x}}{\tilde{\Pi}}, \tag{3.34}$$

where we have defined a dimensionless surface tension

$$\Gamma = \frac{2\gamma T_m}{\rho_s \mathcal{L} R_0 \Delta T}. \tag{3.35}$$

Combining this with the heat balance (3.25) we find

$$x\dot{x} = 1 - \frac{\Gamma}{x} - \frac{x^2\dot{x}}{\tilde{\Pi}} \quad \Rightarrow \quad \dot{x} = \frac{\tilde{\Pi}(x-\Gamma)}{x^2(x+\tilde{\Pi})}. \tag{3.36}$$

The expression for the pressure in the cavity will also change in a similar way

$$p_{\text{exp}} = \frac{x-\Gamma}{\epsilon(x+\tilde{\Pi})}. \tag{3.37}$$

The surface tension for the water–ice interface is $\gamma \approx 33\,\text{erg/cm}^2$ so $\Gamma = O(10^{-5})$ when $R_0 = 1\,\text{cm}$ and $\Delta T = 1\,\text{K}$. As before, the maximum pressure in the cavity occurs when $x = O(1)$. Since $\Gamma \ll 1$, the effect of curvature melting is negligible and the extra term can be ignored.

Equation (3.36) also shows that growth only occurs if $x > \Gamma$, i.e. there is a minimum radius of the ice nucleus, below which no ice growth occurs. In dimensional terms this condition becomes

$$a > a_{\text{min}} \equiv \frac{2\gamma T_m}{\rho_s \mathcal{L} \Delta T}. \tag{3.38}$$

The critical nucleation radius is independent of the permeability of the rock and the radius of the cavity hence it solely depends on the curvature of the sphere. The permeability of the porous medium doesn't determine whether ice nucleation is possible apart from in the special case $\Pi = 0$, i.e. when the rock is impermeable, where no ice can grow. This is a result of the volume increase occurring during solidification, owing to the density difference of ice and water, resulting in flow away from the solidification front. Since no water can flow through the porous medium when $\Pi = 0$, no freezing can occur.

3.3 Full results

We solve the full problem, governed by the system of differential equations (3.28) and (3.29) using Matlab's solver *ode15s*. This solver is chosen as it is suitable for stiff problems like the one here. Since the disjoining pressure term $F/(R-x)^3$ is acting only in a small region of the problem, there are two different scales and the required step to capture that behaviour is very small. A non-stiff solver would require a lot more steps to produce accurate results. For the following examples, we use a value of the Hamaker constant $\mathcal{A}$ a few orders of magnitude larger than the real one, as it helps makes the graphs clearer (a larger $\mathcal{A}$ means that the gap between ice and rock h is larger) and saves computational time. Smaller values of $\mathcal{A}$ require much smaller steps but do not alter the qualitative results. Typical values of the shear modulus are $G \approx 10 - 100\,\mathrm{GPa}$ for rocks like limestone or granite (see also section 7.2). This corresponds to a dimensionless elastic modulus of $E \approx 9 - 90 \cdot 10^3$. In the examples presented here, we have used a slightly smaller value of $E = 3000$ to make the deformation of the cavity more visible, but the qualitative conclusions remain the same.

Graphs 3.4-3.6 show results for the evolution of the radius of the ice and the cavity (left), and the liquid and solid pressures (right) plotted against time for three different types of rock. The first one, graph 3.4 shows results for a sandstone with permeability of 10^{-12} cm^2. There are three distinct regions. The first one extends up to about $t = 0.45$ and describes the expansion regime. We notice that the expansion of the cavity itself is negligible, while the evolution of the solid ice agrees very well with the $t^{1/2}$ behaviour (red line) predicted in the expansion section. There is no pressure difference across the solidification front since we are ignoring curvature effects and the disjoining forces are negligible (red dotted line). The important thing to note is that the maximum pressure during the expansion regime is much smaller than the maximum disjoining pressure. The second region is characterized by a very fast increase in the disjoining forces. The ice is now close enough to the cavity for intermolecular forces to become important and the solidification process has slowed down considerably since the ice is limited by the cavity boundary. Disjoining forces cause the cavity to expand and water to be sucked into the gap as we can see from the drop in the water pressure, which becomes negative. The third and last region is the recovery phase, where both the

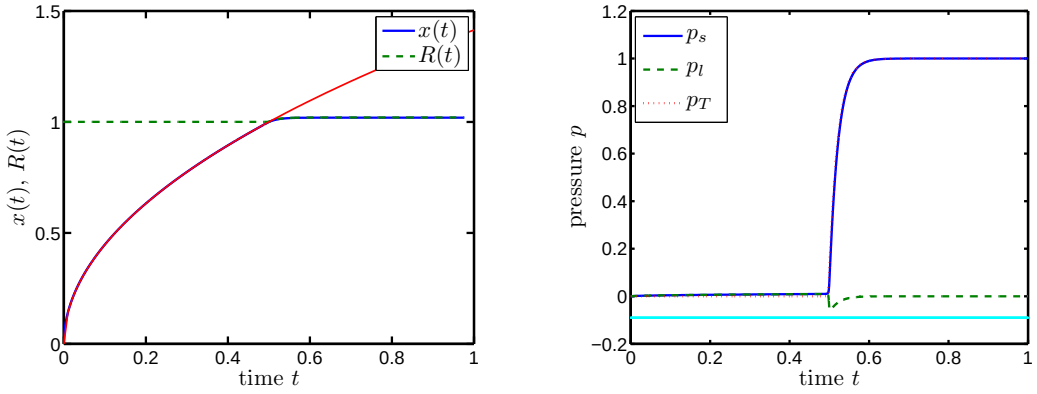

(a) (b)

Figure 3.4: *Results for the radii evolution (a) and pressure values (b) in relatively permeable porous rock, such as sandstone. (a) The radius of the cavity is represented by the green dashed curve, the radius of the ice by the blue solid curve and the red curve shows the approximate result from §3.2. (b) The blue curve is the solid pressure, the green dashed curve is the water pressure and the red dotted curve the disjoining pressure. The cyane straight line represents the vapour pressure. We have taken* $\tilde{\Pi} = 100$, $E = 3000$ *and* $\mathcal{F} = 10^{-10}$.

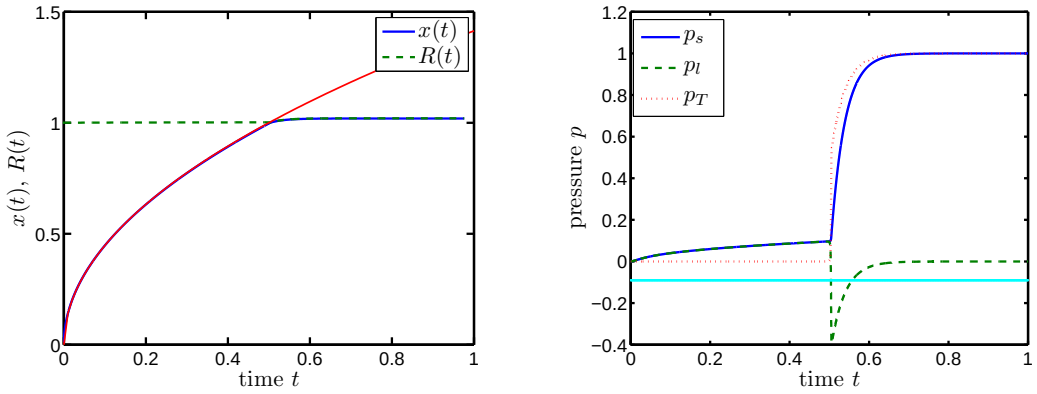

(a) (b)

Figure 3.5: *Results for the radii evolution (a) and pressure values (b) in limestone. (a) The radius of the cavity is represented by the green dashed curve, the radius of the ice by the blue solid curve and the red curve shows the approximate result from §3.2. (b) The blue curve is the solid pressure, the green dashed curve is the water pressure and the red dotted curve the disjoining pressure. The cyane straight line represents the vapour pressure. We have taken* $\tilde{\Pi} = 1$, $E = 3000$ *and* $\mathcal{F} = 10^{-10}$.

cavity and the ice keep growing until they reach (asymptotically) the equilibrium

state where the restoring force of the elastic rock balances the disjoining pressure and there is no water flow. Then, we have

$$R_{\text{eq}} = 1 + \frac{1}{E} \quad \text{and} \quad x_{\text{eq}} = 1 + \frac{1}{E} - F^{1/3}. \tag{3.39}$$

Similar results are found for the limestone, shown in figure 3.5, in which we see that the liquid pressure becomes even more negative. Since the pressures are taken relative to p_m, which has been scaled to 0, they are allowed negative values. Their dimensional values can't be negative though, as the minimum value is the water vapour pressure. This is something that isn't automatically accounted for by the mathematical problem presented so far. Let p_l' be the dimensionless water pressure and p_l the corresponding dimensional value. From the scalings of the problem we know that

$$p_l = p_l' p^* + p_m. \tag{3.40}$$

For example, we see that in the second graph in Figure 3.5, the water pressure gets as low as $p_l' = -0.3$, which in dimensional terms (see equation (3.33) too) is $p_l = -4.3\,\text{atm}$. The condition for non-negative dimensional pressures can be written as $\alpha p^* \leq p_\infty$ (practically, we take the vapour pressure to be zero), where $-\alpha$ is the minimum value that dimensionless pressure is allowed. For 1°C undercooling and reference pressure of 1 atm, we find that $\alpha \approx 0.09$. This is shown in both figure 3.4 and 3.5 as a straight cyane-coloured line. In the case of the limestone, where the calculations give a negative dimensional pressure, we assume that in reality, the pressure is equal to the vapour reference pressure, hence the water has vaporized, until pressure rises to positive values again. This is something that will affect the solid and disjoining pressures too, and requires separate analysis.

We also show the results for a very impermeable rock such as granite, with permeability of $10^{-15}\,\text{cm}^2$, in figure 3.6. The three regions are still distinct. What is interesting is that the largest pressure, and hence the biggest cavity deformation, comes from the expansion regime, which can be clearly seen in the pressure graph; the maximum pressure occurs before the intermolecular forces become important and is many times larger than the disjoining pressure. As the pressure increases, the ice growth deviates from the $t^{1/2}$ analytic solution more. This is because the high water pressure causes lowering of the freezing temperature and

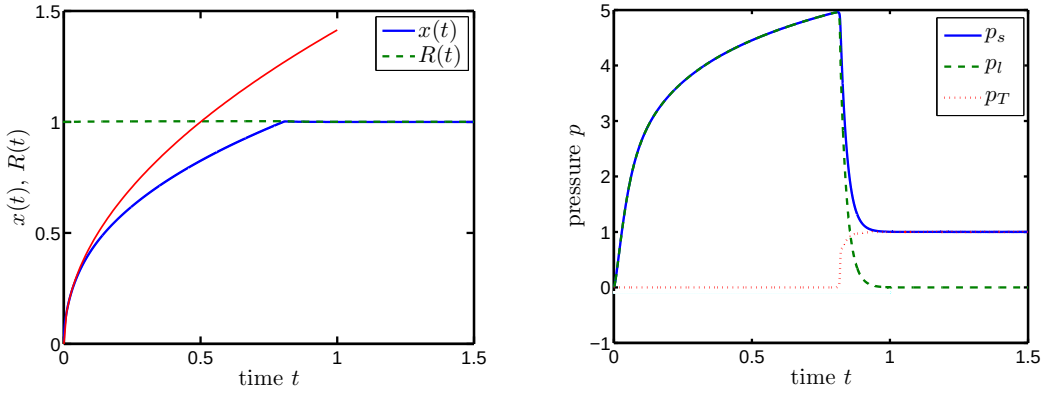

Figure 3.6: *Results for the radii evolution (a) and pressure values (b) in granite.(a) The radius of the cavity is represented by the green dashed curve, the radius of the ice by the blue one and the red line shows the approximate result from §3.2. (b) The blue line is the solid pressure, the green dashed line is the water pressure and the red dotted line the disjoining pressure. We have taken* $\tilde{\Pi} = 0.01$, $E = 3000$ *and* $\mathcal{F} = 10^{-10}$.

hence slows down the solidification process. The third regime keeps its recovering character, with the pressures relaxing to their equilibrium values and the water flow slowing down. An important point is that the water pressure never becomes negative, so there is no flow of water towards the solidification front. This is to show that only in limiting cases of very impermeable rocks is expansion important, while usually the maximum pressures are a result of the intermolecular forces between the ice and the rock.

In conclusion, in most cases we observe flow of water from the porous medium towards the solidification front. The only exception is the case of a very impermeable rock where the main contribution to the pressure build-up in the cavity comes from the expansion regime, due to the difficulty of the unfrozen water to escape the cavity during solidification. For relatively permeable rocks (see figure 3.4) the water pressure becomes negative and water flows towards the ice front. As we consider less permeable rocks, the minimum value of water pressure decreases. Then there is a regime where the calculations give unphysical negative dimensional pressures. In reality, when water reaches the minimum pressure (the vapour pressure), a vapour bubble will be created. The solidification cannot continue when the supply of water has stopped, hence no freezing or rock expansion occurs during that period. The solidification process can resume, tending to the

steady state shown in the third regime, when water from the medium has reached the freezing front. The timescale of this process will depend on the permeability of the medium as less permeable rocks limit the flow of water more. This regime requires a different approach, as the assumption of the ice–water–rock interface, and the subsequent pressure balance, break down. Further analysis of this phenomenon is beyond the scope of this thesis.

3.4 Conclusions

We have studied the process of water freezing inside a spherical cavity and how the growth of ice can create high pressures inside the cavity. We have identified the main features of the process: the expansion of the water when it freezes and the disjoining forces across a thin premelted film that develop when the ice has grown to be close enough to the rock. We have compared the effect that those two processes have on the pressure inside the cavity and how they depend on the permeability of the rock. This has shown that it is only in the case of very impermeable rocks, like granite, that expansion can raise the pressure enough to cause a fracture. For more permeable rocks, the water can escape the cavity easily during solidification without experiencing any influence of the porous medium. Therefore, the main rise in pressure comes from the premelting stage when the ice is very close to the rock. In this case the flow reverses and the water flows towards the solidification front. This is a result of disjoining forces that push the ice and the rock apart and cause the water pressure to drop. These disjoining forces can easily reach several atmospheres even for very small undercoolings, which indicates that they could be responsible for the fracturing of rocks.

Although the work presented here is done for a simple geometry, it provides insight into the processes that take place during the freezing of water-saturated rocks. It demonstrates the relative importance of expansion and premelting and shows that, in most cases, high pressures occur at the later stage where the ice has extended to the cavity boundary, therefore justifying our focusing future attention to ice-filled cavities. The idealized model developed here provides us with some important conclusions about the importance of the different interactions taking place inside the cavity. These conclusions can work as a basis for a mathematical analysis of more complicated and realistic geometries.

Chapter 4

The penny-shaped crack

We have so far studied ice growth inside a spherical cavity and the pressure build-up associated with the different processes taking place. We now have an understanding of the different balances between these processes which will be useful in our study of more complicated problems.

In order to develop a more realistic model of frost fracturing, we will have to look at more relevant geometries. Ice growth inside pre-existing faults in rocks, and the large pressures associated with it, will cause asymmetric growth of the faults, with the resulting crack likely to have two dimensions much larger than the third. Penny-shaped cracks were considered by Walder & Hallet (1985), who simply assumed a uniform pressure within each crack, resulting in elliptical profiles (see section 4.2.1). Complications arise if we attempt to account for curvature-induced melting of the ice, which can be an important effect, especially close to

the tip of the crack. We will attempt to address these points and consider the geometry of an isolated crack in more detail. Our aim is to develop a mathematical model combining fluid dynamics, thermodynamics and elasticity theory that will allow us to describe the processes taking place inside an ice-filled crack in order to make predictions of its shape and evolution.

In this chapter, we will develop the equations describing the fluid dynamics and linear elasticity of the problem, study some simple scalings that arise from the coupling of the two solid and liquid pressure fields and discuss numerical methods that can be used to tackle the problem further. We will focus on the balance of pressures and solve the problem for the propagation of a cavity under uniform pressure and only restricted by the water supply at the freezing front. We will find that the propagation rate cannot be determined by fluid dynamic arguments alone, and the dynamics of the crack need to be studied further. Despite this, many interesting features arise from the analytic solution obtained, and it is also used as a test for the two numerical methods developed.

4.1 Setting the problem

In an attempt to model this more complicated geometry, we will consider an axisymmetric, penny-shaped crack of radius $R(t)$ and small width $b(r,t) \ll R(t)$. The crack is considered to be inside an elastic porous rock that is large enough compared to the crack to be treated as infinite in extent. The rock is saturated with water that has been supercooled to a uniform temperature $T_\infty < T_m$, where T_m is the melting temperature of the ice measured at the reference pressure $p_m = p_\infty$. In this section, we assume that the crack and the rock remain isothermal. The latent heat produced during solidification has to be transported away from the freezing front in order for the process to continue. This requires a temperature gradient normal to the surface, and the transfer of energy is described mathematically by the Stefan condition (2.15). As we saw in section 3.1.1, when the solidification rate is dominated by the latent heat transfer, the growth of the ice behaves like $t^{1/2}$. This behaviour is seen in figures 3.4-3.6 for early times but, as soon as the ice is close enough to the cavity boundary for the disjoining pressure p_T to become important, the growth slows down dramatically.

This indicates that during the premelting stage, i.e. when the cavity is almost ice-filled, solidification is not fast enough for the latent heat transfer rate to have a controlling effect on it.

The study of spherical cavities in chapter 3 showed that the expansion of water doesn't contribute significantly to the build-up of pressure inside the cavity. We also saw that it is during the later phase of solidification, when the ice has almost filled the cavity, that the pressure is maximized. These two statements allow us to focus our attention on the period after most of the water in the crack is frozen and there is only a thin film of water between the ice and the rock. The thickness of the film, h, is constant as a result of the uniform temperature distribution inside the rock and crack. Although this requires the water to keep freezing in order to maintain constant h as the crack opens, we will neglect the expansion of water as we expect solidification to be slow, implying that the effect of expansion on the pressure exerted on the rock is even smaller than in the earlier expansion regime.

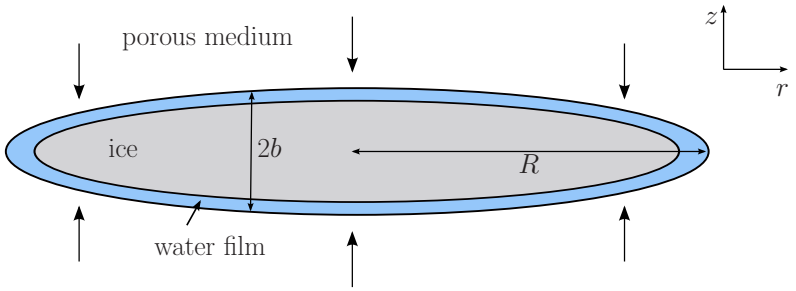

Figure 4.1: *An ice-filled cavity in a water-saturated medium. There is a thin water film of uniform thickness h between the ice and the rock.*

4.1.1 The elastic pressure field

We assume that the rock deforms linearly under load (as we did in chapter 3) and use linear elasticity to describe the pressure field within the solid. The equations

relating stress to displacement in cylindrical coordinates are (Sneddon, 1951)

$$\sigma_{rr} = (\lambda + 2G)\frac{\partial u_r}{\partial r} + \lambda\frac{u_r}{r} + \lambda\frac{\partial u_z}{\partial z}, \tag{4.1}$$

$$\sigma_{\theta\theta} = \lambda\frac{\partial u_r}{\partial r} + (\lambda + 2G)\frac{u_r}{r} + \lambda\frac{\partial u_z}{\partial z}, \tag{4.2}$$

$$\sigma_{zz} = \lambda\frac{\partial u_r}{\partial r} + \lambda\frac{u_r}{r} + (\lambda + 2G)\frac{\partial u_z}{\partial z}, \tag{4.3}$$

$$\sigma_{rz} = G\left(\frac{\partial u_r}{\partial z} + \frac{\partial u_z}{\partial r}\right), \tag{4.4}$$

where the subscripts represent components of the stress tensor σ and the displacement vector $\mathbf{u}$. The constant λ is Lamé's first parameter while G is the shear modulus. Solving the equations above can be reduced to solving the biharmonic equation (see Appendix A.1)

$$\nabla^4\Phi = 0, \tag{4.5}$$

where the function Φ is related to the stress field by

$$u_r = \frac{\lambda + G}{G}\,\Phi_{rz}, \tag{4.6}$$

$$u_z = \frac{\lambda + 2G}{G}\,\nabla^2\Phi - \frac{\lambda + G}{G}\,\Phi_{zz}. \tag{4.7}$$

There are several methods that can be used to find solutions for the pressure and displacement field using the function Φ. Different approaches are suited to different problems and their simplicity depends on the geometry of the problem and the boundary conditions. For the configuration here, we follow Spence & Sharp (1985) and assume that the crack has zero internal shear stress, i.e. $\sigma_{rz}(r, 0) = 0$. By symmetry, the problem for the disk-shaped cavity is equivalent to that for a half space $z > 0$ with prescribed pressure field within the circle $r < R$ and no normal displacement for $r > R$. Then, the expressions for the pressure $p(r, z)$ and the displacement $b(r)$ become (Sneddon, 1951, and see Appendix A.2)

$$p(r, z) = -\sigma_{zz}(r, z) = 2(\lambda + G)\int_0^\infty \xi^3 e^{-\xi z} B(\xi)(1 + \xi z) J_0(r\xi)\, d\xi, \tag{4.8}$$

$$b(r) = u_z(r, 0) = -\frac{\lambda + 2G}{G}\int_0^\infty \xi^2 B(\xi) J_0(r\xi)\, d\xi. \tag{4.9}$$

We have ignored the time dependence of the functions for simplicity of the notation as it only enters the equations as a parameter through the cavity thickness $b(r,t)$. The history of the crack shape is unimportant as it is only the current cavity shape that affects the pressure distribution at each time instant t. The function $B(\xi)$ is an unknown function to be determined from the boundary conditions while $J_0(r\xi)$ is the Bessel function of the first kind of order zero. By inverting the second integral and substituting for $B(\xi)$ in the expression for $p(r,z)$ we find that

$$p(r,z) = -m\frac{1}{r}\frac{d}{dr}\int_0^R \frac{\partial b}{\partial s}\,ds \int_0^\infty sre^{-\xi z}(1+\xi z)J_1(\xi r)J_1(\xi s)\,d\xi, \tag{4.10}$$

where $m = G/(1-\nu)$, and $\nu = \lambda/(2(\lambda+G))$ is the Poisson ratio for the elastic rock. We have used the boundary condition $b(r) = 0$ for $r > R$ to change the limits of the first integral in equation (4.10) from $[0,\infty)$ to $[0,R]$. On the undeformed reference boundary of the crack, given by $z = 0$, $r < R$, the elastic pressure $p_s(r,t)$ is given by (including the time dependence of R and b in the notation again)

$$p_s(r,t) = -\frac{G}{1-\nu}\int_0^{R(t)} M\left(\frac{r}{s}\right)\frac{\partial b(s,t)}{\partial s}\frac{ds}{s}, \tag{4.11}$$

where the kernel M is

$$M\left(\frac{r}{s}\right) = \begin{cases} \dfrac{2}{\pi}\dfrac{s^2}{s^2-r^2}E\left(\dfrac{r}{s}\right) & s > r \\ \dfrac{2}{\pi}\left[\dfrac{sr}{s^2-r^2}E\left(\dfrac{s}{r}\right) + \dfrac{s}{r}K\left(\dfrac{s}{r}\right)\right] & s < r \end{cases} \tag{4.12}$$

and the functions K and E are complete elliptic integrals of the first and second kind respectively.

4.1.2 Propagation of the tip

Generally, there are three basic types of crack. Here, we are interested in the first one, the mode-I crack, which corresponds to normal displacement of the crack walls under tensile stresses. This is the crack most commonly found in brittle

solids. Figure 4.2 is a sketch showing the typical configuration of a mode-I crack.

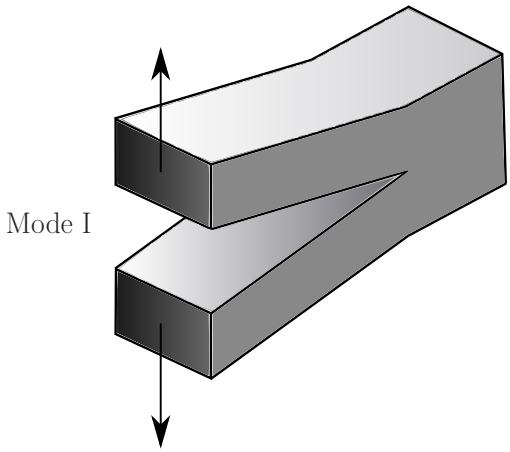

Figure 4.2: *A sketch of the mode-I opening.*

Linear elasticity predicts a singularity of the form $l^{-1/2}$ for the stress near at the tip of a crack, where l is the distance from the tip. For infinitesimally narrow cracks, the stress and displacement fields near the tip are given by Irwin's solutions (see Lawn, 1993)

$$\sigma_{ij} = \frac{K_I}{\sqrt{2\pi l}} f_{ij}(\theta) \tag{4.13}$$

$$u_i = \frac{K_I}{2m}\sqrt{\frac{l}{2\pi}} g_i(\theta) \tag{4.14}$$

where K_I is the mode-I stress intensity factor, depending only on the applied loading on the crack walls and the crack geometry. As in the previous section, $m = G/(1-\nu)$ where G is the shear modulus of the medium and ν is Poisson's ratio, while l and θ are the polar coordinates with the tip of the crack as the origin. The functions f and g describe the angular component of the spatial distribution of the field.

Linear elastic fracture mechanics (LEFM) predicts that the crack will propagate when the stress-intensity factor K_I reaches the critical value of the fracture toughness K, which is a material property. When the stress is below this critical value, i.e. $K_I < K$, no propagation occurs. When $K_I > K$, the pressure behind the propagating tip drops, which slows the propagation down. This indicates that

propagation occurs in the marginal state $K_I = K$. Using the Irwin equations, we can show (Savitski & Detournay, 2002) that the near-field of the crack is parabolic in shape

$$b \sim \frac{K}{m}\left[\frac{8(R-r)}{\pi}\right]^{1/2}, \quad \text{as} \quad r \to R. \tag{4.15}$$

An alternative expression for the stress-intensity factor can be derived by considering the effect that a given loading at the inner walls of a crack has on the stress at the tip (see Lawn, 1993, pg. 33). We assume that the load $p(r)$ is axisymmetric and continuously distributed along the inner walls. The stress-intensity factor produced by this load is then given by

$$K_I = \frac{2}{\sqrt{\pi R}}\int_0^R \frac{rp(r)}{\sqrt{R^2 - r^2}}\, dr. \tag{4.16}$$

When the crack is at the critical state $K_I = K$, the last two expressions are equivalent (see Rice, 1968).

4.1.3 The water pressure distribution

We now consider the pressure distribution of water inside the cavity and the porous medium. The flow of water through the pores is described by Darcy's equation

$$\mu\mathbf{u} = -\Pi\nabla p, \tag{4.17}$$

where μ is the dynamic viscosity of water and Π the permeability of the medium. We combine (4.17) with the mass continuity equation $\nabla.\mathbf{u} = 0$ to find that the water pressure p satisfies Laplace's equation $\nabla^2 p = 0$ everywhere apart from inside the crack. The pressure can hence be given in terms of a Green's function:

$$p = \frac{\mu}{4\pi\Pi}\int_{\text{disk}} \frac{q(r')}{|\mathbf{x} - \mathbf{r}'|}\, d\mathbf{r}' = \frac{\mu}{4\pi\Pi}\int_{\text{disk}} \frac{q(r')r'\, dr'\, d\theta'}{(r^2 + r'^2 - 2rr'\cos\theta' + z^2)^{1/2}}, \tag{4.18}$$

where $q(r)$ is the flux of water into the cavity

$$q(r) = -\frac{2\Pi}{\mu}\lim_{z\to 0}\frac{\partial p}{\partial z}. \tag{4.19}$$

The θ-integral can be expressed as an elliptic integral of the first type. We denote the water pressure on the boundary $z = b(r,t)$ as p_l. The boundary condition can be evaluated at $z = 0$ for simplicity, since the cavity opening b is small compared to the length of the crack. Then,

$$p_l(r,t) = \frac{\mu}{\pi\Pi}\int_0^R \frac{sq(s,t)}{r+s}\,K\left(\frac{2\sqrt{rs}}{r+s}\right)ds, \tag{4.20}$$

where K is the complete elliptic integral of the first kind.

Inside the cavity, water flows in the film between the ice and the rock. Assuming there is no flow in the θ direction, we write the velocities in the direction of r and z as v and w respectively. Because h is small, we can use lubrication theory to approximate the flow in the thin film. Since we are assuming a constant thickness h, we are ignoring the time-dependence of the flow using steady Navier-Stokes

$$\frac{\partial p}{\partial z} = 0 \quad \text{and} \quad \frac{\partial p}{\partial r} = \mu\frac{\partial^2 v}{\partial z^2}, \tag{4.21}$$

which give the solution

$$v = \frac{1}{2\mu}\frac{\partial p}{\partial r}(z-b)(z-b+h), \tag{4.22}$$

satisfying the no-slip condition at the rock and ice boundaries.

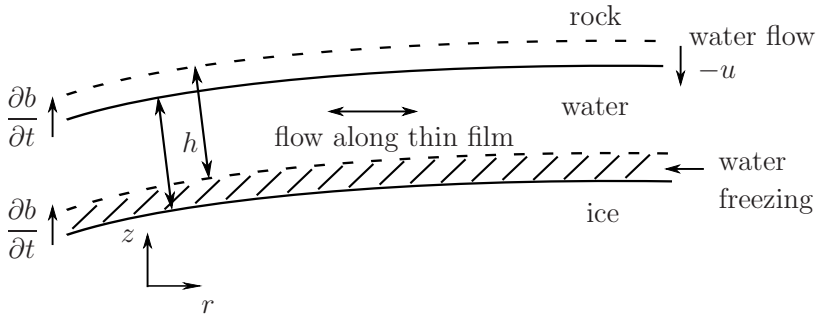

Figure 4.3: *A sketch of the premelted film, showing the different contributions to water flow in and out of it.*

Water flows inside the thin gap and freezes at the ice boundary. Since we have assumed that the gap h is uniform, the rate of growth of the ice is the

same as the rate of opening of the cavity, i.e. $\frac{\partial b}{\partial t}$. We can use mass conservation inside the thin film to deduce an equation for the rate of cavity opening $\frac{\partial b}{\partial t}$. The film changes as seen in figure 4.3, with the dashed curves representing the film after time δt. The bottom of the boundary moves as the water occupying $b - h < z < b - h + \delta b$ freezes. Since we have ignored the expansion of water as it freezes, this corresponds to a volume flux (per unit area) out of the gap of $\frac{\partial b}{\partial t}$ hence, at $z = b - h$, the velocity at the vertical direction is $w = -\frac{\partial b}{\partial t}$. Water flows into the gap from the porous medium as described by the Darcy equation (4.17) hence, at $z = b$, we have $w = u$. The mass continuity equation is

$$\frac{1}{r}\frac{\partial}{\partial r}(rv) + \frac{\partial w}{\partial z} = 0 \tag{4.23}$$

which, integrated from $z = b - h$ to $z = b$, gives an equation for the evolution of the cavity width $b(r, t)$

$$\frac{\partial b}{\partial t} + \frac{1}{r}\frac{\partial}{\partial r}\left(r\frac{h^3}{12\mu}\frac{\partial p_l}{\partial r}\right) = -u(b) = \frac{\Pi}{\mu}\frac{\partial p}{\partial z}\Big|_{z=b}, \tag{4.24}$$

where the second equality comes from Darcy's equation (4.17).

We estimate the sizes of the terms in the equation above, denoting the characteristic length scale by L and the pressure scale by P. The lubrication flow term on the left-hand side of equation (4.24) describes flow in the thin gap between the ice and the rock while the pressure term on the right-hand side represents the flow of water from the porous medium towards the solidification front. Using the pressure and length scales we find the ratio of these two terms to be

$$\frac{h^3}{12\mu}\frac{P}{L^2} : \frac{\Pi}{\mu}\frac{P}{L} = \frac{h^3}{12\Pi} : L. \tag{4.25}$$

The left-hand side of (4.25) is at most about 10^{-4} cm (since the thickness of the film h is of the order of 10 nm, see also section 2.1.3), while the size of a typical cavity will be several orders of magnitude larger. Hence, the flow through the porous medium dominates over the flow in the thin films. This allows us to ignore the lubrication flow term and to write equation (4.24) in the much simpler form

$$\frac{\partial b}{\partial t} = \frac{\Pi}{\mu}\frac{\partial p}{\partial z}\Big|_{z=b} \approx \frac{\Pi}{\mu}\frac{\partial p}{\partial z}\Big|_{z=0} = -\frac{1}{2}q(r, t). \tag{4.26}$$

The integral equation for p_l (4.20) can now be written in terms of $b(r,t)$

$$p_l(r,t) = -\frac{2}{\pi}\frac{\mu}{\Pi}\int_0^{R(t)} K\left(\frac{2\sqrt{rs}}{r+s}\right)\frac{\partial b(s,t)}{\partial t}\frac{s\,ds}{r+s}. \tag{4.27}$$

4.1.4 The pressure balance

We saw in chapter 2 that a difference in the solid–liquid pressure on a freezing surface can be caused by several effects. The presence of a foreign substance close to the boundary of the ice can cause a disjoining pressure acting across the film of water. A curved surface also causes a difference in the pressures across the freezing interface and depresses the freezing temperature. While studying the spherical model we found that the effect of the curvature of the surface of the spherical nucleus is unimportant (see section 3.2.1). Here, we are dealing with even smaller curvatures since the surface of the penny-shaped ice is much flatter than the spherical one. The only exception is at the tip of the crack, where the curvature becomes very large. This could affect the extent of the ice into the tip of the cavity, as we will discuss towards the end of section 4.2.1.

Close to the rock, we expect the ice to no longer be smooth but highly curved, extending into the pores of the medium, as described by figure 3.2 (see section 3.1.1). At the beginning of section 3.1.1 we showed why this effect is negligible and how we can treat the freezing front as a smooth surface, in a similar way to Rempel *et al.* (2001). The solid–liquid pressure difference hence must simply be balanced by the disjoining pressure

$$p_s - p_l = p_T. \tag{4.28}$$

The density difference between the solid and liquid phases is again ignored here, as in section 4.1.3. Its effect on the freezing temperature occurs through the phenomenon of pressure melting. A departure of the liquid pressure from the reference value causes a change in the freezing temperature, as described by the Gibbs-Duhem equation (2.8). In terms of p_s and p_l, the dimensionless interface temperature is given by

$$T^I = 1 - (p_s - p_l) + \epsilon p_l(x,t), \tag{4.29}$$

where $\epsilon = \Delta\rho/\rho_l$ and the second term on the right-hand-side describes the pressure-melting effect. The p_l terms can be combined to give $(1-\epsilon)p_l$ and, since the $\epsilon \approx 0.1$, we can approximate it as $(1-\epsilon)p_l \approx p_l$, i.e. taking $\epsilon \approx 0$. The interface undercooling (in dimensional terms) is therefore simply given by

$$\frac{\rho_s \mathcal{L} \Delta T}{T_m} = p_s - p_l. \tag{4.30}$$

4.2 Similarity solution

We begin by investigating a crack whose propagation is limited only by the ability of water to flow through the porous rock and feed the growing ice, rather than determined by considerations of the material fracture toughness.

In addition to the length and pressure scales L and P we define the time scale t^*. The balance of terms in the pressure balance equation (4.28) gives

$$m \sim \frac{\mu}{\Pi}\frac{L^2}{t^*} \;\Rightarrow\; L \sim \left(\frac{\Pi m}{\mu}\, t^*\right)^{1/2}. \tag{4.31}$$

There is no other constraint on the time scale so t^* simply is the elapsed time t. The radius of the cavity then propagates according to

$$R(t) = k\left(\frac{\Pi m}{\mu}\, t\right)^{1/2}, \tag{4.32}$$

where k is a constant of proportionality that has to be determined. Since the cavity shape scales with the elapsed time and there is no inherent time scale in the problem we can find a similarity solution in which

$$b(r,t) = k\left(\frac{\Pi m}{\mu}\, t\right)^{1/2} B(\eta) \tag{4.33}$$

where the similarity variable is scaled with the factor k so that the cavity extent $[0, R(t)]$ is mapped to $[0,1]$ and defined as

$$\eta = \frac{r}{R(t)} = \left(\frac{\Pi}{\mu}\frac{G}{1-\nu}\right)^{-1/2} \frac{r}{k t^{1/2}}. \tag{4.34}$$

We define the similarity pressure variables $P_s(\eta)$ and $P_l(\eta)$ according to $p_s(r,t) = mP_s(\eta)$ and $p_l(r,t) = mP_l(\eta)$ and the similarity problem becomes

$$P_s(\eta) = -\fint_0^1 M\left(\frac{\eta}{\sigma}\right) B'(\sigma)\frac{d\sigma}{\sigma}, \tag{4.35}$$

$$P_l(\eta) = -\frac{k^2}{\pi}\int_0^1 K\left(\frac{2\sqrt{\eta\sigma}}{\eta+\sigma}\right)\left[B(\sigma) - \sigma B'(\sigma)\right]\frac{\sigma\, d\sigma}{\eta+\sigma}, \tag{4.36}$$

$$P_s(\eta) - P_l(\eta) = P_T, \tag{4.37}$$

where P_T is the dimensionless disjoining pressure given by $P_T = p_T/m$.

4.2.1 An analytic solution

In the special case of a uniform liquid pressure along the thin premelted film we can find an analytic solution to the liquid pressure field. We saw earlier that the pressure field satisfies Laplace's equation

$$\nabla^2 p = 0, \tag{4.38}$$

with the boundary conditions now becoming

$$p = p_l = \text{constant} \;\text{ on }\; z = 0,\; r < R(t) = kc^{1/2}t^{1/2}, \tag{4.39}$$

where we define $c = \dfrac{\Pi m}{\mu}$, a group of parameters with dimensions of cm^2/sec. The parameter k is dimensionless and describes the propagation rate of the crack. The liquid pressure also decays at infinity

$$p \to 0 \;\text{ as }\; |r| \to \infty. \tag{4.40}$$

Since we have assumed that the liquid pressure is uniform along the crack, and as the undercooling is constant, we find that p_s = uniform too. We can solve Laplace's equation in this geometry by using oblate spheroidal coordinates $\sigma > 1$ and $-1 < \tau < 1$ where $r^2 = R^2\sigma^2\tau^2$ and $z^2 = R^2(\sigma^2-1)(1-\tau^2)$ and separating

variables. The Laplace operator is then given by

$$\nabla^2 = \frac{1}{R^2}\frac{1}{\sigma^2+\tau^2-1}\left\{\frac{\partial}{\partial\sigma}\left[(\sigma^2-1)\frac{\partial}{\partial\sigma}\right] - \frac{1}{\sigma}\frac{\partial}{\partial\sigma} + \frac{\partial}{\partial\tau}\left[(1-\tau^2)\frac{\partial}{\partial\tau}\right]\right\}. \quad (4.41)$$

If we write the pressure as a product of functions of the two variables σ and τ, $p = P(\sigma)Q(\tau)$, the boundary condition becomes

$$P(1)Q(\tau) = p_l, \quad (4.42)$$

hence $Q(\tau)$ is constant and its derivatives vanish. The differential equation for $P(\sigma)$ becomes

$$\sigma(\sigma^2-1)P'' + (2\sigma^2-1)P' = 0 \quad (4.43)$$

and the solution, after using the boundary conditions is

$$p = -\frac{2p_l}{\pi}\tan^{-1}\left(\sqrt{\sigma^2-1}\right) + p_l. \quad (4.44)$$

Then, the evolution equation for the cavity width is given by

$$\frac{\partial b}{\partial t} = -\frac{1}{2}q(r,t) = \frac{\Pi}{\mu}\frac{\partial p}{\partial z}\Big|_{z=0} = -\frac{2p_l}{\pi}\frac{\Pi}{\mu}\frac{1}{\sqrt{R^2-r^2}} \quad (4.45)$$

and, using the similarity variable $\eta = r/kc^{1/2}t^{1/2}$ and trying a similarity solution in the form

$$b = -\frac{2p_l}{\pi c^{1/2}}\frac{\Pi}{\mu}\frac{t^{1/2}}{k}\tilde{b}(\eta), \quad (4.46)$$

we find that the cavity has an elliptical shape $\tilde{b} = 2\sqrt{1-\eta^2}$, hence

$$b = -\frac{4p_l}{\pi m k^2}\frac{1-\nu}{G}\sqrt{R^2-r^2}. \quad (4.47)$$

The solid pressure p_s generated by the shape cavity described by equation (4.47) can now be calculated by using expression (4.11)

$$p_s(r,t) = -\frac{4p_l}{\pi k^2}\int_0^R M\left(\frac{r}{s}\right)\frac{ds}{\sqrt{R^2-s^2}}. \quad (4.48)$$

An elliptic cavity results in a uniform pressure distribution along the walls, hence our assumption of uniform p_s holds (Sneddon & Lowengrub, 1969). We can find

the value of the elastic pressure p_s in terms of p_l and k by evaluating the integral expression at $r = 0$:

$$p_s(0) = -\frac{4p_l}{\pi k^2}\int_0^R \frac{ds}{\sqrt{R^2 - s^2}} = -\frac{2p_l}{k^2}. \tag{4.49}$$

Then, from the pressure balance $p_s - p_l = p_T$ we have p_l and p_s given in terms of p_T (i.e. in terms of the undercooling ΔT) and k as

$$p_l = -\frac{k^2}{2 + k^2}p_T \quad \text{and} \quad p_s = \frac{2}{2 + k^2}p_T. \tag{4.50}$$

The cavity shape $B(\eta) = b(r, t)/kc^{1/2}t^{1/2}$ varies with k according to

$$B(\eta) = \frac{4}{\pi}\frac{P_T}{2 + k^2}\sqrt{1 - \eta^2}, \tag{4.51}$$

where $P_T = p_T/m$ is the non-dimensional value of the disjoining pressure.

We see that the propagation rate k cannot be determined by the system of equations (4.35)-(4.37) alone, and an additional condition is required. In section 4.1.2, we showed that LEFM predicts a parabolic-shaped tip, which governs the propagation of a crack. This condition defines a curvature for the tip which does not vary with time. In contrast, the elliptic cavity has a time-dependent tip curvature, as can be seen in equation (4.55). This means that the tip propagation condition predicted by LEFM unfortunately cannot be incorporated in the elliptic-shaped similarity solution here, so the propagation rate k remains a parameter in this approach. Figure 4.4 shows the aspect ratio of the cavity for different propagation rates k. The value of $B(\eta)$ at $\eta = 0$, which gives the aspect ratio of the crack, is shown as a function of k in equation (4.53). We have taken the undercooling $\Delta T = 2\,\mathrm{K}$, the shear modulus $G = 13\,\mathrm{GPa}$ and Poisson's ratio $\nu = 0.2$, representative of a limestone (values for parameters of other rocks and clays are given in table 7.2 of chapter 7) to find that $P_T \approx 10^{-4}$.

The first thing we note is that the maximum aspect ratio (defined as thickness over length) is given by $2P_T/\pi \approx 10^{-4}$, resulting in thin cavities. The thickness of the cavity depends on parameters such as the undercooling ΔT and the elasticity

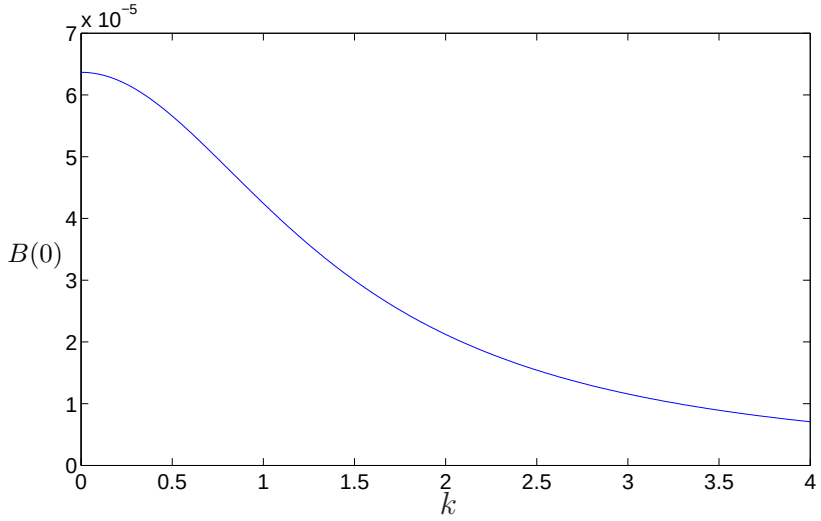

Figure 4.4: *The self-similar cavity aspect ratio against the propagation rate k. The dimensionless disjoining pressure has been taken to be $P_T = 10^{-4}$ which represents an undercooling of $\Delta T = 2\,\mathrm{K}$ for a limestone-like rock.*

of the medium G through the dimensionless parameter

$$P_T = \frac{1-\nu}{G}\frac{\rho_s \mathcal{L} \Delta T}{T_m}. \tag{4.52}$$

From the above expression we see that thicker cavities occur for larger undercoolings, as the disjoining pressure is larger and hence can deform the cavity more. Also, a smaller value of G results in a larger aspect ratio as the medium is more compliant and hence deforms more under a given amount of stress. For small propagation rates k, the self-similar shape tends to its maximum value

$$B(\eta) = \frac{2P_T}{\pi}\sqrt{1-\eta^2}. \tag{4.53}$$

This is the limit of no propagation ($k \to 0$), hence the material is tough enough to withstand the pressure applied for the given undercooling ΔT. The solid pressure in this case equals the disjoining pressure, as the liquid pressure tends to zero. This describes a situation of equilibrium, where the elastic back pressure of the medium is balancing the disjoining forces between rock and ice, and no more solidifying is occurring, hence there is no flow of water towards the cavity, agreeing with $p_l = 0$ at $k = 0$, given from equation (4.50).

A slow propagation rate k generally implies a tough cavity, which requires

a high pressure to fracture. This implies that the deformation of the cavity, and hence the aspect ratio, is relatively large. The liquid pressure is negative as described by equation (4.50) but with a small absolute value. This is expected, as the process is slow enough for the water flow through the porous medium to be sufficiently fast so that water is able to fill the opening gap between the ice and the rock easily. In contrast, fast propagation requires larger negative pressures, and cavitation effects can become important. Fast fracturing occurs in weak rocks and, since not much pressure is required to fracture them, their aspect ratios decay like $1/k^2$ with the propagation rate k. Here, the controlling process is the ability of water to flow to the freezing front at the rate required to sustain the propagation. In general, the parameter k is related to how tough the medium is, with large values of k corresponding to weak materials. As the radius of the cavity is

$$R(t) = k\left(\frac{\Pi}{\mu}\frac{G}{1-\nu}\right)t^{1/2}, \tag{4.54}$$

we see that the extent of the crack also depends on other material parameters, such as the permeability Π and the shear modulus G. For example, in a very impermeable medium, the flow towards the solidification front is heavily constrained and hence the growth of the cavity is slow. This results in small crack extents for a given time t. Similarly, if a medium is very compliant (i.e. G is small), the cavity deforms more under pressure, requiring a lot of water to freeze for the pressure to be sustained. This results in slower propagation.

Secondly, it is interesting to note that this problem produces small aspect ratios for the propagating cavities. Even for slow propagation, a crack of radius 1cm is only about 1μm thick, hence the aspect ratio is of the order of 10^{-4}. We have ignored effects of curvature-melting on the near-flat ice surface, but these effects can become important at the highly curved ice tips. For elliptic-shaped ice, the curvature at the tip is given by

$$\kappa = \frac{R(t)}{b(0,t)^2} = \frac{\pi^2}{16c^{1/2}P_T^2}\frac{(2+k^2)^2}{k}t^{-1/2} \sim 6\cdot 10^7\frac{(2+k^2)^2}{k}|t|^{-1/2}\mathrm{cm}^{-1}, \tag{4.55}$$

where $|t|$ is the elapsed time in sec. We have used parameters appropriate for a limestone. For an undercooling of ΔT, the Gibbs-Thompson relation given by

equation (2.11) defines the maximum curvature that the tip of the ice can have

$$\kappa_{\max} = \frac{\rho_s \mathcal{L} \Delta T}{\gamma T_m} \approx 3 \times 10^5 \mathrm{cm}^{-1}\mathrm{K}^{-1} \times \Delta T. \tag{4.56}$$

Figure 4.5 shows a plot of the curvature κ against the propagation rate k for different values of time t. The maximum curvature is shown by the red curve and we see that even at large times, the curvature of the ice tip is above the Gibbs-Thompson defined threshold $\kappa_{\max}$. In these cases, ice can grow inside the cavity, but is unable to extend all the way to the tip of the crack. This means that the cavity is not completely ice-filled and some of our assumptions fail, including that of a uniform gap h between the ice and the rock and the pressure balance across it. In addition to this, water flow in the r direction inside the cavity might become important, since the water fills the whole width of the cavity and the thickness of the film is not small anymore.

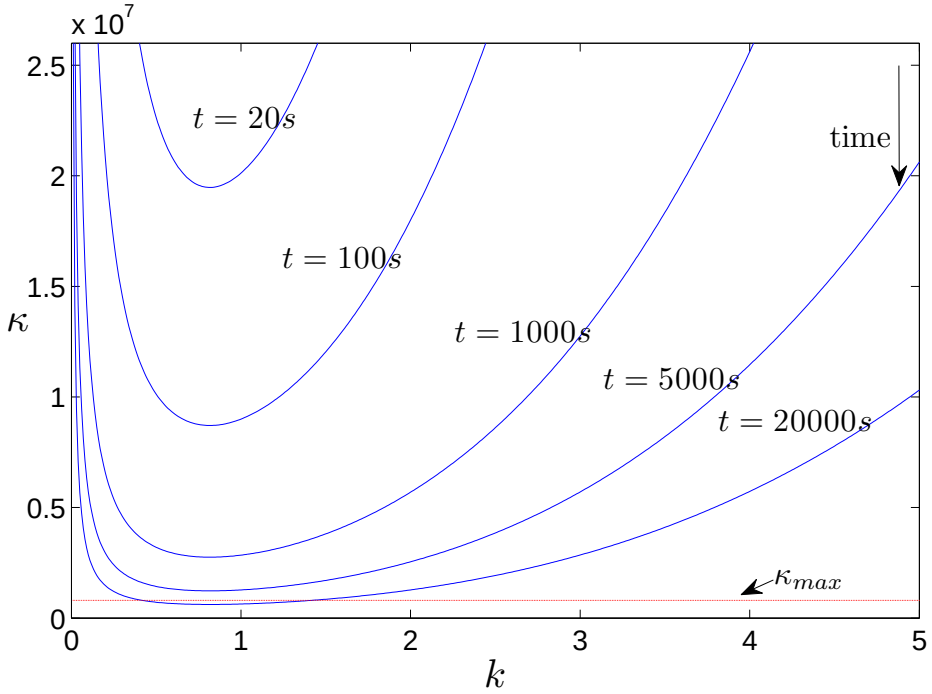

Figure 4.5: *The curvature of the ice tip against the propagation rate k at several times. The red line indicates the maximum curvature κ_{max} given by equation* (4.56)*, determined by the Gibbs-Thompson relation* (2.11)*.*

Despite these limitations, we have studied the balance of the liquid and solid pressure fields and discovered that they admit elliptic solutions for the cavity

shape for uniform pressure distributions. The family of solutions has provided information about the aspect ratio of the cavities and indicated that curvature-melting phenomena can play an important role in determining the extent of the ice inside the cavity. We have also derived useful results about the relation between cavity thickness and propagation rate and discussed the processes that dominate slow and fast propagation. We now aim to improve our model to close the problem by determining the propagation variable k and including the criterion for the propagation of the cavity. Analytic solutions are unlikely to be found for non-uniform pressure distributions. In addition to this, there will likely be further complications when determining the propagation rate from the tip condition (4.15). We therefore aim to develop a numerical method to solve the system of integral equations (4.11) and (4.27) together with the pressure balance (4.28). The analytic solution obtained in this section can be used as a test for the numerical results and the method can then be adjusted to solve for more complicated situations.

4.3 Numerical approach

Concentrating on the pressure balance equation and the scales that it dictates has given us a family of self-similar elliptic solutions. We have ignored the tip condition which needs to be taken into account in order for the propagation rate k to be determined. Instead of solving for the liquid pressure field directly, under the assumption of uniform distribution, we develop a numerical method for the integral equations, which we will first apply to the similarity solution (4.35) - (4.37) and compare the results against the analytic solution just found. We note that at $\sigma = \eta$ the kernel of (4.35) has a pole singularity, while the kernel of (4.36) has a log singularity. Any numerical schemes that we employ will have to be able to deal with these singularities.

4.3.1 Method 1: Linear spline

The idea here is to extract the tip behaviour described by equation (4.15) and then represent the remaining part of $B(\eta)$ by using a linear spline. Even though

the tip equation isn't used in this test problem, we want our method to be easily generalized to include the tip behaviour later. To do this, we divide $[0,1]$ into N intervals of equal length. We take the cavity width in each interval to be of the form

$$B_n(\eta) = \left(1-\eta^2\right)^{1/2} f_n(\eta), \tag{4.57}$$

where $f_n(\eta)$ is a piecewise linear function $f_n(\eta) = \alpha_n\eta + \beta_n$. Then,

$$B_n'(\eta) = \left(1-\eta^2\right)^{-1/2} (\alpha_n - 2\alpha_n\eta^2 - \beta_n\eta). \tag{4.58}$$

We can write expressions for the two pressures as sums of integrals that we are able to compute numerically. For the liquid pressure we have

$$P_l(\eta) = -k^2 \sum_{n=1}^{N} \left(\alpha_n Q_n + \beta_n R_n\right), \tag{4.59}$$

where

$$Q_n(\eta) = \frac{1}{\pi} \int_{\eta_n}^{\eta_{n+1}} K\left(\frac{2\sqrt{\eta\sigma}}{\eta+\sigma}\right) \frac{\sigma^4}{\eta+\sigma} \frac{d\sigma}{\sqrt{1-\sigma^2}} \tag{4.60}$$

and

$$R_n(\eta) = \frac{1}{\pi} \int_{\eta_n}^{\eta_{n+1}} K\left(\frac{2\sqrt{\eta\sigma}}{\eta+\sigma}\right) \frac{\sigma}{\eta+\sigma} \frac{d\sigma}{\sqrt{1-\sigma^2}}. \tag{4.61}$$

Similarly,

$$P_s(\eta) = \sum_{n=1}^{N} \left(\alpha_n S_n + \beta_n T_n\right), \tag{4.62}$$

with

$$S_n(\eta) = \fint_{\eta_n}^{\eta_{n+1}} M\left(\frac{\eta}{\sigma}\right) \frac{2\sigma^2-1}{\sqrt{1-\sigma^2}} \frac{d\sigma}{\sigma} \tag{4.63}$$

and

$$T_n(\eta) = \fint_{\eta_n}^{\eta_{n+1}} M\left(\frac{\eta}{\sigma}\right) \frac{d\sigma}{\sqrt{1-\sigma^2}}. \tag{4.64}$$

The complete elliptic integral of the first kind $K(x)$, appearing in both integrals Q_n and R_n as well as the kernel $M(\eta/\sigma)$ of the integrals S_n and T_n, has a logarithmic singularity at $x = 1$. The Matlab built-in function *quadgk* can deal with such integrable singularities. In addition to this, there is a pole singularity from the kernel $M(\eta/\sigma)$ at $\sigma = \eta$. We deal with this as explained in appendix C. We need to find the coefficients of the linear spline, α_n and β_n, hence we have $2N$

unknowns in total. We require the spline to be continuous across $\eta = \eta_n$, which gives $N - 1$ continuity equations

$$(\alpha_n - \alpha_{n-1})\,\eta_{n-1} + (\beta_n - \beta_{n-1}) = 0 \;\text{ for }\; 0 < n < N. \tag{4.65}$$

Also, we evaluate $P_s(\eta) - P_l(\eta) = P_T$ at the midpoints of each interval, i.e. at $\sigma_j = (2j-1)/2N$ to obtain a further N equations

$$(S_{jn} + k^2 Q_{jn})\alpha_n + (T_{jn} + k^2 R_{jn})\beta_n = P_T, \tag{4.66}$$

where $S_{jn} = S_n(\sigma_j)$ etc. The last condition to complete the linear system comes from the assumption that the slope at $\eta = 0$ is zero, since we assume the crack is symmetric with respect to $\eta = 0$ and smooth. Therefore

$$\alpha_1 = 0. \tag{4.67}$$

The set of equations can be written in matrix form

$$\mathbf{G}(\alpha_1, \ldots, \alpha_N, \beta_1, \ldots, \beta_N) = (P_T, \ldots, P_T, 0, \ldots, 0), \tag{4.68}$$

where

$$\mathbf{G} = \begin{pmatrix}
A_{11} & \cdots & \cdots & A_{1N} & C_{11} & \cdots & \cdots & C_{1N} \\
A_{21} & \cdots & \cdots & A_{2N} & C_{21} & \cdots & \cdots & C_{2N} \\
\vdots & \ddots & & & & \ddots & & \vdots \\
\vdots & & \ddots & & & & \ddots & \vdots \\
A_{N1} & \cdots & \cdots & A_{NN} & C_{N1} & \cdots & \cdots & C_{NN} \\
1 & 0 & \cdots & \cdots & \cdots & \cdots & \cdots & 0 \\
-\eta_1 & \eta_1 & \cdots & 0 & -1 & 1 & \cdots & 0 \\
0 & -\eta_2 & \cdots & 0 & 0 & -1 & \cdots & 0 \\
\vdots & \ddots & & & & \ddots & & \vdots \\
0 & \cdots & -\eta_{N-1} & \eta_{N-1} & 0 & \cdots & -1 & 1
\end{pmatrix},$$

with $A_{jn} = S_{jn} + k^2 Q_{jn}$ and $C_{jn} = T_{jn} + k^2 R_{jn}$.

4.3.2 Method 2: Point values

We are also interested in developing a simpler method and comparing the results with both the analytic solution as well as the linear spline numerical results. For the linear spline, we decided to use high order methods to numerically evaluate the integrals, which meant we had to deal with the singularities of the kernels before implementing the schemes. Here, we want to investigate how much accuracy we lose if we use a simpler method both for representing the function $B(\eta)$ as well as calculating the integrals.

The simplest methods of approximating an integral are the mid-point rule

$$\int_{\eta_n}^{\eta_{n+1}} f(\eta,\sigma)\,d\sigma = \frac{1}{N} f\left(\eta,\sigma_n\right) \tag{4.69}$$

and the trapezium rule

$$\int_{\eta_n}^{\eta_{n+1}} f(\eta,\sigma)\,d\sigma = \frac{1}{2N}\left[f\left(\eta,\eta_n\right) + f\left(\eta,\eta_{n+1}\right)\right]. \tag{4.70}$$

We need to take into account the fact that our function $f(\eta,\sigma)$ has singularities at $\eta = \sigma$. Therefore, if we want to use the mid-point rule, the η at which the integral is evaluated can't be the midpoint of an interval, like in the linear spline algorithm. Instead, we can calculate the solid and liquid pressures $P_s(\eta)$ and $P_l(\eta)$ and apply the pressure balance equation (4.37) at the endpoints of the intervals $\eta = \eta_n$, for $1 < n < N$. We note that this approach still gives us N conditions as we haven't evaluated (4.37) at $B_{N+1} = 1$, i.e. the tip of the crack.

We use a linear spline to discretize the cavity thickness $B(\eta)$: we again split the [0,1] interval into N equal-sized intervals and then represent the function $B(\eta)$ by the values B_i at each interval endpoint $\eta_i = \dfrac{i-1}{N}$. The midpoints of each interval are $\sigma_i = \dfrac{2i-1}{2N}$. Inside each interval n we have

$$B(x) = B_n + \left(B_{n+1} - B_n\right)(x - x_n)N \quad \text{for} \quad x_n \le x \le x_{n+1}, \tag{4.71}$$

with the value of B at the interval midpoint given by

$$B = \frac{B_n + B_{n+1}}{2}. \tag{4.72}$$

The derivative of the cavity thickness is the slope of the spline in each interval

$$B'(x) = \frac{B_{n+1} - B_n}{\eta_{n+1} - \eta_n} = N(B_{n+1} - B_n) \text{ for } x_n \leq x \leq x_{n+1}. \tag{4.73}$$

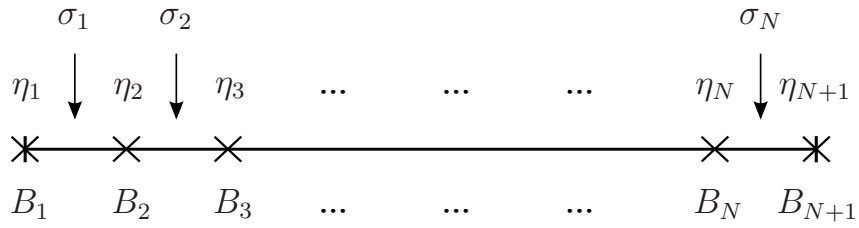

Combining all the above, we can write an expression for the pressures P_s and P_l evaluated at an interval edge-point η_j

$$\begin{aligned} P_s(\eta_j) &= -\sum_{n=1}^{N} \int_{\eta_n}^{\eta_{n+1}} M\left(\frac{\eta_j}{\sigma}\right) B'(\sigma) \frac{d\sigma}{\sigma} && (4.74) \\ &\equiv -\sum_{n=1}^{N} \alpha_{jn}(B_{n+1} - B_n) && (4.75) \\ &= \sum_{n=1}^{N} \left(\alpha_{jn} - \alpha_{j(n-1)}\right) B_n && (4.76) \end{aligned}$$

and

$$\begin{aligned} P_l(\eta_j) &= -\frac{k^2}{\pi} \sum_{n=1}^{N} \int_{\eta_n}^{\eta_{n+1}} K\left(\frac{2\sqrt{\sigma\eta_j}}{\sigma + \eta_j}\right) [B(\sigma) - \sigma B'(\sigma)] \frac{\sigma\, d\sigma}{\sigma + \eta_j} && (4.77) \\ &\equiv -\frac{k^2}{\pi} \sum_{n=1}^{N} \beta_{jn} \left[\left(\frac{1}{2N} + \sigma_n\right) B_n + \left(\frac{1}{2N} - \sigma_n\right) B_{n+1}\right] && (4.78) \\ &= -\frac{k^2}{\pi} \sum_{n=1}^{N} \left[\left(\frac{1}{2N} + \sigma_n\right) \beta_{jn} + \left(\frac{1}{2N} - \sigma_{n-1}\right) \beta_{j(n-1)}\right] B_n, && (4.79) \end{aligned}$$

where

$$\alpha_{jn} = \frac{1}{\sigma_n} M\left(\frac{\eta_j}{\sigma_n}\right) \text{ and } \beta_{jn} = \frac{\sigma_n}{\eta_j + \sigma_n} K\left(\frac{2\sqrt{\eta_j \sigma_n}}{\eta_j + \sigma_n}\right) \tag{4.80}$$

for $1 \leq j \leq N$ and $1 \leq n \leq N$. We have also used the fact that $B_{N+1} = 0$ and we are taking $\alpha_{j0} = \beta_{j0} = 0$. Using these expressions, the equations reduce to the

matrix problem

$$\left(A_{jn} + k^2 C_{jn}\right) B_n = P_T \quad \text{for} \quad 1 \leq j \leq N, \tag{4.81}$$

with $A_{jn} = \alpha_{jn} - \alpha_{j(n-1)}$ and $C_{jn} = \frac{1}{\pi}\left[\left(\frac{1}{2N} + \sigma_n\right)\beta_{jn} + \left(\frac{1}{2N} - \sigma_{n-1}\right)\beta_{j(n-1)}\right]$.

4.3.3 Results

We plot the results from our two numerical schemes against the analytic solution found in §4.2.1 (red curve) for different values of the parameter k and the interval number N in figures 4.6-4.8. The left-hand-side graphs show the results of the point value (PV) algorithm for $N = 10, 20$ and 40. On the right, we have the linear spline results (LS) for the same values of N. These are plotted for three different values of the propagation rate $k = 0.1, 1$ and 10. On every graph, the red curve is the analytic solution derived in section 4.2.1. The three sets of graphs

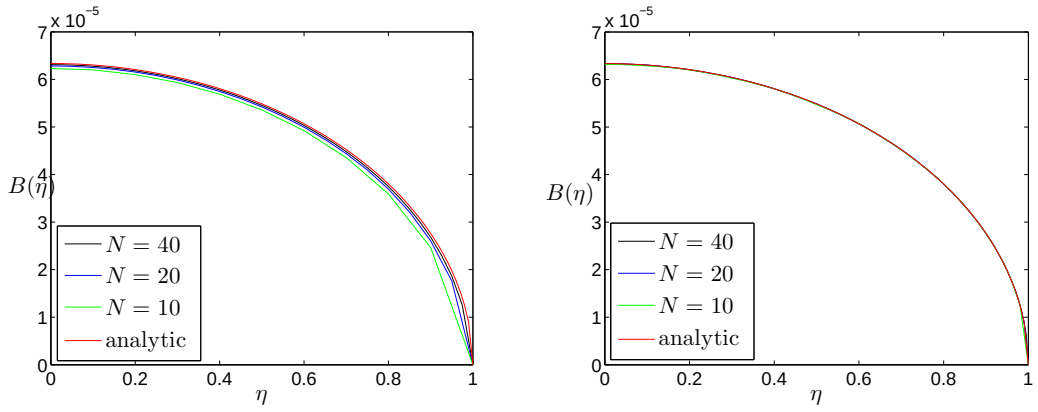

Figure 4.6: *Left: Numerical results from PV method for $N = 10$ (green), $N = 20$ (blue) and $N = 40$ (black) against analytic solution (red). Right: Results from LS method for the same values of N. In both cases, $k = 0.1$.*

clearly show a much better agreement between the LS results and the analytic solution. Even though the PV method doesn't produce curves as close to the analytic ones, the results are still acceptable, even for grids with relatively low resolution ($N = 10$ or 20). The LS method seems to be doing a lot better towards $\eta = 1$ in particular, which is to be expected since the $\sqrt{1-\eta^2}$ behaviour is already included in the expression for $B(\eta)$ (4.57).

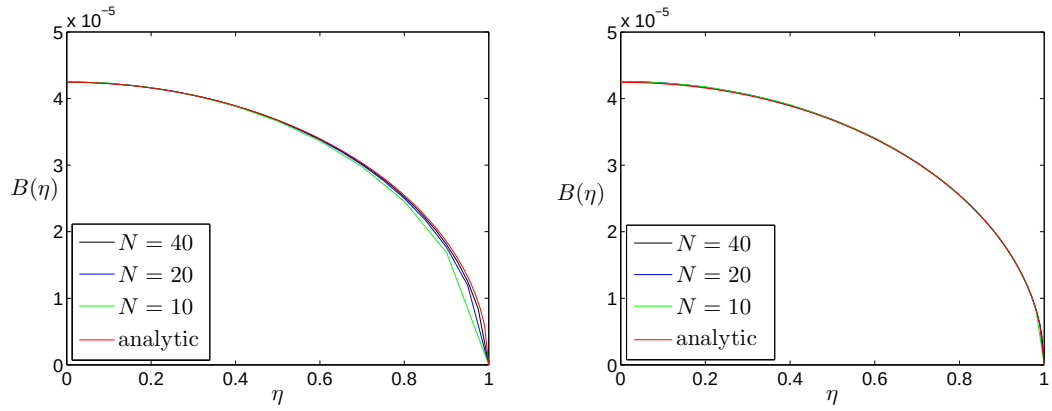

Figure 4.7: *Left: Numerical results from PV method for $N = 10$ (green), $N = 20$ (blue) and $N = 40$ (black) against analytic solution (red). Right: Results from LS method for the same values of N. In both cases, $k = 1$.*

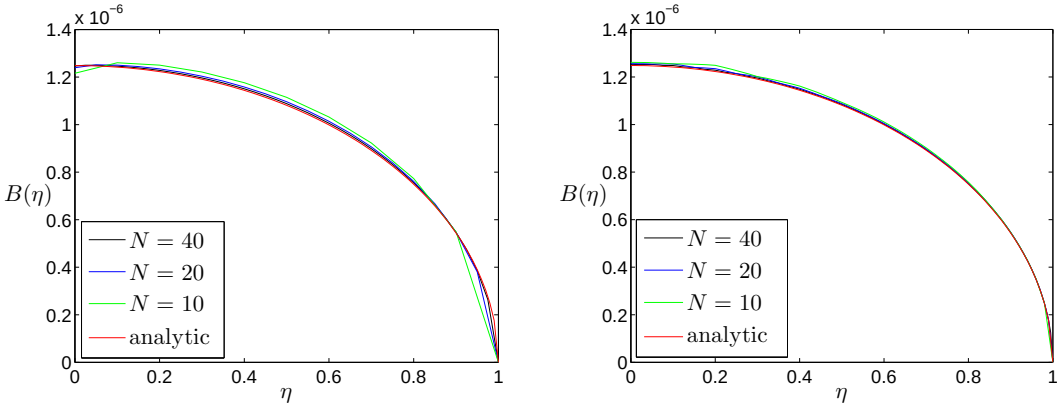

Figure 4.8: *Left: Numerical results from PV method for $N = 10$ (green), $N = 20$ (blue) and $N = 40$ (black) against analytic solution (red). Right: Results from LS method for the same values of N. In both cases, $k = 10$.*

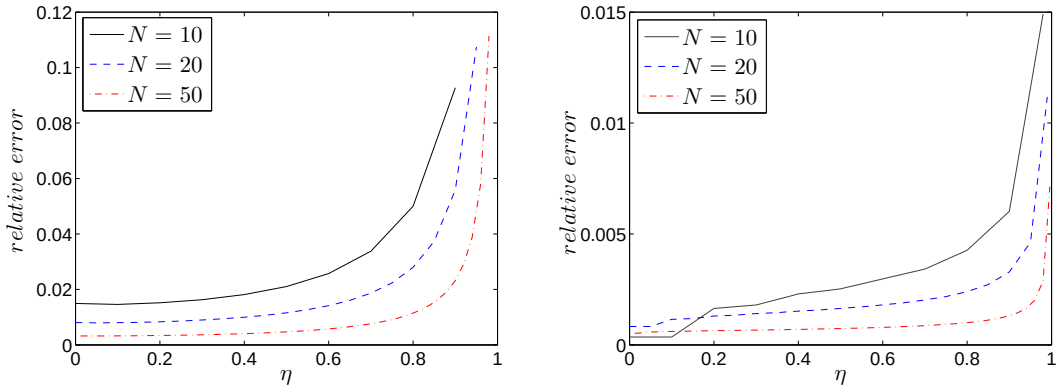

Figure 4.9: *Plots of the relative error for different resolutions N for the PV method (left) and the LS method (right) for $k = 0.1$.*

We can look at these observations in more detail by plotting the relative error, i.e. error = (analytic − numerics)/analytic. There is a distinct trend throughout the error graphs. The errors are largest towards the $\eta \approx 1$ region, for both methods, while errors from the PV method are about an order of magnitude larger than the errors from the LS method close to the tip. As k increases, we see the errors for PV decreasing. This is because the biggest contribution comes

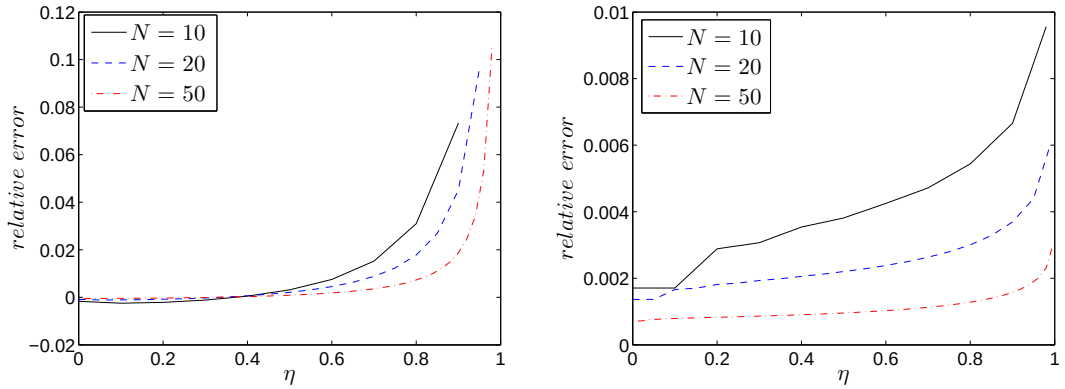

Figure 4.10: *Plots of the relative error for different resolutions N for the PV method (left) and the LS method (right) for $k = 1$.*

from the pole singularity in A_{jn}, which dominates the matrix $A_{jn} + k^2 C_{jn}$ when k is small. The LS errors are of similar size for all values of k. The main reason for the better accuracy of the LS method is the fact that the interval integrals are calculated using the *quadgk* routine, while in the PV case we have used the simpler mid-point rule. This also results in the PV method being considerably

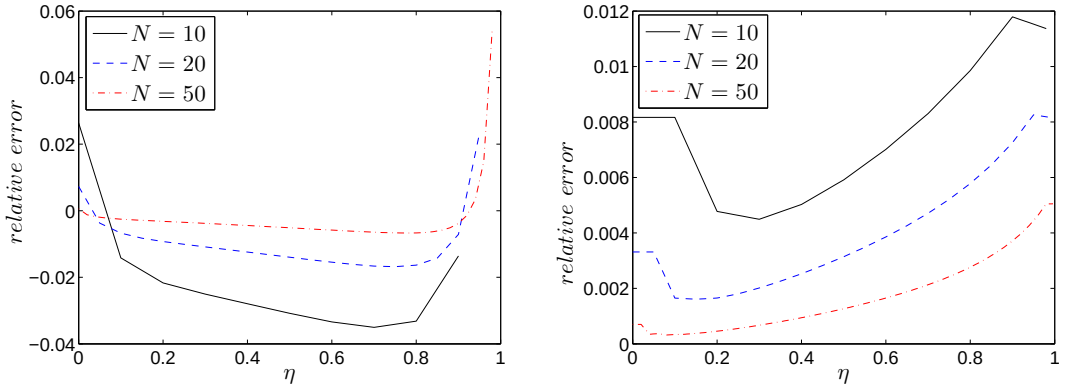

Figure 4.11: *Plots of the relative error for different resolutions N for the PV method (left) and the LS method (right) for $k = 10$.*

faster than the LS method. The difference in speed, coupled with the considerably simpler implementation which will become increasingly important as we tackle more complicated problems in chapters 5 and 6, are the two attractive features of the PV method.

Averaging the error over the N intervals and plotting against N in a log-log plot (figure 4.12) can provide information about the order of our numerical scheme. On the left hand side of figure 4.12 is the average error for the PV

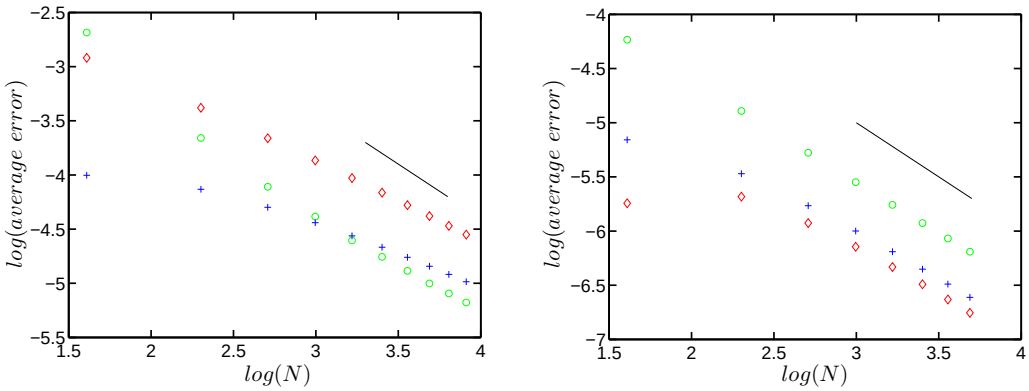

Figure 4.12: *Log-log plots of the average error produced by the PV method (left) and the LS method (right) against the number of intervals N. Green circles represent $k = 10$, blue crosses $k = 1$ and red diamonds $k = 0.1$. The solid line has a slope of -1.*

numerical scheme. As expected, the average error decreases as the interval number N increases. It is also interesting that the error of the two methods behaves differently with k: as we saw, with the PV method, the average error decreases with k. In the LS case, we observe the opposite behaviour, with the larger error coming from the $k = 10$ case, indicating that the log singularity of C_{jn} is the main contribution to the error. This shows that the main difference of the two methods is the treatment of the pole singularities. The black solid lines have slope -1, indicating that both methods are approximately first order.

4.4 Conclusion

In this chapter we have used some ideas of the spherical model developed in chapter 3 and expanded on them to create a mathematical model for a 3D penny-shaped crack. We have solved for the liquid pressure satisfying Laplace's equation

in the porous medium and for the solid pressure governed by linear elasticity. The two integral equations obtained have been combined through a pressure balance across the premelted film. We solved the problem of uniform distribution of pressures along the cavity analytically, and obtained solutions describing the propagation of the cavity when the only process limiting the fracturing is the supply of water. The propagation rate k was not determined by the pressure balance alone, and hence a family of solutions for different values of k was found. The theory of linear elasticity predicts the behaviour of the tip of a thin crack but we saw that the relation cannot be incorporated in the similarity solution framework described in this chapter.

Despite this, the study of the analytic family of solutions has provided us with interesting conclusions about the effect that different parameters of the problem such as the elastic modulus and the permeability of the medium, as well as the undercooling of the system, have on the characteristics of the cavity. In particular, small aspect ratios were observed for typical parameters of rocks. In addition to this, the analytic solution has enabled us to compare different numerical approaches for the solution of the problem, which will become useful in the next chapters. The understanding we have obtained from this chapter will be used in determining the important features our model should include.

Chapter 5

A similarity solution in a warming environment

In chapter 4, we discussed the growth of ice in a penny-shaped cavity and looked at the shape of those cracks and their evolution with time. We took the surrounding environment to be undercooled to some fixed temperature $T_\infty < T_m$, where T_m is the melting temperature measured at some pressure $p_m = p_\infty$. We found that the propagation rate cannot be determined by the balance of the solid and liquid pressures alone. In this chapter, we will incorporate the condition on the tip propagation as described by equation (4.15). We also allow for temperature variations inside the cavity and the rock, which describes the system in a more realistic way. Irrespective of the temperature field, a constant undercooling of the far field $\Delta T = T_m - T_\infty$ implies a non-decaying temperature field, i.e. a non-decaying disjoining pressure p_T, as can be seen from equation (4.27). Through the

pressure balance (4.28) we deduce that this implies non-decaying liquid and solid pressure fields which, as in the previous chapter, lead to a balance between the width and the length scales $W \sim L$. This length scale balance cannot incorporate the parabolic shape imposed by the tip condition (4.15), which is likely to make the similarity solution break down.

The problem of a non-decaying disjoining pressure can be addressed by considering a warming environment, with the undercooling determined by a power law of the form $\Delta T = Ht^{-\alpha}$, where $\alpha > 0$. This describes a supercooled system which is warming up to T_m asymptotically. It overcomes the problem of constant undercooling and we shall see that it provides us with the opportunity to develop a similarity solution including the dynamics of the tip for a specific power law α. This, used together with time-dependent results derived later, can provide an interesting insight into the long-term behaviour of the fracture. In nature, the far-field temperatures will vary with time, so the study here can provide interesting insight on how this variation affects the fracturing.

5.1 The governing equations

Our extended problem is based on the model described in chapter 4, with a few modifications to allow for temperature variations in the far field as well as the non-uniform temperature field inside the rock and cavity. We will also consider the Gibbs–Thompson effect of curvature-induced melting of ice, since we discovered at the end of chapter 4 that it could potentially play an important role. Therefore, we assume that the ice in the cavity only extends up to $r = \lambda R$, where $\lambda \in [0, 1]$, with the rest of the cavity filled with water. A sketch of the cavity is shown in Figure 5.1. The pressure field in the surrounding elastic medium can be expressed in terms of the cavity shape, as in chapter 4,

$$p_s(r,t) = -\frac{2}{\pi}\, m \fint_0^{R(t)} M^*\left(\frac{r}{s}\right) \frac{\partial b}{\partial s}\, \frac{ds}{s}, \tag{5.1}$$

where $m = G/(1-\nu)$.

The water pressure satisfies Laplace's equation in the porous medium. There is a water flux $q(r,t)$ towards the cavity and, since the crack is long and thin,

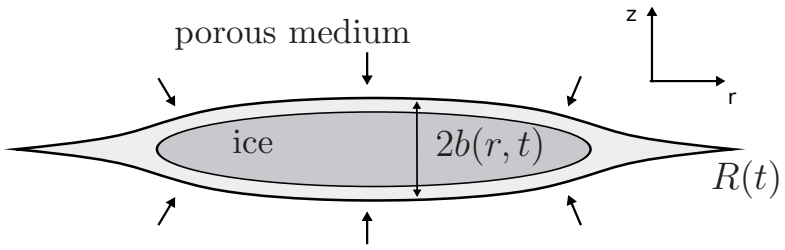

Figure 5.1: *A sketch of a penny-shaped crack propagating in a porous rock, where the tip is at $r = R(t)$ and the ice extends to $r = \lambda R(t)$. The thickness of the cavity is $2b(r,t)$.*

it can be approximated as a planar sink. We can therefore express the liquid pressure field in terms of $q(r,t)$ using the Green's function

$$p_l(r,t) = \frac{1}{\pi}\frac{\mu}{\Pi}\int_0^{R(t)} K\left(\frac{2\sqrt{rs}}{r+s}\right) q(s,t)\frac{s\,ds}{s+r}, \tag{5.2}$$

where K is the complete integral of the first kind which arises from integrating out the θ dependence. The idea we used in section 4.1.3 is to relate the water flux to the cavity deformation and therefore, substituting into equation (5.2), obtain an integral expression of the liquid pressure $p_l(r,t)$ in terms of $b(r,t)$. In the thin film between the ice and the rock (i.e. for $r < \lambda R$), we can still use the thin film approximation as in section 4.1.3 to find

$$q(r,t) = -\frac{2\Pi}{\mu}\lim_{z\to 0}\frac{\partial p}{\partial z} = -2\frac{\partial b}{\partial t}. \tag{5.3}$$

When $\lambda < 1$, the region towards the tip of the crack isn't occupied by ice but is instead filled with water. If this gap is large enough to allow easy flow in the r direction, we can approximate the liquid pressure as uniform. Close to the tip, it is likely that the width of the crack will be small, as the ice would be able to extend further towards the tip otherwise. For example, for $\Delta T = 1\,\mathrm{K}$ the critical radius of curvature of ice is of the order of $0.1\,\mu\mathrm{m}$, hence we expect the thickness of the water-filled tip to be at most that. The balance (4.25) tells us that the flow inside the film and through the medium are in this case at most comparable. As the temperature increases, the critical radius of curvature decreases, which means that the ice can extend further inside the cavity, and the thickness of the water-

filled tip is even smaller. This indicates that the thin film approximation is valid in the tip too. The alternative would be to use a uniform pressure distribution for the water-filled tip, which would describe a situation in which the flow inside the gap is quick enough to relax any pressure difference along the gap. Appendix D gives the details of the uniform pressure approximation and compares results of the two different schemes. We see that the difference in the results is minimal, but the thin film approximation method is much easier to implement, as it only uses the cavity width values as unknowns, and the linear matrix is of size $N \times N$ rather than $2N \times 2N$. For the remainder of the thesis we will therefore use expression (5.3) to describe the flux of water inside the cavity. This means that the liquid pressure can be written as

$$p_l(r,t) = -\frac{2}{\pi}\frac{\mu}{\Pi}\int_0^{R(t)} K\left(\frac{2\sqrt{rs}}{r+s}\right)\frac{\partial b}{\partial t}\frac{s\,ds}{s+r}. \tag{5.4}$$

We assume that the temperature field is quasi-steady as in section 3.1, and hence is described by Laplace's equation

$$\nabla^2 T = 0. \tag{5.5}$$

The Stefan condition expresses the release of latent heat from the solidification front, which is necessary for the freezing process to continue

$$\rho_s \mathcal{L}\frac{\partial b}{\partial t} = -k_l \lim_{z\to 0}\frac{\partial T}{\partial z}. \tag{5.6}$$

We define the undercooling $\theta(r,z,t) = T(r,z,t) - T_\infty(t) > 0$ which decays as $r \to \infty$ and satisfies the same equations as T^I, (5.5) and (5.6). By comparing equations (5.3) and (5.6), and noting that both p_l and θ^I satisfy Laplace's equation and decay as $r \to \infty$, we see that the interface undercooling $\theta^I(r,t) \approx \theta(r,0,t)$ can be expressed in a similar way to p_l as an integral of $\partial b/\partial t$

$$\theta^I(r,t) = \frac{2}{\pi}\frac{\rho_s \mathcal{L}}{k_l}\int_0^{\lambda R(t)} K\left(\frac{2\sqrt{rs}}{r+s}\right)\frac{\partial b}{\partial t}\frac{s\,ds}{s+r}. \tag{5.7}$$

In the special case $\lambda = 1$, we see that the temperature field is simply proportional to the liquid pressure field $\theta^I = -\frac{\rho_s \mathcal{L}}{k_l}\frac{\Pi}{\mu}p_l$.

The balance of pressures across the premelted film is described by $p_s - p_l = p_T$, where the solid pressure acting on the rock is balanced by the liquid pressure in the thin film and the disjoining forces between the ice and the rock acting across the film. For $r > \lambda R$, where there is no ice, the solid pressure simply balances the liquid pressure. Equation (4.30), taking into account the time-varying temperature field, becomes

$$p_s(r,t) - p_l(r,t) = \begin{cases} \dfrac{\rho_s \mathcal{L} H t^{-\alpha}}{T_m} - \dfrac{\rho_s \mathcal{L}}{T_m}\theta^I(r,t) & \text{if } r \leq \lambda R. \\ \\ 0 & \text{if } r > \lambda R. \end{cases}$$

The extent of the ice is limited by the curvature at its tip, with its maximum value given by the Gibbs–Thompson relation (2.11) evaluated at $r = \lambda R$. The ice tip is approximated as circular and hence the curvature at the tip is taken as $\kappa = 1/b(\lambda R, t)$. The relation determining the ice extent λ is

$$\kappa\gamma = \frac{2\gamma}{b(\lambda R(t), t)} = \frac{\rho_s \mathcal{L} H t^{-\alpha}}{T_m} - \frac{\rho_s \mathcal{L}}{T_m}\theta^I(\lambda R(t), t). \tag{5.8}$$

Finally, as described in section 4.1.2, the tip propagation is governed by

$$b(r,t) \sim \sqrt{\frac{8}{\pi}}\frac{K}{m}\sqrt{R-r} \quad \text{as} \quad r \to R, \tag{5.9}$$

where K is the critical stress-intensity factor (mode I), or fracture toughness, and $m = G/(1-\nu)$.

5.1.1 Non-dimensionalization

We scale pressures with P, length with L, width with W, time with t^* and temperature with θ^* and we find the following balances of scales

$$P \sim \frac{G}{1-\nu}\frac{W}{L} \tag{5.10}$$

$$P \sim \frac{\mu}{\Pi}\frac{LW}{t^*} \tag{5.11}$$

$$\theta^* \sim \frac{\rho_s \mathcal{L}}{k_l} \frac{LW}{t^*} \tag{5.12}$$

$$P \sim \frac{\rho_s \mathcal{L}}{T_m} \theta^* \sim \frac{\rho_s \mathcal{L} H}{T_m} t^{*-\alpha} \tag{5.13}$$

$$\frac{1}{W} \sim \frac{\rho_s \mathcal{L} H}{T_m} t^{*-\alpha} \sim \frac{\rho_s \mathcal{L}}{T_m} \theta^* \tag{5.14}$$

and

$$W \sim \frac{K}{m} L^{1/2}. \tag{5.15}$$

The first four relations give us the balance of scales $P \sim \theta^* \sim t^{*-\alpha}$, $L \sim t^{*1/2}$ and $W \sim t^{*-\alpha+1/2}$ valid for any α. Furthermore, the ice-extent balance (5.14) dictates that the thickness of the cavity should behave as $W \sim t^{*\alpha}$ and the tip condition (5.15) shows the relation between width and length $W \sim L^{1/2}$. The last two conditions can only be included in the similarity solution for the special case $\alpha = 1/4$.

5.2 Special case: $\alpha = \frac{1}{4}$

Working with this special undercooling law of course limits the relevance of our results to real-life scenarios, but there is a lot to be gained by this approach. First of all, being able to include both the ice-extent condition as well as the tip condition in our similarity solution makes for a very interesting problem worth exploring. The results will give us an idea of the behaviour of the cavity shape and growth rates for this specific case and, combined with the time-dependent solution derived for more general conditions in chapter 6, we hope to be able to derive some general conclusions.

When $\alpha = 1/4$, the equations from section 5.1.1 describe a self-similar cavity. The scales for pressure, width, length and temperature, P, W, L, θ^* respectively, are related to the time scale as follows

$$P = \frac{2}{\pi} \sqrt{\frac{8}{\pi}} \left(\frac{\Pi}{\mu} \right)^{-1/4} K m^{-1/4} t^{*-1/4}, \tag{5.16}$$

$$\theta^* = \frac{2}{\pi} \sqrt{\frac{8}{\pi}} \left(\frac{\Pi}{\mu} \right)^{3/4} \frac{\rho_s \mathcal{L}}{k_l} K m^{-1/4} t^{*-1/4}, \tag{5.17}$$

$$L = \left(\frac{\Pi}{\mu} m\right)^{1/2} t^{*1/2}, \tag{5.18}$$

and

$$W = \sqrt{\frac{8}{\pi}} \left(\frac{\Pi}{\mu}\right)^{1/4} K m^{3/4} t^{*1/4}. \tag{5.19}$$

According to these scalings, we take the cavity length to be $R(t) = kt^{1/2}$, for some k to be determined. Unlike chapter 4, the propagation rate k will be determined here using the tip propagation condition (5.9). Then, we can define a similarity variable $\eta = \dfrac{r}{kt^{1/2}}$ and introduce the cavity thickness variable $B(\eta) = \dfrac{b(r,t)}{kt^{1/4}}$, therefore mapping the cavity to $[0,1]$. We also define the similarity functions $P_s(\eta) = t^{1/4} p_s(r,t)$, $P_l(\eta) = t^{1/4} p_l(r,t)$ and $\Theta^I(\eta) = t^{1/4}\theta^I(r,t)$. Then, we have

$$\frac{\partial b}{\partial r} = t^{-1/4} B'(\eta) \quad \text{and} \quad \frac{\partial b}{\partial t} = \frac{k}{t^{3/4}} \left[\frac{1}{4} B(\eta) - \frac{1}{2}\eta B'(\eta)\right]. \tag{5.20}$$

The set of equations in terms of the similarity variable becomes

$$P_s(\eta) = -\int_0^1 M^*\left(\frac{\eta}{\sigma}\right) B'(\sigma) \frac{d\sigma}{\sigma}, \tag{5.21}$$

$$P_l(\eta) = -k^2 \int_0^1 K\left(\frac{2\sqrt{\eta\sigma}}{\eta+\sigma}\right) \left[\frac{1}{4} B(\sigma) - \frac{1}{2}\sigma B'(\sigma)\right] \frac{\sigma d\sigma}{\eta+\sigma} \tag{5.22}$$

$$\Theta^I(\eta) = k^2 \int_0^\lambda K\left(\frac{2\sqrt{\eta\sigma}}{\eta+\sigma}\right) \left[\frac{1}{4} B(\sigma) - \frac{1}{2}\sigma B'(\sigma)\right] \frac{\sigma d\sigma}{\eta+\sigma}, \tag{5.23}$$

$$P_s(\eta) = \begin{cases} P_l(\eta) - \tilde{\Pi}\left[\Theta^I(\eta) - C\right] & \text{if } \eta \le \lambda, \\ P_l(\eta) & \text{if } \eta > \lambda, \end{cases} \tag{5.24}$$

$$\frac{1}{kB(\lambda)} = \tilde{K}\tilde{\Pi}\left[C - \Theta^I(\lambda)\right], \tag{5.25}$$

$$B(\eta) \sim k^{-1/2}\sqrt{1-\eta} \quad \text{as} \quad \eta \to 1, \tag{5.26}$$

where

$$C = \frac{\tilde{H}}{\tilde{\Pi}^{3/4}\tilde{K}} \quad \text{and} \quad \left\{ \begin{array}{l} \tilde{\Pi} = \dfrac{\rho_s^2 \mathcal{L}^2 \Pi}{\mu k_l T_m} \\ \\ \tilde{K} = \dfrac{4}{\pi} \dfrac{K}{\sqrt{2\gamma m}} \\ \\ \tilde{H} = \dfrac{\sqrt{\pi}}{2} \left(\dfrac{\rho_s^2 \mathcal{L}^2 k_l}{\gamma^2 m T_m^3} \right)^{1/4} H \end{array} \right\}. \tag{5.27}$$

The last three parameters can be thought of as dimensionless permeability, fracture toughness and undercooling respectively.

5.2.1 Numerical method

Two different numerical schemes were discussed in chapter 4 and the results were compared in section 4.3.3. Here, we will use the PV (point values) method as it gives reasonably accurate solutions even for a small number of intervals and is simpler to implement and faster to run. In particular, it doesn't require special treatment of the pole singularities of the integrands of $p_s(r,t)$ and avoids long, analytic calculations of integrals. As in section 4.3.2, we approximate the cavity width B as a linear spline, such that the value of B at the nth interval midpoint is given by

$$B = \frac{B_n + B_{n+1}}{2} \tag{5.28}$$

and the spatial derivative is approximated by the slope of the spline in each interval

$$B' = \frac{B_{n+1} - B_n}{\eta_{n+1} - \eta_n} = N\left(B_{n+1} - B_n\right). \tag{5.29}$$

The ice extends to $\eta = \lambda$ which is inside the Λth interval, say. This way, Λ is defined by $\eta_{\Lambda+1} = \dfrac{\Lambda}{N} = \dfrac{\lceil \lambda N \rceil}{N}$. The notation $\lceil x \rceil$ is the ceiling function and represents the smallest integer that isn't smaller than x. With that definition, we have $\eta_\Lambda < \lambda \leq \eta_{\Lambda+1}$. We use the mid-point rule to calculate the integrals involved in the expressions for the solid and liquid pressure and temperature fields. We

evaluate these expressions at the interval endpoints $\eta = \eta_j$, $1 \leq j \leq N$, to find

$$P_s(\eta_j) = \mu_{j1} B_1 + \sum_{n=2}^{N} \left[\mu_{jn} - \mu_{j(n-1)}\right] B_n, \tag{5.30}$$

$$P_l(\eta_j) = -k^2 \lambda_{j1} B_1 - k^2 \sum_{n=2}^{N} \left[\lambda_{jn} + \nu_{j(n-1)}\right] B_n \tag{5.31}$$

and

$$\begin{aligned} \Theta^I(\eta_j) &= k^2 \lambda_{j1} B_1 + k^2 \sum_{n=2}^{\Lambda-1} \left[\lambda_{jn} + \nu_{j(n-1)}\right] B_n + k^2 \nu_{j(\Lambda-1)} B_\Lambda + \\ &\quad + k^2 I_j^\lambda B_\Lambda + k^2 J_j^\lambda B_{\Lambda+1}, \end{aligned} \tag{5.32}$$

with

$$\mu_{jn} = \frac{1}{\sigma_n} M^* \left(\frac{\eta_j}{\sigma_n}\right), \tag{5.33}$$

$$\lambda_{jn} = K\left(\frac{2\sqrt{\eta_j \sigma_n}}{\eta_j + \sigma_n}\right) \frac{\sigma_n}{\sigma_n + \eta_j} \left(\frac{1}{8N} + \frac{\sigma_n}{2}\right), \tag{5.34}$$

$$\nu_{jn} = K\left(\frac{2\sqrt{\eta_j \sigma_n}}{\eta_j + \sigma_n}\right) \frac{\sigma_n}{\sigma_n + \eta_j} \left(\frac{1}{8N} - \frac{\sigma_n}{2}\right). \tag{5.35}$$

The last two terms from the expression for $\Theta^I(\eta_j)$ (5.32) come from the integral over (η_Λ, λ), which is the ice-occupied part of the Λth interval. They are given by

$$\begin{aligned} I_j^\lambda &= K\left(\frac{2\sqrt{\eta_j \sigma_\lambda}}{\eta_j + \sigma_\lambda}\right) \frac{\sigma_\lambda}{\sigma_\lambda + \eta_j} \left[\frac{1}{8}(N\eta_{\Lambda+1} - N\lambda + 1)(\lambda - \eta_\Lambda) - \right. \\ &\quad \left. - \frac{1}{4}(N\eta_{\Lambda+1} - N\lambda - 1)(\lambda + \eta_\Lambda)\right] \end{aligned} \tag{5.36}$$

and

$$J_j^\lambda = K\left(\frac{2\sqrt{\eta_j \sigma_\lambda}}{\eta_j + \sigma_\lambda}\right) \frac{\sigma_\lambda}{\sigma_\lambda + \eta_j} \left[\frac{1}{8} N(\lambda - \eta_\Lambda)^2 - \frac{1}{4} N(\lambda^2 - \eta_\Lambda^2)\right], \tag{5.37}$$

where $\sigma_\lambda = (\eta_\lambda + \lambda)/2$. The three expressions are related via the pressure balance

equation

$$P_s(\eta_j) - P_l(\eta_j) = \begin{cases} \tilde{\Pi}\left[C - \Theta^I(\eta_j)\right] & \text{if } j < \Lambda \\ \tilde{\Pi} N(\lambda - \eta_\Lambda)\left[C - \Theta^I(\eta_j)\right] & \text{if } j = \Lambda \\ 0 & \text{if } j > \Lambda \end{cases} \tag{5.38}$$

which gives us an $N \times N$ matrix of equations for the B_n. The separate expression for $j = \Lambda$ comes from the fact that the Λth interval is not completely ice-filled. The extra $N(\lambda - \eta_\Lambda)$ factor is the fraction of the interval that is occupied by ice. The reason for including this factor is to distinguish between solutions with different λ but same Λ. The final condition required to complete the system for B_n comes from the fact that at the tip of the crack we have $B_{N+1} = 0$. Hence, in matrix form we have

$$\sum_{n=1}^{N} \left[k^2 A_{jn} + C_{jn}\right] B_n = \frac{\tilde{H}\tilde{\Pi}^{1/4}}{\tilde{K}} (\underbrace{1, \ldots, 1}_{\Lambda}, N(\lambda - \eta_\Lambda), \underbrace{0, \ldots, 0}_{N-\Lambda}). \tag{5.39}$$

For $j \leq \Lambda$: $\displaystyle\sum_{n=1}^{N} \left(C_{jn} + k^2 A_{jn}\right) = \frac{\tilde{H}\tilde{\Pi}^{1/4}}{\tilde{K}}$

$n = 1$	$C_{j1} = \mu_{j1}$	$A_{j1} = (1 + \tilde{\Pi})\lambda_{j1}$
$n = 2$ to $\Lambda - 1$	$C_{jn} = \mu_{jn} - \mu_{j(n-1)}$	$A_{jn} = (1 + \tilde{\Pi})\left[\lambda_{jn} + \nu_{j(n-1)}\right]$
$n = \Lambda$	$C_{j\Lambda} = \mu_{j\Lambda} - \mu_{j(\Lambda-1)}$	$A_{j\Lambda} = \lambda_{j\Lambda} + (1 + \tilde{\Pi})\nu_{j(\Lambda-1)} + \tilde{\Pi} I_j^\lambda$
$n = \Lambda + 1$	$C_{j(\Lambda+1)} = \mu_{j(\Lambda+1)} - \mu_{j\Lambda}$	$A_{j(\Lambda+1)} = \lambda_{j(\Lambda+1)} + \nu_{j\Lambda} + \tilde{\Pi} J_j^\lambda$
$n = (\Lambda + 2)$ to N	$C_{jn} = \mu_{jn} - \mu_{j(n-1)}$	$A_{jn} = \lambda_{jn} + \nu_{j(n-1)}$

For $j = \Lambda$: $\displaystyle\sum_{n=1}^{N} \left(C_{jn} + k^2 A_{jn}\right) = N(\lambda - \eta_\Lambda)\frac{\tilde{H}\tilde{\Pi}^{1/4}}{\tilde{K}}$ with A and C defined as above with $\tilde{\Pi}$ substituted with $\tilde{\Pi}_\lambda = N(\lambda - \eta_\Lambda)\tilde{\Pi}$.

For $j > \Lambda$: $\displaystyle\sum_{n=1}^{N} \left(C_{jn} + k^2 A_{jn}\right) = 0$ with A and C defined as above with $\tilde{\Pi}$ substituted with 0.

The ice extent condition becomes

$$\frac{1}{kB_\lambda} = \tilde{H}\tilde{K}^2\left[C - \Theta_\lambda^I\right], \tag{5.40}$$

where B_λ and Θ^I_λ are the values of the cavity width and the interface temperature at the ice tip, i.e. at $\eta = \lambda$. These are found from the corresponding values at the end of the intervals $\eta = \eta_\Lambda$ and $\eta = \eta_{\Lambda+1}$ using linear extrapolation, such that

$$B_\lambda = B(\lambda) = N(\eta_{\Lambda+1} - \lambda)B_\Lambda + N(\lambda - \eta_\Lambda)B_{\Lambda+1} \tag{5.41}$$

and similarly

$$\Theta^I_\lambda = \Theta^I(\lambda) = N(\eta_{\Lambda+1} - \lambda)\Theta^I_\Lambda + N(\lambda - \eta_\Lambda)\Theta^I_{\Lambda+1}. \tag{5.42}$$

The tip condition is valid in the limit $\eta \to 1$. If we apply it at $\eta = \eta_N$ we get

$$B_N = k^{-1/2}\sqrt{1 - \eta_N} = \frac{1}{\sqrt{kN}} \tag{5.43}$$

The method we use is the following: Solve the following problem M times (default 10) each for $\lambda = m/M$, $1 < m \leq M$. For the chosen values of λ:

- Compute $\lambda_{jn}, \mu_{jn}, \nu_{jn}$ and therefore A_{jn} and C_{jn}.
- Determine the root of (5.43) to find the correct propagation rate k.
- Knowing k and λ, invert $\mathbf{G} = k^2\mathbf{A} + \mathbf{C}$ to find the B_n.
- Compute $\Theta^I(\eta_\lambda)$ from (5.32) and (5.42).
- From equation (5.40), find the value of $\kappa - \kappa_{\max}$ which should be negative for ice to be able to extend into that interval.

Finally, to find the correct value of the ice extent λ, we first check whether $\kappa - \kappa_{\max} < 0$ for all $\lambda = m/M$. If it is always negative, then the ice can extend all the way to the tip, i.e. $\lambda = 1$. If, on the other hand, all the values are positive, then the cavity is too thin and the curvature effect, described by the Gibbs-Thompson equation, doesn't allow for any ice growth. If we find both negative and positive values, we look for the maximum value λ_1 for which $\kappa - \kappa_{\max} < 0$ and the minimum value λ_2 for which $\kappa - \kappa_{\max} > 0$ and use linear extrapolation to estimate the λ for which $\kappa - \kappa_{\max} = 0$. We can improve accuracy by repeating the process in the interval (λ_1, λ_2). If for all the values of λ tried, equation (5.43) can't be satisfied for any value of k, then there is no propagation.

5.3 Results

5.3.1 Solutions

Solving the problem for a variety of parameters reveals the existence of two similarity solutions, a slowly-propagating one and a fast-propagating one. Figures 5.2 and 5.3 show the cavity shape $B(\eta)$, as well as the pressures $P_s(\eta)$ and $P_l(\eta)$, in terms of the spatial parameter η for these two situations. The region occu-

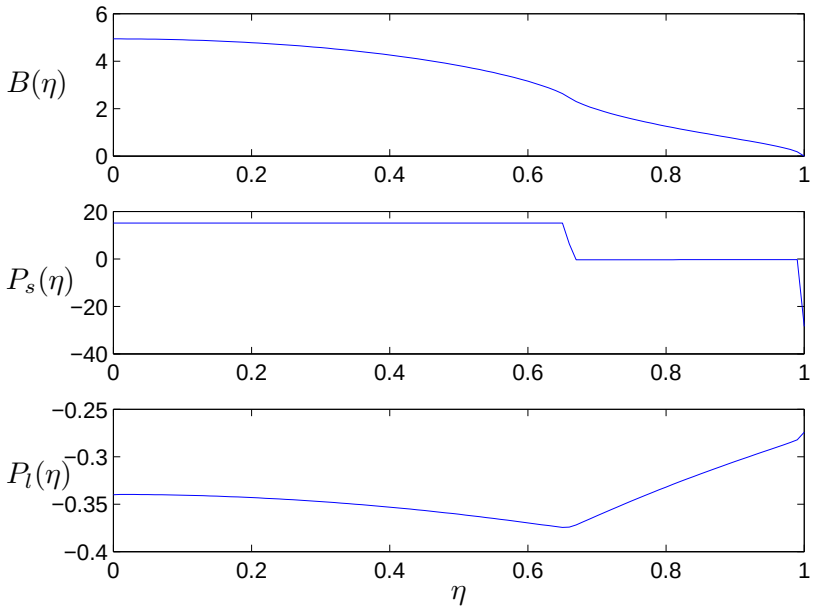

Figure 5.2: *A plot of the slow solution with $k_1 = 0.3001$: the three plots show the cavity width $B(\eta)$, the solid pressure $P_s(\eta)$ and the liquid pressure $P_l(\eta)$ against η.*

pied by ice is easily distinguishable in both cases, with $\lambda = 0.66$ for the slowly propagating case (figure 5.2) and $\lambda = 0.88$ for the fast propagating case (figure 5.3). The slow propagating crack is thicker than the fast one, agreeing with the balance $B \sim k^{-1/2}$ dictated by the tip condition (5.43), which appears to have a global effect on the cavity width. We also note that the liquid pressure P_l is an order of magnitude larger in the fast-propagating case than the slow one. This shows that the effect of water migration towards the solidification front does not affect the slow cavity as much as the fast one. This could be due to the fact that

the water freezes slowly, resulting in a smaller negative pressure and slow flow of water towards the solidification front. The large negative value of the solid pressure P_s at $\eta = 1$ agrees with the prediction of infinite solid pressure at the tip of the crack due to the parabolic shape of the tip as predicted by linear elasticity, but remains finite due to the limitations of the discretized numerical scheme we have used. The value at $\eta = 1$ is not used to determine any cavity characteristics as the pressure balance is not evaluated at the tip, hence the value of the negative peak is unimportant.

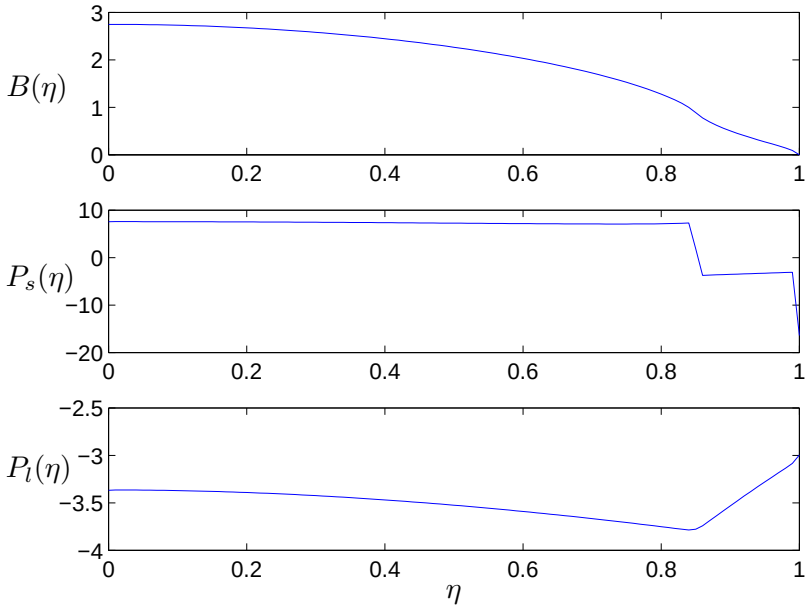

Figure 5.3: *A plot of the fast solution with $k_2 = 1.2057$: the three plots show the cavity width $B(\eta)$, the solid pressure $P_s(\eta)$ and the liquid pressure $P_l(\eta)$ against η.*

5.3.2 Phase planes

Similarity solutions do not exist for all values of the parameters $\tilde{H}$, $\tilde{K}$ and $\tilde{\Pi}$. Mathematically, although the matrix $\mathbf{C} + k^2\mathbf{A}$ can always be inverted (provided it is not singular) for a given k and λ, the tip condition (5.43) and the ice extent condition (5.40) will only hold for the right choice of k and λ. We investigate the existence and type of solutions by solving the equations for different values of these

parameters. The parameters $\tilde{H}$ and $\tilde{K}$ are the ones most directly determining the ice extent λ and propagation rate k, hence we fix the permeability $\tilde{\Pi}$ and plot phase planes of the different types of solutions in terms of the undercooling $\tilde{H}$ and the fracture toughness $\tilde{K}$. Figure 5.4 shows phase plots for both the slow (left) and the fast (right) solutions.

We find 4 different types of solutions. Two of them (red crosses and black circles) represent situations when no propagation occurs, but the reason behind this is different in each case and we shall discuss it further. The other two describe propagating cracks: the blue diamonds denote completely ice-filled cavities, with $\lambda = 1$, while the green squares represent partially-filled cracks, where $\lambda < 1$.

The red crosses indicate problems for which the stress at the tip of the crack is less than the critical value K, even for completely ice-filled cavities. Practically this means that whatever the ice extent λ, we can't find a propagation rate k for which the tip condition (5.43) is satisfied, even before we take into account the Gibbs-Thompson effect determining whether curvature allows ice to grow in the cavity for the given undercooling. This is the case where the material is tough enough to withstand the pressure caused by the build up of ice for a given undercooling ΔT. An increase in the elastic modulus m of the rock or a decrease of the fracture toughness K will result in an overall decrease of $\tilde{K}$, making the medium stiffer or less tough respectively. A weaker medium requires less pressure for fracturing hence smaller undercooling. A stiffer medium implies that the pressure build-up happens faster as the cavity doesn't deform much and hence less ice is required to maintain the pressure. The timescale of pressure build-up is important as the undercooling reduces with time. The longer the process takes, the smaller the disjoining pressure will be. Also, an increase of the undercooling $\tilde{H}$ means more ice build-up inside the cavity. Both the increase of $\tilde{H}$ and the decrease of $\tilde{K}$ result in fracturing of the cavity, as can be seen from the phase space (5.4). The boundary of the no propagation region (red crosses) looks to be determined by a linear relationship between $\tilde{H}$ and $\tilde{K}$

$$\tilde{K} = \beta(\tilde{\Pi})\tilde{H}, \tag{5.44}$$

where β is a parameter that depends on the value of the permeability $\tilde{\Pi}$.

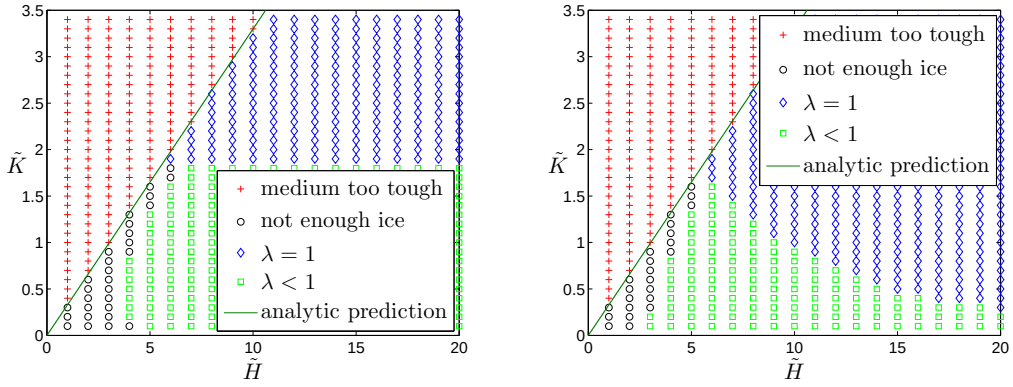

Figure 5.4: *A plot of $\tilde{K}$ against $\tilde{H}$ for $\tilde{\Pi} = 2$ showing the regions of existence of slow solutions (left) and the fast solutions (right). The dark green lines represent the slope as defined by equation* (5.47).

The smaller region shown by the black circles also describes similarity solutions where no propagation occurs. The reason we distinguish this region from the red crosses is because, while the material is not tough enough to withstand the pressure from a completely ice-filled cavity, the curvature melting effect does not allow the ice to extend all the way to the tip of the crack. We can see from figure 5.4 that this occurs for small undercoolings ΔT, indicating that the maximum curvature determined by the Gibbs-Thompson relation is small. In addition to this, the dimensionless fracture toughness is generally small, representing media that do not deform much under pressure, resulting in thin cavities. Curvature-induced melting can also affect the ice growth in solutions described by the red crosses, especially for small ΔT and small $\tilde{K}$ but, in these cases, even if we ignored the Gibbs-Thompson condition and assumed a completely ice-filled cavity, the stress at the tip would still be below the critical value K. An increase in the undercooling ΔT results in ice being able to extend further towards the tip, with the resulting stress causing fracturing. Physically, all non-propagating solutions (black circles and red crosses) will begin from an initial radius, with ice growing up to some λR and deforming them. As the stress at the tip K_I is still below the critical value K, no fracturing can occur, meaning that $k = 0$ hence $R = 0$. This shows that we cannot describe these situations in the similarity solution framework. In reality, we expect an equilibrium situation were the disjoining pressure balances the elastic pressure of the cavity. As the environment warms

up with time, the maximum curvature imposed by the Gibbs-Thompson relation decreases, resulting in the melting of ice towards the tip. We therefore expect the pressure to slowly relax and part of the ice to melt as the environment is warming, which is not captured by the characteristics of the similarity solution. We will discuss these cases more in chapter 6, where the time dependent problem is solved, allowing us to explore the initial stages of ice build-up in more detail.

The green squares describe the sets of $(\tilde{H}, \tilde{K})$ for which we can find sets of solutions (k_1, λ) and (k_2, λ) satisfying the tip and ice extent conditions, (5.43) and (5.40). The blue diamonds represent sets of parameters where solutions for k exist but the curvature of the ice tip is always less than the maximum value defined by equation (5.40), i.e. the ice can extend to the tip of the cavity and the curvature doesn't affect the extent of the ice. While we have denoted this as $\lambda = 1$, this would require the curvature of the tip of the ice to be equal to the curvature of the tip of the crack. In the model we have used here, this is represented by a parabolic tip, which results in a curvature several orders of magnitude larger than the approximate circular curvature of the ice close to the tip. This indicates that the cavity can never be completely ice-filled. Indeed, the section we have labelled as such actually represents solution for which $\lambda > 1 - 1/N$, i.e. the ice extends inside the last interval. This has a negligible effect on the results, especially for large N, and the boundary between $\lambda < 1$ and $\lambda = 1$ is useful in representing contours of constant λ. The assumption of a parabolic tip is only approximate and breaks down when within a few nm of the tip (see Lawn, 1993). In reality, the tip is more likely to be sharp, making the curvature at that point infinite. The details of what happens at such small scales close to the tip are beyond the scope of this thesis.

What is interesting is that for the slow solution k_1, shown at the left hand side of figure 5.4, there is a maximum value of $\tilde{K}$ which doesn't depend on $\tilde{H}$ and above which the cavity is completely ice-filled. In contrast, for the fast solution the threshold is affected by the value of $\tilde{H}$ and is quickly reducing for large $\tilde{H}$. The fast solution has a much larger thickness at a given time, even though its aspect ratio is smaller, as can be seen from comparing figures 5.2 and 5.3 and remembering that $k_2 \approx 3k_1$ in that case. This means that the ice can extend further into the tip as the radius of curvature is larger. As $\tilde{H}$ increases, so does

the maximum possible curvature of the ice, hence it can grow further towards the tip.

In general, a large fracture toughness $\tilde{K}$ means more ice inside the cavity. This can be seen from the phase plane of the fast solution, on the right hand side of figure 5.4, where cavities are more ice-filled for a given undercooling as $\tilde{K}$ increases. A large fracture toughness indicates that more stress at the tip is required for propagation, therefore higher pressure build-up inside the cavity is needed. This pressure is provided by more water freezing, which creates a thicker cavity, inside which the ice can extend closer to the tip. A large value of $\tilde{K}$ can also be caused by a small value of the elastic modulus m, which indicates an elastic medium deforming considerably under pressure.

5.3.3 Stability of solutions

The stress intensity factor K_I describes the stress at the tip of the crack and is a result of the loading on the cavity walls. The crack starts to propagate if K_I reaches the critical value of the fracture toughness K, and we have steady propagation for $K_I = K$. This is expressed by equation (5.43) and provides a means of determining the propagation rate k. We can also investigate how different values of k correspond to different loadings at the tip. We define a dimensionless stress-intensity factor K^* scaled with the fracture toughness K. The tip condition (5.43) now gives us the propagation rate k produced by some general stress intensity K^* at the tip

$$K^* = \sqrt{kN} B_N. \tag{5.45}$$

In this new formulation, quasi-steady propagation occurs for $K^* = 1$, i.e. where the stress-intensity factor is equal to the critical value. Figure 5.5 shows the values of the stress intensity K^* plotted against the corresponding propagation rate, with the points of quasi-steady propagation denoted by the red squares.

We can now understand how the two solutions react to small perturbations in propagation rates, therefore determining which solution is stable. We note that for $k_1 < k < k_2$, the stress intensity factor is higher than its critical value and

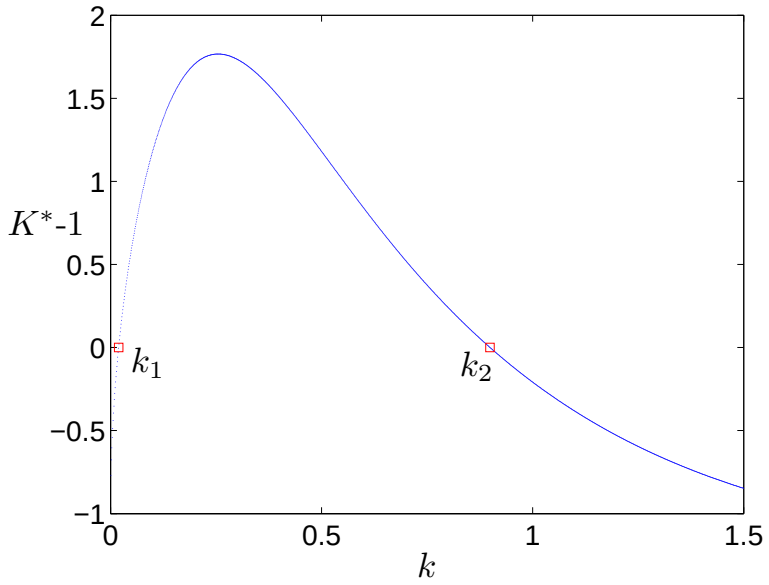

Figure 5.5: *A plot of $K^* - 1$ against the propagation rate k, showing the unstable (slow) and stable (fast) solutions.*

for $k > k_2$ or $k < k_1$ it is lower. Therefore, if the cavity propagates just faster than the slow solution, at $k = k_1 + \epsilon$ (where $\epsilon > 0$), the pressure builds up higher than the critical value. This forces the cavity to propagate even faster, making the solution unstable. For a propagation rate just slower than k_1 we end up with $K^* < 1$ therefore the propagation slows even further. Conversely, for a cavity propagating at $k = k_2 + \epsilon$, the stress-intensity factor is lower than the critical value, causing the propagation to slow down and hence making the fast solution stable.

5.3.4 Stable solution

We now focus our attention on the stable solution, which is the fast-propagating one, and analyse how the propagation and shape of the cavity depend on the different parameters of the problem. Figure 5.6 shows phase planes of solutions for different values of the fracture toughness $\tilde{K}$ (y-axis) and the undercooling $\tilde{H}$ (x-axis). The two graphs represent two different values of the permeability, with $\tilde{\Pi} = 0.02$ for the left hand side graph and $\tilde{\Pi} = 200$ for the right hand side one.

A schematic of the different stable solutions on the $\tilde{H} - \tilde{K}$ plane is shown in figure 5.7.

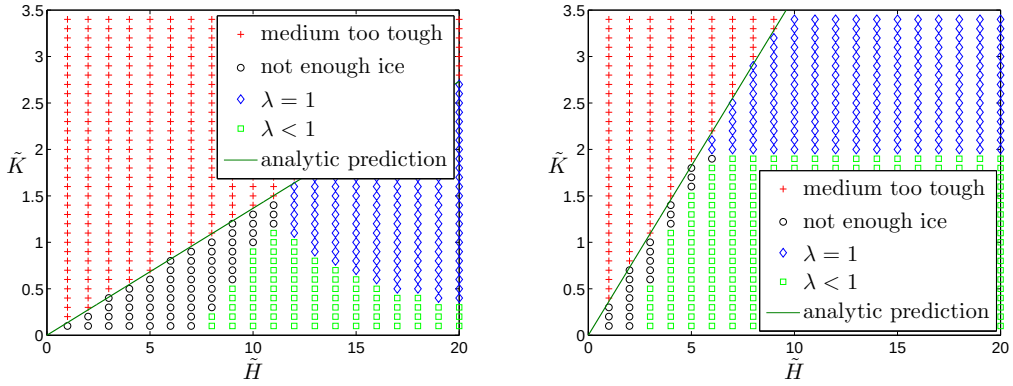

Figure 5.6: *A plot of $\tilde{K}$ against $\tilde{H}$ for $\tilde{\Pi} = 0.02$ (left) and $\tilde{\Pi} = 200$ (right) showing the regions of existence of solutions. The dark green lines represent the slope as defined by equation* (5.47).

A change in the permeability $\tilde{\Pi}$ can restrict or facilitate the flow of water towards the solidification front. We can use this to explain the effect of $\tilde{\Pi}$ on the boundary between the region of no propagation (shown by the red crosses on figure 5.6) and the solutions of either fully filled or partially filled cavities. As discussed in section 5.3.2, this is described by a linear relationship between $\tilde{H}$ and $\tilde{K}$ with the slope β depending on the permeability $\tilde{\Pi}$, as can be seen from equation (5.44).

For a very impermeable rock, as shown on the left of figure 5.6, for a given value of the fracture toughness $\tilde{K}$, the dimensionless undercooling $\tilde{H}$ required for propagation is much higher than that in the more permeable rocks. In the notation used in equation (5.44) this means that β is smaller for smaller $\tilde{\Pi}$. This is explained by the fact that in a relatively impermeable medium, the flow of water towards the freezing front is more restricted and hence the freezing and pressure build-up processes are slower. As the undercooling ΔT decreases with time, the freezing process is further slowed, resulting in insufficient stress at the tip.

To understand the linear relationship between $\tilde{K}$ and $\tilde{H}$ describing the red crosses boundary, we need to examine what changes across the boundary. Equation (5.39) describes the balance of the pressures across the premelted film for a

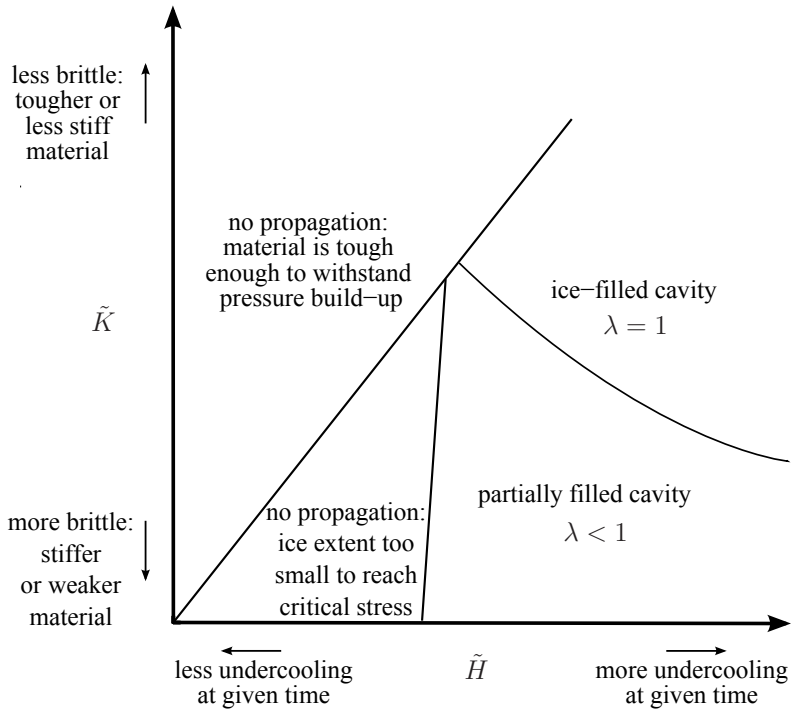

Figure 5.7: *An approximate sketch of the different regions representing the existence and type of stable solutions in a $\tilde{K}$ - $\tilde{H}$ parameter space.*

specific propagation rate k. If no k exists for which this balance is achieved, the cavity does not propagate, at least under the similarity solution framework. The tip condition (5.43) gives us that $B \sim k^{-1/2}$. We also see that while the matrix C_{jn} is independent of any of the physical parameters of the problem, A_{jn} depends on the permeability according to $A_{jn} \sim 1 + \tilde{\Pi}$. If we substitute these relations in equation (5.39), we find

$$(1 + \tilde{\Pi})k^{3/2} + k^{-1/2} \sim \frac{\tilde{H}\tilde{\Pi}^{1/4}}{\tilde{K}}. \tag{5.46}$$

The left-hand side of the expression has a minimum at $k = 1/\sqrt{3(1 + \tilde{\Pi})}$ hence, if the value of $\tilde{H}\tilde{\Pi}^{1/4}/\tilde{K}$ is smaller than that minimum, no solution for k exists. This threshold is the linear boundary described by equation (5.44) with a slope β. The fact that neither A_{jn} and C_{jn} depend on $\tilde{H}$ or $\tilde{K}$ agrees with our observation that the boundary is a straight line, therefore β is only a function of the dimensionless permeability $\tilde{\Pi}$. Substituting $\beta = \tilde{K}/\tilde{H}$ and $k = k_{\min} \sim 1/\sqrt{1 + \tilde{\Pi}}$ in equation

(5.46) we find an expression for β

$$\beta(\tilde{\Pi}) \sim \frac{\tilde{\Pi}^{1/4}}{(1+\tilde{\Pi})^{1/4}}. \tag{5.47}$$

For impermeable rocks, where $\tilde{\Pi} \ll 1$, we find that $\beta \sim \tilde{\Pi}^{1/4}$ hence the slope of the boundary increases with permeability. Since only the dependence on $\tilde{\Pi}$, rather than the exact value of the factor β, is determined by equation (5.47), we use the slope of the graph on the right hand-side of figure 5.6 to determine the slopes for the rest of the phase planes in figures 5.4 and 5.6. These are represented by the dark green lines and we see that the agreement is excellent.

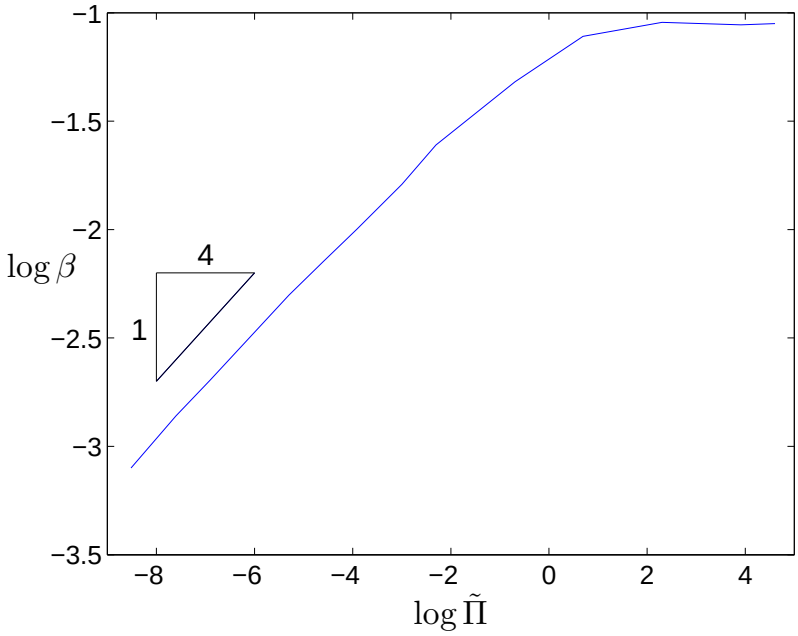

Figure 5.8: *A log-log plot of the parameter β, defined in equation* (5.44)*, against the permeability $\tilde{\Pi}$. The data for β have been obtained numerically and are in good agreement with the theoretically predicted behaviour described by equation* (5.47)*.*

We investigate this behaviour further by plotting β for more values of the permeability as shown in figure 5.8. The slopes β are obtained from $\tilde{K} - \tilde{H}$ phase planes for different values of $\tilde{\Pi}$. The results for small values of $\tilde{\Pi}$ indeed show a power law dependence of β on the permeability with the value of the

power matching the theoretically predicted value of 1/4 well. As the permeability increases, the value of the slope β tends to a constant, as is predicted by equation (5.47) for $\tilde{\Pi} \gg 1$. Physically this means that for a large enough permeability, the availability of water supply doesn't limit the propagation of the cavity. The region of no propagation becomes smaller as the permeability increases but tends to a constant for $\tilde{\Pi} \gg 1$. For these permeable rocks, the propagation is only limited by the amount of undercooling, and whether there can be enough ice growth to cause the stress at the tip to reach the critical value $\tilde{K}$.

The effect of permeability $\tilde{\Pi}$

Comparing the two graphs in figure 5.6, we notice that the permeability $\tilde{\Pi}$ strongly affects the boundary between the $\lambda = 1$ solutions (blue diamonds) and the $\lambda < 1$ solutions (green squares). In particular, as the permeability $\tilde{\Pi}$ decreases, solutions with the same $\tilde{H}$ and $\tilde{K}$ can become ice-filled.

Figure 5.9 shows the cavity thickness $\tilde{\Pi}^{-1/4}B(\eta)$, the solid and liquid pressures $\tilde{\Pi}^{-1/4}P_{s,l}(\eta)$ and the undercooling of the ice boundary $\tilde{\Pi}^{3/4}\left(\Theta^I(\eta) - C\right)$, i.e. the dimensionless $T^I - T_m$, against the spatial variable η. These functions have been plotted for two different values of the permeability, $\tilde{\Pi} = 2$ (blue solid curve) and $\tilde{\Pi} = 20$ (red dashed curve). The more permeable case, described by the dashed curve, has a smaller aspect ratio. We know from our analysis in section 5.2 that the width of the cavity W scales with $\tilde{\Pi}^{1/4}$ while the length scales with $\tilde{\Pi}^{1/2}$. As the permeability increases, both width and length increase, making the cavity longer and thicker, but the aspect ratio decreases, meaning the cavity becomes more slender. Despite this, the ice extent λ is smaller than in the impermeable case, which agrees with our observations from figure 5.6. This can be explained by considering the temperature inside the cavity in both cases: figure 5.9 shows that for the permeable one, the cavity is much warmer, making the maximum allowed ice curvature (dictated by the Gibbs-Thompson relation (5.40)) smaller.

Figure 5.10 shows that the propagation rate k decreases as the permeability increases. To understand this further, we look at how the radius of the crack is expressed in its dimensional form

$$R(t) = \left(\frac{\Pi}{\mu} m\right)^{1/2} k t^{1/2} \tag{5.48}$$

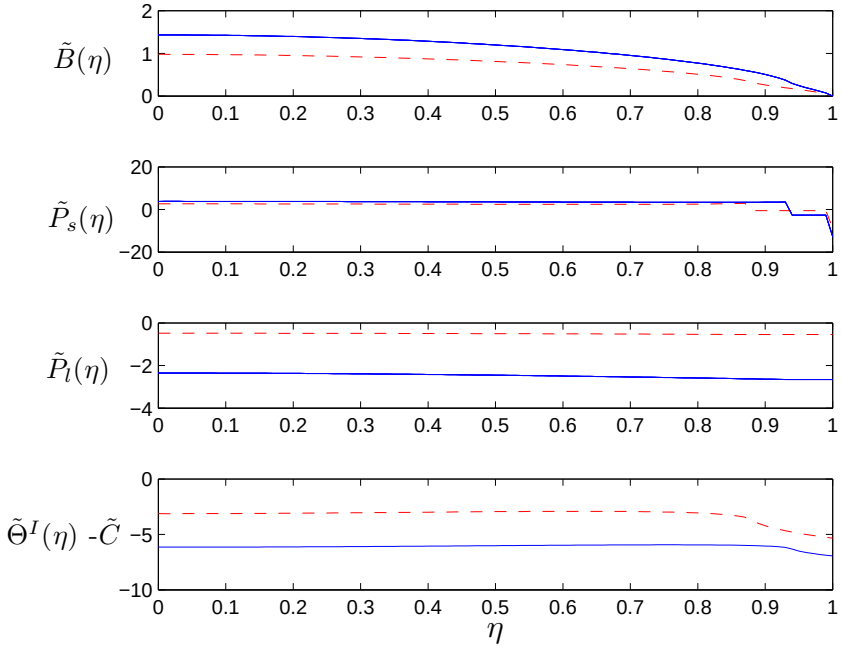

Figure 5.9: *The cavity thickness $B(\eta)$, the liquid and solid pressures $P_s(\eta)$ and $P_l(\eta)$ and the temperature field $\Theta^I(\eta)$ for two different values of the permeability $\tilde{\Pi} = 2$ (blue solid curve) and $\tilde{\Pi} = 20$ (red dashed curve). The functions are scaled appropriately with powers of $\tilde{\Pi}$ to show the dependence on the permeability correctly, e.g. $\tilde{B}(\eta) = \tilde{\Pi}^{-1/4} B(\eta)$ etc.*

hence when we vary $\tilde{\Pi}$, we need to take into account the dependence of the radius on the permeability by looking at $R \sim \tilde{\Pi}^{1/2} k$. This is also plotted on figure 5.10 and we see that at a given time t the radius is larger in the more permeable media. This is expected as there is faster supply of water, resulting in faster freezing inside the cavity and hence faster build-up of pressure. This can also explain the warmer temperature inside the cavities of more permeable media. Since the rate of freezing is larger, the Stefan condition tells us that more latent heat is released, increasing the temperature in the thin premelted film between ice and rock.

The ice extent

As discussed in section 4.1.2, the stress-intensity factor at the tip of a crack induced by a loading $p_s(r, t)$ on the inner walls of the crack can be expressed as

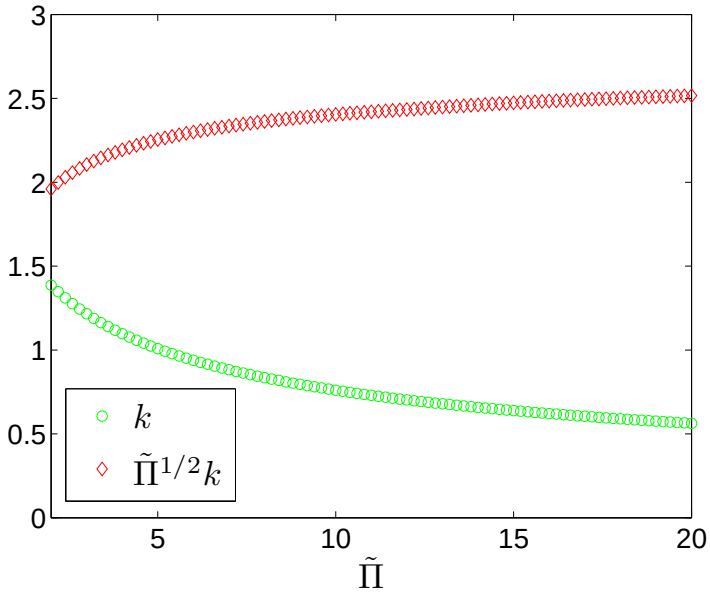

Figure 5.10: *The propagation rate k and the scaled propagation rate $\tilde{\Pi}^{1/2}k$ which represents the cavity radius, plotted against the permeability $\tilde{\Pi}$.*

an integral over p_s

$$K_I = \frac{2}{(\pi R)^{1/2}} \int_0^R \frac{r p_s(r,t)}{(R^2 - r^2)^{1/2}}\, dr. \tag{5.49}$$

When $K_I = K$, i.e. when the stress at the tip K_I, caused by the pressure distribution $p_s(r,t)$, is equal to the fracture toughness K, the expression above is equivalent to equations (5.1) and (5.9). We can see that the integral is weighted towards the stress contributions closer to the tip. For a small λ, the lack of ice (and therefore pressure) close to the tip has to be counteracted by substantial ice growth, enough to raise the stress intensity at the tip to the critical value. This implies that for smaller λ we have bigger width. The thicker the cavity though, the further the ice can extend towards the tip. The balance of these two processes leads us to the result that λ increases as $\tilde{K}$ increases, as shown in figure 5.11. There is a similar explanation for why λ increases with $\tilde{H}$, since a colder cavity will cause more water to freeze, resulting in a fatter cavity and the ice being able to extend further towards the tip of the crack.

Figure 5.11 only shows values of the ice extent λ for propagating solutions, i.e. solutions denoted by the green squares or black diamonds in figures 5.4 and

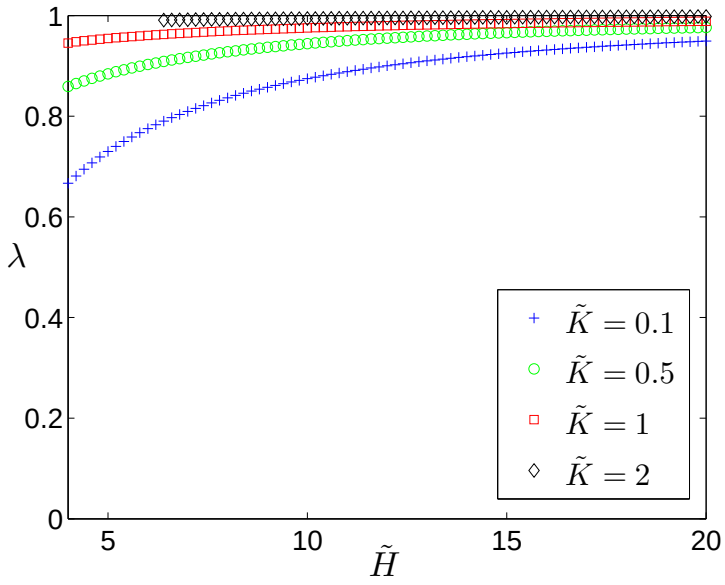

Figure 5.11: *The ice extent λ vs. the undercooling $\tilde{H}$, for different values of the fracture toughness $\tilde{K}$. We have taken $\tilde{\Pi} = 20$.*

5.6. For each value of $\tilde{K}$, there is a minimum possible value of the ice extent corresponding to a propagating solution. This is because for λ smaller than that, the stress at the tip is less than critical, hence the tip condition cannot be satisfied. This minimum value of λ decreases for decreasing $\tilde{K}$. This is a result of small cavity thicknesses, due to either stiff or weak media, meaning that the ice cannot extend far into the tip.

The propagation rate

The propagation rate depends on the freezing rate, as more water needs to freeze to maintain the stress at the tip. The faster the solidification, the quicker the pressure in the cavity builds up and the stress condition at the tip is met. This can be seen in figure 5.12 where for a given $\tilde{K}$, the propagation rate increases with $\tilde{H}$.

The propagation rate decreases as the fracture toughness $\tilde{K}$ increases, since it is easier to fracture a more brittle rock. Less pressure build-up is required inside the cavity for the tip condition to be met, resulting in faster propagation.

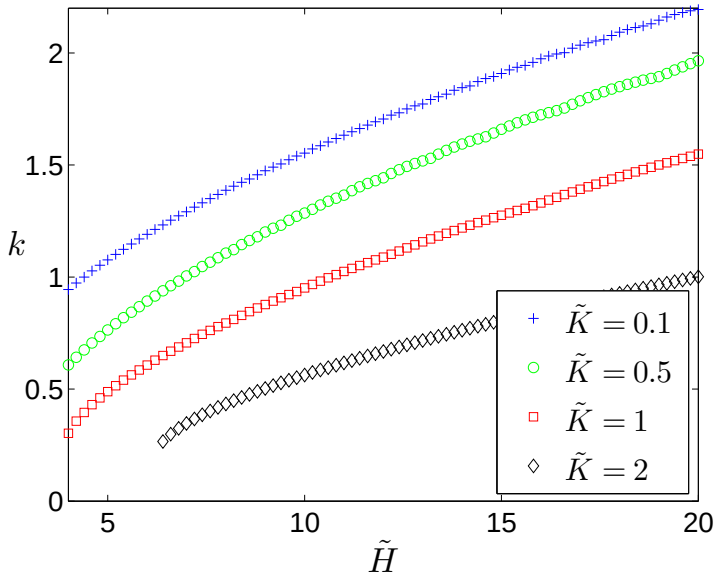

Figure 5.12: *The propagation rate k vs. the undercooling $\tilde{H}$, for different values of the fracture toughness $\tilde{K}$. We have taken $\tilde{\Pi} = 20$.*

The aspect ratio

We can look at either the aspect ratio of the cavity or the aspect ratio of the ice, though for a given λ it is straightforward to derive conclusions about one from the other. Since we have scaled the cavity width with W and the length with L, the aspect ratio scales with W/L, therefore we look at $\tilde{K}\tilde{\Pi}^{-1/4}B_1$. The tip condition (5.43) implies the balance $B \sim k^{-1/2}$, therefore we expect the aspect ratio to decrease with increasing propagation rate.

Larger undercooling means lower temperature and, using equation (5.40), we expect ice to be able to exist in thinner cavities for larger $\tilde{H}$, since there is a bigger maximum curvature allowed. Equation (5.49) shows that the stress at the tip is an integral of the pressure over all of the cavity, but heavily weighted towards the tip. With ice growing further towards the tip, we need less pressure at any given r to reach the critical fracture toughness value $\tilde{K}$. We therefore expect the aspect ratio of the cavity to be smaller as λ increases, for a given $\tilde{K}$. Figures 5.11 and 5.12 support this as we can see that, for larger undercoolings $\tilde{H}$, we have a smaller aspect ratio and a larger ice extent. As the fracture toughness increases, more pressure is needed for the crack to propagate and that pressure needs to be

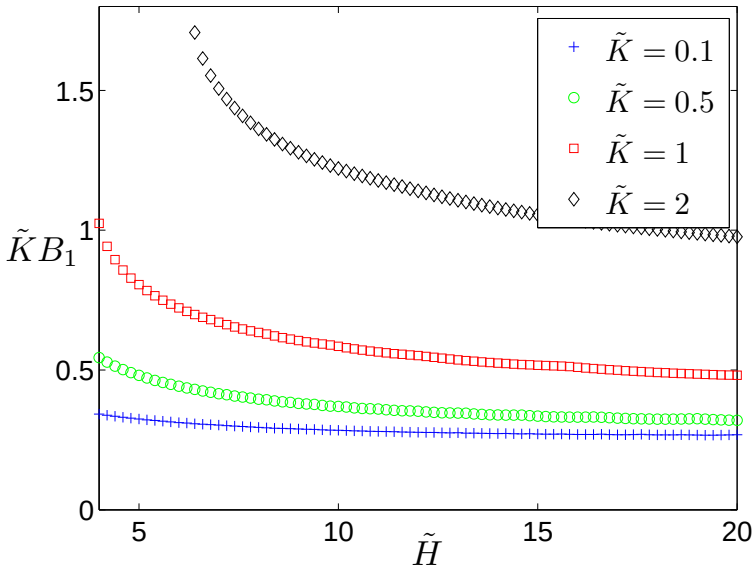

Figure 5.13: *The aspect ratio of the cavity $\tilde{K}\tilde{\Pi}^{-1/4}B_1$ vs. the undercooling $\tilde{H}$, for different values of the fracture toughness $\tilde{K}$. We have taken $\tilde{\Pi} = 20$.*

provided by more ice build-up inside the cavity. This can clearly be seen in figure 5.13, with the aspect ratio curves increasing for larger $\tilde{K}$.

The temperature field

We plot the temperature $\Theta^I - C$ against η, both inside ($\eta < 1$) and outside ($\eta > 1$) the cavity. The parameters in this case are such that $C \approx 6$, and $\Theta^I - C$ represents the difference between the interface temperature and the melting temperature, i.e. in similarity form

$$\left(\Theta^I - C\right) = t^{1/4}\frac{C}{H}\left(T^I - T_m\right). \tag{5.50}$$

We recall that the temperature problem is set so that the far-field is undercooled to some T_∞, which can be seen in figure 5.14 where for large η, $\Theta^I \to 0$. The temperature remains negative everywhere, with the cavity being warmer than the rock. The region where ice exists, which extends almost up to $\eta = 1$, has a slight variation of temperature, with the warmest region being towards the tip of the ice, at $\eta = \lambda$.

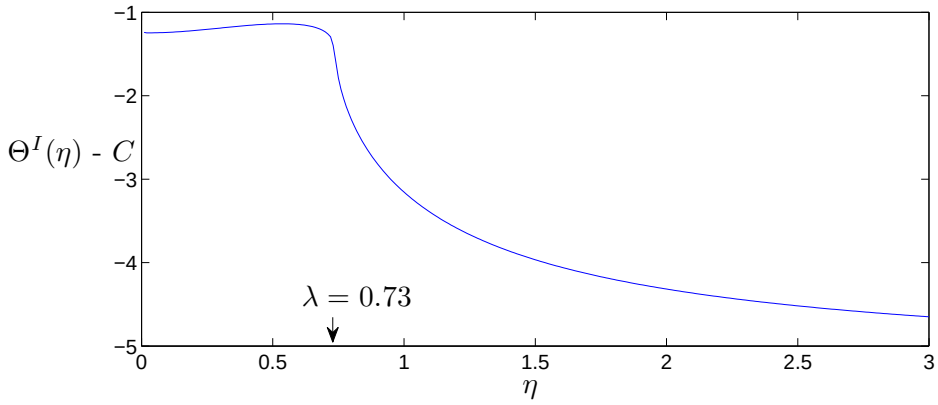

Figure 5.14: *The temperature field $\Theta^I - C$, in the cavity ($\eta < 1$) and in the rock ($\eta > 1$).*

The region around the tip of the ice is where the highest rate of solidification is, since the ice is growing both in the r and z direction. This implies that more latent heat is released there, making this region the warmest. In general, the variations of temperature for $\eta < \lambda$, i.e. the part of the cavity occupied by ice, are small compared to $\eta > \lambda$. Inside the water-filled tip of the cavity, the temperature drops rapidly as the latent heat effect from the solidification process decreases as η increases. As we move away from the cavity and into the porous medium where $\eta > 1$, the temperature decays further, tending to the undercooling ΔT as $\eta \to \infty$.

5.4 Conclusions

In this chapter, we have developed a mathematical model to describe the fracturing of penny-shaped cracks, incorporating two important features: the curvature-melting controlled extent of the ice inside the cavity, and the elastic fracturing which determines the propagation rate. We developed a similarity solution for the undercooling law $\Delta T = Ht^{-1/4}$ which produces two solutions. The characteristics of the two were studied and it was shown that only the fast solution is stable.

It was also found that propagation occurs only for certain combinations of the parameters $\tilde{H}$, $\tilde{K}$ and $\tilde{\Pi}$. The regions of no propagation were discussed and,

although their features cannot be captured by the similarity solution developed here, an understanding of why they occur and how they behave has been established. These will be studied further in the next chapter, where the time dependent problem allows us to look at the initial stages of pressure build-up.

Characteristics of the stable fracturing such as the ice extent, the propagation rate and the aspect ratio of the cavities were studied and their dependence on the dimensionless parameters $\tilde{H}$, $\tilde{K}$ and $\tilde{\Pi}$ was discussed. This allowed us to develop an understanding of the relative importance of the different parameters which will help us in our studies of the time dependent model.

An interesting feature which arises from the assumption of a warming environment is the importance of the permeability Π, which controls the time scale of flow and water supply. Since the undercooling decreases with time, media with low permeabilities can experience no fracturing, even for parameters for which more permeable media would fracture. This is due to the time-dependence of the undercooling and, since the next chapter is predominantly involved with constant undercoolings, it is an important point to take away from this study.

Chapter 6

Time-dependent problem

In chapter 5 we developed a model predicting the fracturing of a crack caused by the freezing of water in a saturated porous medium. Linear elasticity, which predicts propagation when the stress at the tip of the cavity reaches a critical value, is coupled with the Darcy flow and temperature field equations to produce a system of coupled integral relations that can be solved for the shape and radius of the cavity. A similarity solution was found for the special case of background undercooling $\Delta T \sim t^{-1/4}$. For thin cavities, the curvature at the tip of the ice can become large. The Gibbs-Thompson relation (2.11) is taken into account when determining the extent of the ice inside the cavity, as it defines the maximum ice curvature for a given undercooling. We found a parameter regime for which the ice cannot extend all the way to the tip of the crack, because of the phenomenon of curvature-induced melting.

Having a similarity solution that incorporates all the important features of the problem is extremely useful and has allowed us to derive many interesting conclusions about how the different parameters of the problem affect the crack propagation. Using the understanding we have gained, we are now better equipped to solve the full time-dependent problem. This is important for several reasons, not least because it allows us to consider a general undercooling law and easily change from a uniform undercooling to a power law like the one used in chapter 5.

Furthermore, we can study not only the long-time behaviour of the crack, where the process has developed and the pressure build-up is causing the cavity to propagate, but also the initial stage of ice growth. This is characterized by the stress at the tip K_I being below the critical value K and therefore the crack does not propagate. During this stage, the cavity thickness increases as a result of the ice formation and subsequent pressure build-up, while the stress at the tip K_I approaches the critical value K. The ice extent λ is a complicated function of the undercooling of the surrounding and the thickness of the cavity, and this framework allows for it to vary with time. We will, in general, keep the analysis in this chapter dimensionless, as we are mainly interested in exploring the qualitative dependence of fracturing on the different parameters of the problem. Applications of the theory to different rocks and soils are presented in chapter 7.

6.1 Dimensional time-dependent problem

The set-up of the problem is more or less identical to the one presented in section 5.1. We consider the surrounding environment to be undercooled to the constant value $\Delta T = T_m - T_\infty > 0$, but note that it is straightforward to modify this to a power law and incorporate it into our algorithm if we want to draw comparisons with the similarity solution. As before, the solid and liquid pressure integrals are given by

$$p_s(r,t) = -\frac{2}{\pi} m \fint_0^{R(t)} M^*\left(\frac{r}{s}\right) \frac{\partial b}{\partial s} \frac{ds}{s}, \tag{6.1}$$

$$p_l(r,t) = -\frac{2}{\pi} \frac{\mu}{\Pi} \int_0^{R(t)} K\left(\frac{2\sqrt{rs}}{r+s}\right) \frac{\partial b}{\partial t} \frac{s\,ds}{s+r}, \tag{6.2}$$

while the temperature is

$$\theta^I(r,t) = T^I(r,t) - T_\infty = \frac{2}{\pi}\frac{\rho_s \mathcal{L}}{k_l}\int_0^{\lambda R(t)} K\left(\frac{2\sqrt{rs}}{r+s}\right)\frac{\partial b}{\partial t}\frac{s\,ds}{s+r}. \tag{6.3}$$

These are connected via the pressure balance:

$$p_s(r,t) - p_l(r,t) = \begin{cases} \dfrac{\rho_s \mathcal{L}\Delta T}{T_m} - \dfrac{\rho_s \mathcal{L}}{T_m}\theta^I(r,t) & \text{if } r \le \lambda R. \\ \\ 0 & \text{if } r > \lambda R. \end{cases} \tag{6.4}$$

The ice extends to $r = \lambda(t)R(t)$, where the parameter λ is determined by the Gibbs-Thompson relation

$$\frac{2\gamma}{b(\lambda R,t)} = \frac{\rho_s \mathcal{L}\Delta T}{T_m} - \frac{\rho_s \mathcal{L}}{T_m}\theta^I(\lambda R(t),t). \tag{6.5}$$

It is important to remember that λ can vary with time, unlike in the similarity solution frame, and hence will have to be computed at every time step. When the stress at the tip reaches the critical value, the cavity propagates according to

$$b(r,t) \sim \frac{K}{m}\left[\frac{8(R-r)}{\pi}\right]^{1/2} \quad \text{as} \quad r \to R. \tag{6.6}$$

6.2 Scalings

We scale the equations for pressure, length, width, temperature and time with p^*, $R_0 = R(t_0)$, W, θ^* and t^*. The following scalings arise

$$W = \sqrt{\frac{8}{\pi}}\frac{K}{m}R_0^{1/2}, \tag{6.7}$$

$$p^* = \frac{2}{\pi}\sqrt{\frac{8}{\pi}}R_0^{-1/2}K, \tag{6.8}$$

$$\theta^* = \frac{2}{\pi}\sqrt{\frac{8}{\pi}}R_0^{-1/2}\frac{\rho_s \mathcal{L}\Pi}{\mu k_l}K, \tag{6.9}$$

$$t^* = \frac{\mu}{\Pi m}R_0^2. \tag{6.10}$$

The pressure balance and ice extent conditions now become

$$p_s(r,t) - p_l(r,t) = \begin{cases} \dfrac{\tilde{H}}{\tilde{K}} - \tilde{\Pi}\theta^I(r,t) & \text{if } r \le \lambda R \\ \\ 0 & \text{if } r > \lambda R \end{cases}$$

and

$$\frac{1}{b(\lambda R,t)} = \tilde{K}^2 \left(\frac{\tilde{H}}{\tilde{K}} - \tilde{\Pi}\theta^I(\lambda R(t),t) \right), \tag{6.11}$$

where the pressures p_s and p_l, the temperature θ^I and the width $b(r,t)$ are now dimensionless. The new constants that we introduced $\tilde{\Pi}$, $\tilde{K}$ and $\tilde{H}$ represent the dimensionless permeability, fracture toughness and undercooling respectively, as in chapter 5, although their definitions are slightly different:

$$\tilde{\Pi} = \frac{\rho_s^2 \mathcal{L}^2 \Pi}{\mu k_l T_m}, \tag{6.12}$$

$$\tilde{H} = \sqrt{\frac{\pi R_0}{4\gamma m}} \frac{\rho_s \mathcal{L} \Delta T}{T_m}, \tag{6.13}$$

$$\tilde{K} = \frac{4}{\pi} \frac{K}{\sqrt{2\gamma m}}. \tag{6.14}$$

We map the $[0,R]$ interval to $[0,1]$ by setting $\eta = r/R(t)$. Then

$$\frac{\partial \eta}{\partial r} = \frac{1}{R(t)} \quad \text{and} \quad \frac{\partial \eta}{\partial t} = -\frac{rR'(t)}{R^2(t)}. \tag{6.15}$$

We also let $B(\eta,t) = b(r,t)/R(t)$ in order to preserve the aspect ratio. Then

$$\frac{\partial b(r,t)}{\partial r} = \frac{\partial B(\eta,t)}{\partial \eta} \tag{6.16}$$

and

$$\frac{\partial b(r,t)}{\partial t} = R(t)\frac{\partial B(\eta,t)}{\partial t} + R'(t)\left(B(\eta,t) - \eta \frac{\partial B(\eta,t)}{\partial \eta} \right). \tag{6.17}$$

Then, the equations describing the system become

$$P_s(\eta,t) = -\fint_0^1 M\left(\frac{\eta}{\sigma}\right) \frac{\partial B(\sigma,t)}{\partial \sigma} \, \frac{d\sigma}{\sigma}, \tag{6.18}$$

$$P_l(\eta,t) = -\int_0^1 K\left(\frac{2\sqrt{\eta\sigma}}{\eta+\sigma}\right) Q(\sigma,t)\frac{\sigma\, d\sigma}{\sigma+\eta} \tag{6.19}$$

and

$$\Theta^I(\eta,t) = \int_0^\lambda K\left(\frac{2\sqrt{\eta\sigma}}{\eta+\sigma}\right) Q(\sigma,t)\frac{\sigma\, d\sigma}{\sigma+\eta}, \tag{6.20}$$

where

$$Q(\sigma,t) = \left\{ R(t)\frac{\partial B(\sigma,t)}{\partial t} + R'(t)\left[B(\sigma,t) - \sigma\frac{\partial B(\sigma,t)}{\partial \sigma}\right]\right\} R(t). \tag{6.21}$$

The pressure balance simply becomes

$$P_s(\eta,t) - P_l(\eta,t) = \begin{cases} \dfrac{\tilde{H}}{\tilde{K}} - \tilde{\Pi}\Theta^I(\eta,t) & \text{if } \eta \le \lambda. \\ \\ 0 & \text{if } \eta > \lambda. \end{cases}$$

The ice extent is determined by

$$\frac{1}{R(t)B(\lambda,t)} = \tilde{K}^2\left(\frac{\tilde{H}}{\tilde{K}} - \tilde{\Pi}\Theta^I(\lambda,t)\right) \tag{6.22}$$

and the condition on the crack propagation comes from

$$B(\eta,t) \sim R(t)^{-1/2}\sqrt{1-\eta}, \quad \text{as } \eta \to 1. \tag{6.23}$$

6.3 Numerical scheme

We again split $[0,1]$ in N intervals. The edges of the intervals are $\eta_n = (n-1)/N$ and the values of the cavity width there are $B_n(t) = B(\eta_n, t)$. We denote the values at the ith iteration with the superscript i so that $B_n^i = B_n(t^i)$. We denote the time step by Δt such that $t^i = t_0 + i\Delta t$. As the method used here is almost identical to that in section 5.2.1, we skip the details, which can be found in Appendix B. For a given λ^i and R^i, we have the following linear problem to solve.

For $j < \Lambda$: $A^i_{jn} B^i_n = C^i_{jn} B^{i-1}_n + \tilde{H}\tilde{K}^{-1}$ where

$$\begin{aligned}
A_{jn} &= \left[\mu_{jn} - \mu_{j(n-1)}\right] + (1+\tilde{\Pi})\left[\alpha_{jn}\beta^i_n + \alpha_{j(n-1}\gamma^i_n\right] && n < \Lambda \\
&= \left[\mu_{jn} - \mu_{j(n-1)}\right] + \alpha_{jn}\beta^i_n + (1+\tilde{\Pi})\alpha_{j(n-1)}\gamma^i_n + \tilde{\Pi}\alpha^i_{j\lambda}\beta^i_\lambda && n = \Lambda \\
&= \left[\mu_{jn} - \mu_{j(n-1)}\right] + \alpha_{jn}\beta^i_n + \alpha_{j(n-1)}\gamma^i_n + \tilde{\Pi}\alpha^i_{j\lambda}\gamma^i_\lambda && n = \Lambda + 1 \\
&= \left[\mu_{jn} - \mu_{j(n-1)}\right] + \alpha_{jn}\beta^i_n + \alpha_{j(n-1)}\gamma^i_n && n > \Lambda + 1 \\
\\
C_{jn} &= \left[\alpha_{jn} + \alpha_{j(n-1)}\right](1+\tilde{\Pi}){R^i}^2 && n < \Lambda \\
&= \left[\alpha_{jn} + (1+\tilde{\Pi})\alpha_{j(n-1)}\right]{R^i}^2 + \tilde{\Pi}\alpha^i_{j\lambda}\delta^i_\lambda && n = \Lambda \\
&= \left[\alpha_{jn} + \alpha_{j(n-1)}\right]{R^i}^2 + \tilde{\Pi}\alpha^i_{j\lambda}\epsilon^i_\lambda && n = \Lambda + 1 \\
&= \left[\alpha_{jn} + \alpha_{j(n-1)}\right]{R^i}^2 && n > \Lambda + 1
\end{aligned} \tag{6.24}$$

For $j = \Lambda$ we have $A^i_{jn} B^i_n = C^i_{jn} B^{i-1}_n + N(\lambda^i - \eta_\Lambda)\tilde{H}\tilde{K}^{-1}$ and also $\tilde{\Pi}$ is substituted by $\tilde{\Pi}_\lambda = N(\lambda^i - \eta_\Lambda)\tilde{\Pi}$.

For $j > \Lambda$ we have $A^i_{jn} B^i_n = C^i_{jn} B^{i-1}_n$ with

$$\begin{aligned}
A_{jn} &= \left[\mu_{jn} - \mu_{j(n-1)}\right] + \alpha_{\Lambda n}\beta^i_n + \alpha_{\Lambda(n-1}\gamma^i_n, \\
C_{jn} &= \left[\alpha_{\Lambda n} + \alpha_{\Lambda(n-1)}\right]{R^i}^2.
\end{aligned} \tag{6.25}$$

The matrices α_{jn} and μ_{jn}, vectors β^i_n, γ^i_n and $\alpha_{j\lambda}$, and the factors β^i_λ, γ^i_λ, δ^i_λ and ϵ^i_λ are defined in Appendix B.

The ice extent λ^i is found via

$$\frac{1}{R^i B^i_\lambda} = \tilde{H}\tilde{K} - \tilde{\Pi}\tilde{K}^2 {\Theta^I}^i_\lambda, \tag{6.26}$$

$$\begin{aligned}
\text{where} \quad B^i_\lambda &= N(\eta_{\Lambda+1} - \lambda^i)B^i_\Lambda + N(\lambda^i - \eta_\Lambda)B^i_{\Lambda+1}, \\
{\Theta^I}^i_\lambda &= N(\eta_{\Lambda+1} - \lambda^i){\Theta^I}^i(\eta_\Lambda) + N(\lambda^i - \eta_\Lambda){\Theta^i}^I(\eta_{\Lambda+1}),
\end{aligned} \tag{6.27}$$

and the new radius comes from the tip condition

$$B^i_N = \frac{1}{\sqrt{N R^i}}. \tag{6.28}$$

Technical details

We give a brief outline of the algorithm used to solve the problem described above.

- Choose initial condition
- Compute time-independent matrices μ_{jn} and α_{jn}.
- For the ith iteration, for a number of values of λ^i equally spaced around λ^{i-1}, do the following:
  - Use a least squares routine to find the value of R^i that satisfies the tip condition;
  - Now that we know R^i for each of the values of λ^i, we can find B_n^i by computing A_{jn} and C_{jn} and inverting the matrix;
  - Compute the curvature at the tip of the ice using equation (6.28) for every λ^i.
- We pick the largest λ^i for which $\kappa - \kappa_{\max} < 0$ (or use linear interpolation between this and the next (positive) value to find a more accurate solution). Figure 6.1 shows that $\kappa - \kappa_{\max}$ is an increasing function of λ^i.
- We now have found the correct ice extent λ^i that satisfies Gibbs-Thompson. We can now find the radius R^i that satisfies the tip condition and then solve for the thickness B_n^i.

6.4 Initial condition

An advantage of solving the time-dependent problem is that we can investigate the initial stages of ice formation and pressure build-up, rather than just looking at the propagation at the critical state $K_I = K$. A simple way of thinking about how a situation like this can develop in nature is to imagine a pre-existing fault, with some ice growing inside it. Initially, the stress at the tip is sub-critical and hence no fracturing occurs. Instead, water keeps freezing inside the non-propagating cavity, causing it to increase in thickness. This in turn increases the pressure applied on the rock, and subsequently the stress at the tip. When the critical value is reached, the propagation begins.

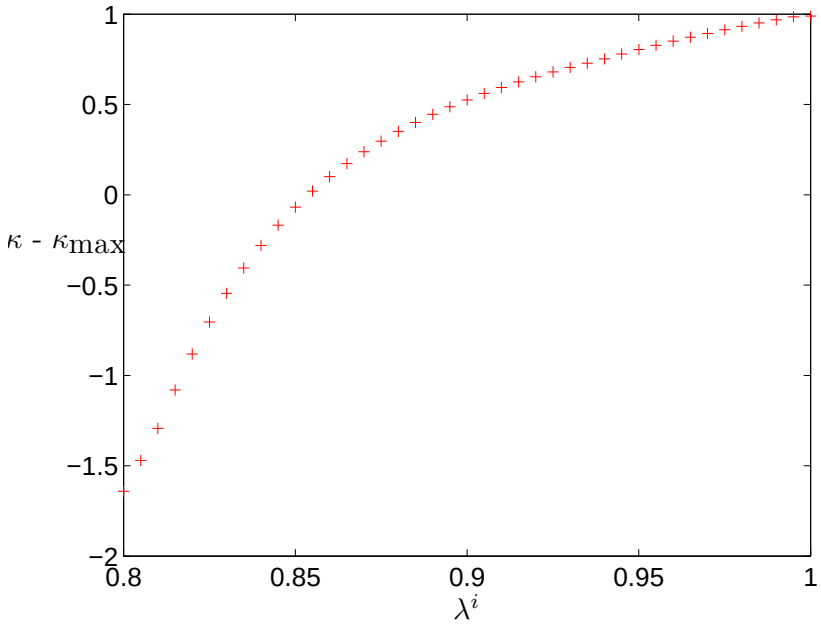

Figure 6.1: *A plot of the curvature of the tip relative to the maximum curvature allowed by Gibbs-Thompson $\kappa - \kappa_{max}$ vs. different ice extents λ^i. The correct value of λ^i is found for $\kappa - \kappa_{max} = 0$.*

6.4.1 Elliptic cavity of chosen thickness

We start with an elliptic cavity which implies a uniform pressure distribution and hence there are two initial parameters to specify: the thickness of the cavity B_1^0 and the initial ice extent λ^0. Firstly we note that the value of λ^0 is not important if the cavity shape is fixed, hence we take $\lambda^0 = 0$. The thickness of the cavity will affect the ability of the ice to grow inside it. For a given value of undercooling, there is a minimum radius of curvature of ice defined by the Gibbs–Thompson equation. The initial fault is required to have a thickness larger than this critical nucleation radius. It is also important to assume an initial thickness that results in a tip stress smaller than the critical value K, as otherwise the cavity would already be propagating. An elliptic cavity with $K_I = K_{\text{initial}}$ at the tip is given by

$$B_n = K_{\text{initial}} \sqrt{\frac{N}{2N-1}} \sqrt{1 - \frac{(n-1)^2}{N^2}}. \tag{6.29}$$

The higher the value of K_{initial}, the thicker the cavity is. This means that there is more stress at the tip and the cavity is closer to the critical state. Note that the initial condition doesn't necessarily satisfy the Gibbs–Thompson relation and a value for λ needs to be found in the first time iteration. This means that even

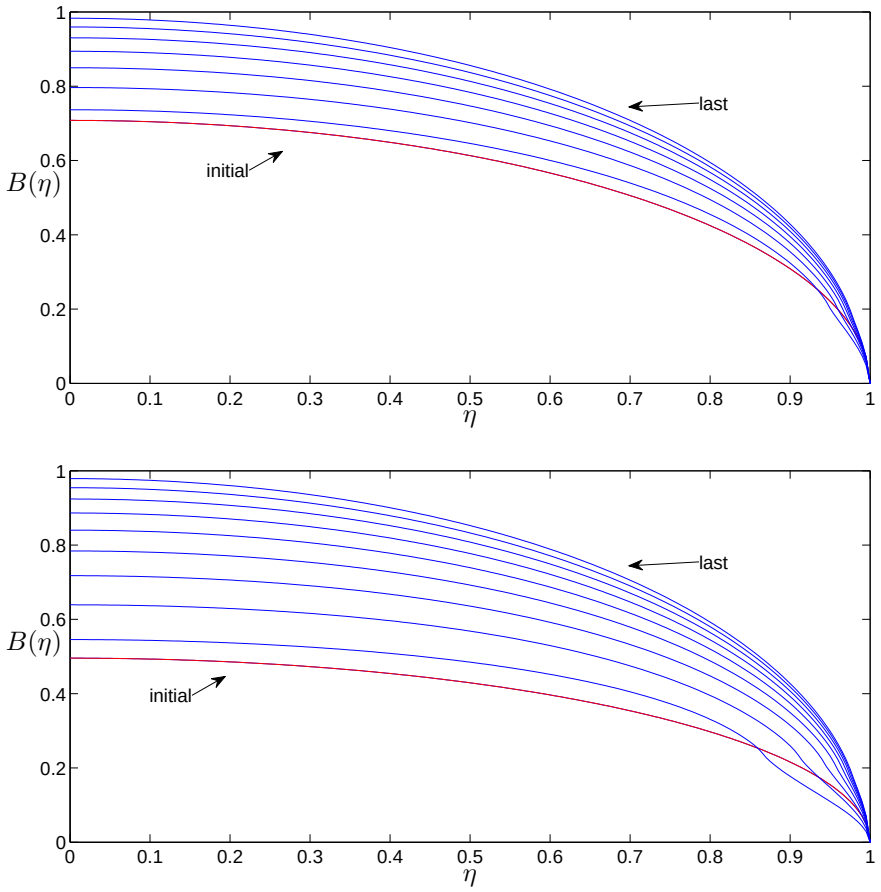

Figure 6.2: *Initial cavity growth where at the top we have chosen the initial thickness to be $K_{initial} = 1$ and at the bottom $K_{initial} = 0.7$. While the initial value of λ differs, the final cavity shape is the same.*

if $K_{\text{initial}} = K$, i.e. equal to the critical value, the next time step can produce a cavity with $K_I < K$ as the cavity shape adjusts to the new value of λ. An example can be seen in the top graph of figure 6.2. Although the elliptic shape of the initial condition has $K_{\text{initial}} = 1$ and hence satisfies the tip condition for propagation, after the first time step the cavity has $\lambda < 1$ and it becomes thinner closer to the tip, resulting in a non-elliptic shape. The stress at the tip is now sub-critical, i.e. $K_I < K$. After a few iterations, the critical stress at the tip is

reached. During the initial pressure build-up stage, we calculate the cavity shape evolution and the ice extent with $R = 1$, until the tip stress reaches the critical value and the cavity fractures.

Our choice of initial thickness will affect how far the ice can grow into the cavity initially and figure 6.2 shows that when we start with a small initial thickness (bottom graph), the first ice extent λ is smaller too, as expected. At the top, we have chosen $K_{\text{initial}} = 1$ while the bottom figure has $K_{\text{initial}} = 0.7$. The important conclusion from figure 6.2 is that the difference in the initial condition doesn't change the final shape of the non-propagating cavity, which is when $K = K_I$, and therefore represents the initial condition for propagation. The aspect ratios of the two final shapes differ by about 0.4%.

6.4.2 Critical stress unreachable

Depending on the properties of the porous medium and the undercooling of the surroundings, cases exist in which the pressure induced by the ice on the rock is not enough to make the cavity propagate. If the cavity is completely ice-filled, the ice growth is limited by the back pressure from the rock. In that case, the maximum pressure has been achieved but the induced stress at the tip is not large enough to cause fracturing. In cases of small undercoolings or very stiff rocks (hence very thin cavities), the equilibrium is reached with the ice extent $\lambda < 1$. This is a result of curvature melting as described by the Gibbs–Thompson relation (6.5). Since the ice cannot grow further into the tip of the crack, no more pressure build-up is possible. An example can be seen in figure 6.3 where the ice has reached the maximum extent it can achieve and the back pressure from the rock on the ice is preventing any further freezing. The stress at the tip for this example is about half the value of the critical fracture toughness K and therefore no propagation occurs in this case. This effect is mainly a result of insufficient undercooling and/or large fracture toughness which means that more pressure is required for propagation. The elasticity of the medium can become important since it affects the extent of the ice and hence the pressure distribution inside the cavity. As expected, this effect is independent of the initial cavity thickness we choose and corresponds to the "no propagation" regions discussed in section 5.3.2.

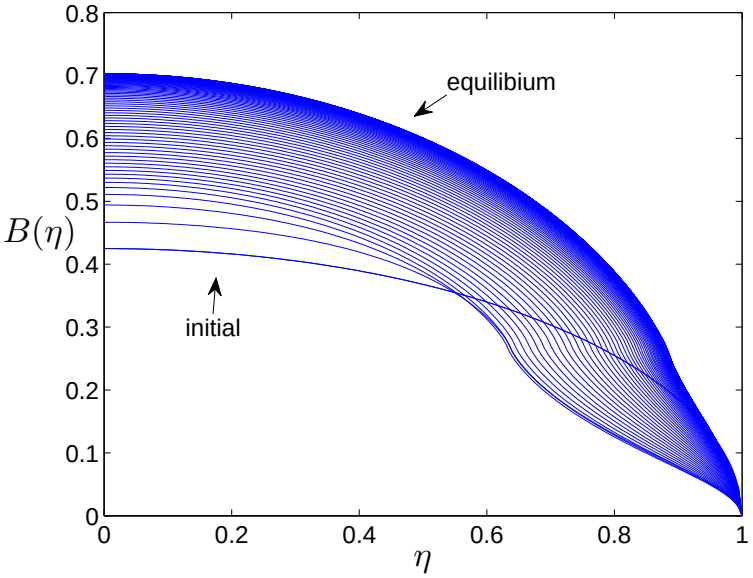

Figure 6.3: *Initial cavity growth where the critical tip stress is unreachable. The back pressure from the rock is balancing the disjoining pressure and ice cannot grow anymore.*

6.5 Comparison with similarity solution

A useful and straightforward check for the time-dependent numerical scheme is to introduce a variable undercooling such as in section 5.2 and compare the results with those from the similarity solution. To avoid confusion, we denote the dimensionless similarity solution parameters as $\tilde{H}_w$, $\tilde{K}_w$ and $\tilde{\Pi}_w$. Comparing them with the dimensionless parameters of the time-dependent problem, as defined by equations (6.12)-(6.14), we find

$$\tilde{\Pi} = \tilde{\Pi}_w, \quad \tilde{K} = \tilde{K}_w \quad \text{and} \quad \tilde{H} = \tilde{H}_w \tilde{\Pi}_w^{1/4} \tilde{t}^{-1/4}. \tag{6.30}$$

The dependence of the undercooling $\tilde{H}$ on $\tilde{\Pi}_w$ comes from the fact that $\tilde{H}$ now describes a rate of undercooling. The time dependence comes through $\tilde{\Pi}_w$ as that is the main factor that sets the time scale of the problem as described by relation (6.10). Using these relations, we can solve the time-dependent problem for a warming environment and compare it to similarity-solution results produced for the same parameters of undercooling, fracture toughness and permeability.

For the specific example shown in figures 6.4–6.6 we have used $\tilde{H}_w = 7$,

$\tilde{\Pi}_w = 10$ and $\tilde{K}_w = 0.1$. In figure 6.4, we plot the shape of the cavity $B(\eta, t)$ at a given time t_* (solid curve) while the dashed-dotted curve is the similarity shape $B(\eta)$. The time t_* is after a few iterations of the time-dependent problem to allow the cavity to converge to the similarity shape. The cavities are scaled so that $B(0)$ is the same in both cases, for more accurate comparison of their shape. The aspect ratio agreement is shown in figure 6.5. The dashed-dotted

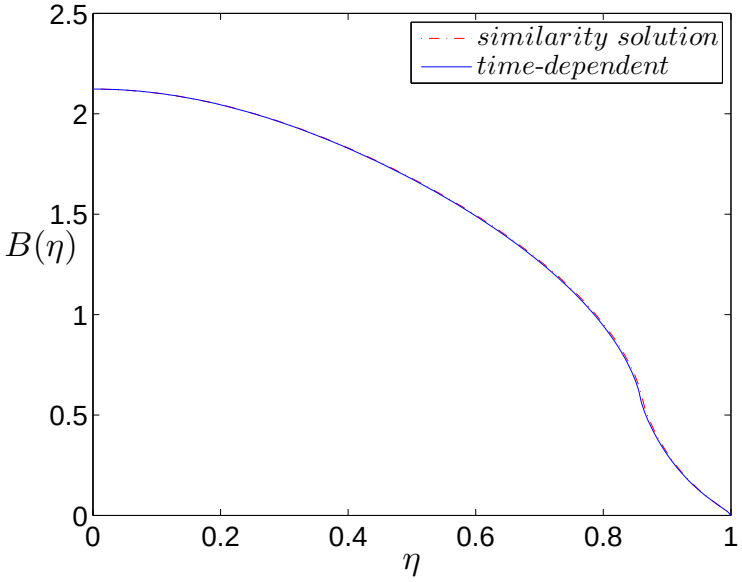

Figure 6.4: *The cavity shape from the similarity solution (red dashed curve) and the time-dependent code with adjusted undercooling (blue solid curve).*

curve is the aspect ratio behaviour of the similarity solution which behaves like $t^{-1/4}$. The same decay with time can be seen for the time-dependent aspect ratio, and the agreement between the two curves is very good. Finally, the extent of the ice $\lambda(t)$ and the radius of the crack $R(t)$ can be compared in figure 6.6. For the similarity solution, the ice extent λ is constant, and the $\lambda(t)$ value of the time-dependent problem quickly converges to the uniform value. The radius of the time-dependent cavity also agrees with the similarity solution $t^{1/2}$ power law, as expected. The fact that the similarity solution is reproducible by the time-dependent problem with the appropriate temperature boundary condition indicates that the similarity solution is an attractor.

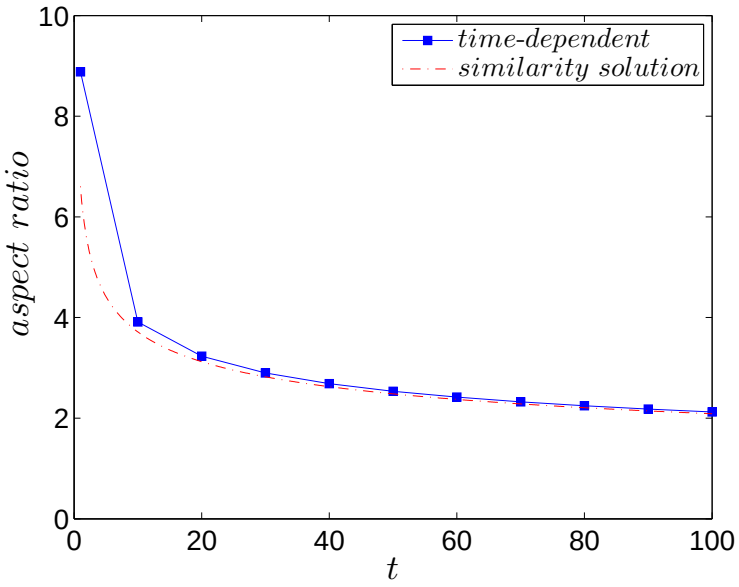

Figure 6.5: *The evolution of the aspect ratio of the cavity. We see that the time dependent results (blue squares) are in good agreement with the $t^{-1/4}$ behaviour predicted by the similarity solution (red dashed-dotted curve).*

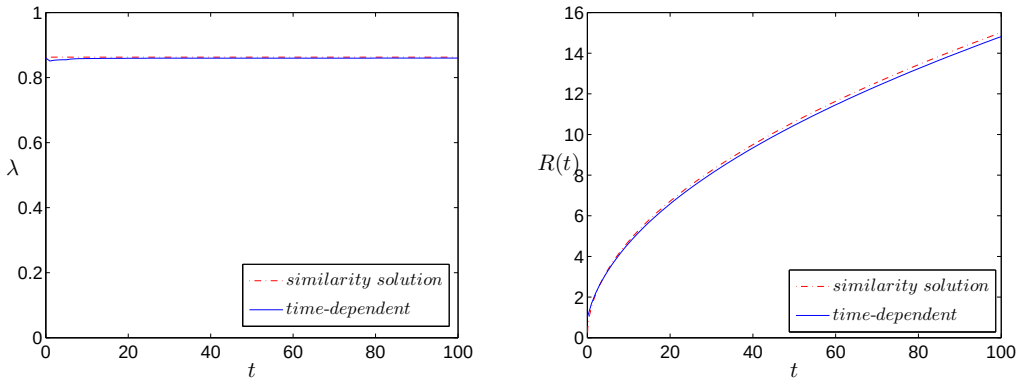

Figure 6.6: *The ice extent λ (left) and the radius $R(t)$ of the cavity (right) as given by the similarity solution (dashed curve) and the time-dependent problem (solid curve).*

6.6 Growth curves

With the previous section serving as a useful check of the time-dependent code in the case of $\Delta T \sim t^{-1/4}$, we now focus our attention again on constant undercoolings ΔT. When the undercooling is large enough, the initial period of pressure

build up inside the cavity results in the stress at the tip reaching the critical value K. This causes the cavity to fracture as can be seen in the example plotted in figure 6.7. The water continues to freeze, applying more pressure on the rock and ensuring that the stress at the tip remains at the critical value. While the ice growth causes the cavity to expand and become thicker, we note that the aspect ratio decreases with time, making the cavity more slender.

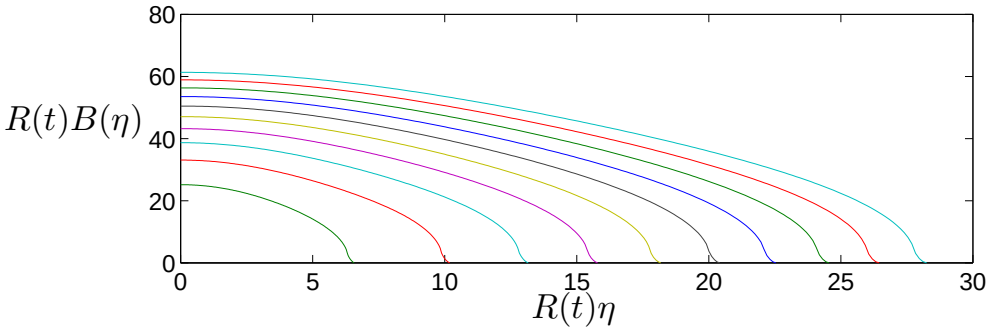

Figure 6.7: *Time plots of the cavity shape $R(t)B(\eta)$ evolving with time. Parameters used are $\tilde{\Pi} = 4$, $\tilde{H} = 10$ and $\tilde{K} = 0.1$.*

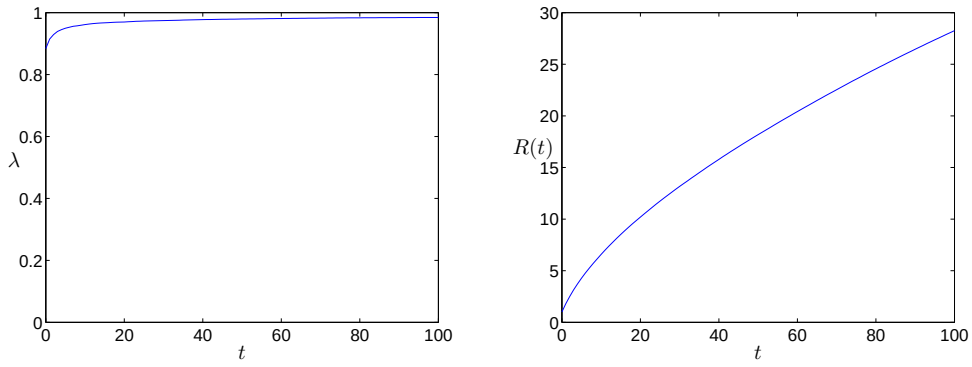

Figure 6.8: *Plot of the ice extent λ (left) and the radius of the cavity $R(t)$ (right) against the time t. Parameters used are $\tilde{\Pi} = 4$, $\tilde{H} = 10$ and $\tilde{K} = 0.1$.*

We also plot the ice extent λ and the cavity radius $R(t)$ against time in figure 6.8. An interesting feature here is that the ice extent increases with time. This is in contrast to the constant ice extent we found from the similarity solution in chapter 5. The difference is because of the behaviour of the temperature field in

the two scenarios. In chapter 5 we assumed a warming environment; the smaller undercoolings at later times result in a smaller value for the maximum curvature as defined by the Gibbs-Thompson relation (6.5). The straightforward conclusion of this is that ice extends less inside a cavity in warmer environments. This is counteracted by the increasing thickness of the cavity with time, and hence, for the warming system, the ice extent λ remains constant with time. In the case of constant undercooling, which is described in this section, the maximum curvature remains constant while the thickness of the cavity increases and, as a result, the ice can extend further towards the tip.

The plot on the right-hand side of figure 6.8 describes the growth of the crack with time. There are several features associated with these growth curves, and their characteristics will be investigated in the remainder of this chapter.

6.6.1 The effect of undercooling

The stress build-up inside the cavity is clearly dependent on the temperature of the surrounding medium. We saw earlier that for very small undercoolings, the pressure build-up is not enough to overcome the cohesion forces of the rock and cause it to fracture. We expect faster propagation to occur for greater undercoolings of the surrounding, as described by figure 5.12 in chapter 5 for the similarity solution.

In figure 6.9 we have plotted the growth curves $R(t)$ vs. t for different values of the undercooling ΔT. We see that the change in temperature affects both the initial stage of pressure build-up inside the cavity as well as the propagation rate of the crack. For smaller undercoolings, it takes longer for the stress at the tip to reach the critical value. It is important to note here that the minimum value of the undercooling ΔT for propagation to occur at all is just below 8 K for this specific example. The maximum disjoining pressure acting between the ice and the rock through the premelted film is a linear function of ΔT and is given by

$$p_T = \frac{\rho_s \mathcal{L} \Delta T}{T_m}. \tag{6.31}$$

This shows how the maximum pressure the ice can exert on the rock is limited by the value of the undercooling. As the critical value of the stress at the tip

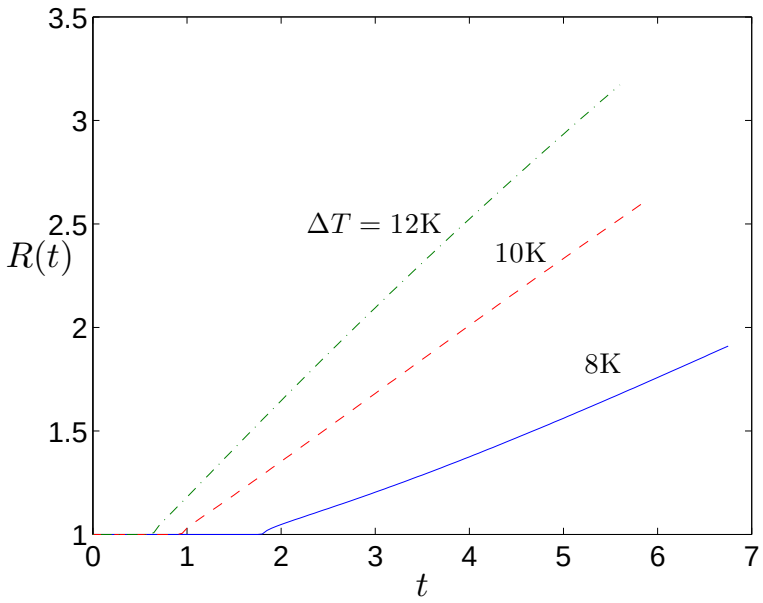

Figure 6.9: *Growth curves of the radius of the cavity $R(t)$ vs. time t for different values of the undercooling ΔT.*

is reached and the crack extends, more water has to freeze to fill the now larger cavity and build up the stress again. At lower temperatures, the solidification is faster, meaning that a faster cavity propagation rate can be sustained.

An increase of the fracture toughness K has a similar effect to a decrease of ΔT, slowing propagation down as more water is needed to freeze to maintain the critical state $K_I = K$. There is a linear relationship between the temperature and the disjoining pressure as demonstrated by equation (6.31), as well as the stress intensity at the tip as shown by equation (4.16). This implies that the ratio of the fracture toughness of the medium over the undercooling, $K/\Delta T$, is important in determining the propagation rate.

6.6.2 The effect of permeability

As we saw in section 5.3.4, the permeability of the rock affects the time scale of propagation as well as the ability of a cavity to fracture. Direct comparisons with the conclusions derived from the warming scenario have limited use as, in that

case, the permeability of the medium indirectly affects the undercooling of the environment through the time scale. The permeability limits the flow of water towards the freezing front and hence the solidification process. In the warming scenario, if it takes a long time for the ice and the pressure in the cavity to build up (i.e. small permeability), then the undercooling is reduced and hence the ability of the ice to fracture the cavity is limited. When the undercooling of the medium is not time dependent, the permeability will simply affect the propagation rate rather than the fracturing potential. This will be discussed further in section 7.4.

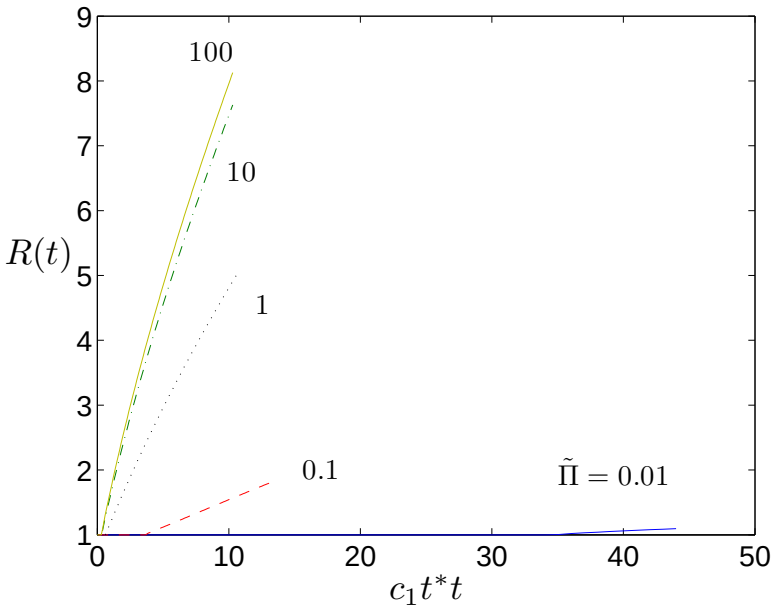

Figure 6.10: *Growth curves of the radius of the cavity $R(t)$ vs. time t for different values of the permeability Π.*

To study the effect of Π on the growth curves, we recall that the timescale t^* depends on the permeability Π. To take this into account, we plot $R(t)$ against $c_1 t^* t$ as shown in figure 6.10, where the parameter $c_1 = mk_l T_m/(\rho_s^2 \mathcal{L}^2 R_0^2)$ makes $c_1 t^* t$ dimensionless. The timescale t^* ensures that the correct dependence of the growth rate on Π is shown. As expected, the permeability has a big effect on both the time scale of the initial phase as well as the growth rate of the cavity. This effect is larger for very small permeabilities: in the $\tilde{\Pi} = 0.01$ case (blue solid curve), the build-up time is about 5 times longer than in the $\tilde{\Pi} = 0.1$ case

(red dashed curve) and the growth rate about 5 times slower. In contrast, the $\tilde{\Pi} = 1$ (black dotted curve) build up time is just twice longer than the $\tilde{\Pi} = 10$ one (green dash-dotted curve) and the growth rate only slower by a factor of 1.5. From this, we deduce that the permeability of the medium affects the solidification and propagation rates by controlling the flow of water towards the freezing front. For very low permeability media such as granite, this effect is especially strong and dominates the time scales of the problem. As the medium becomes more permeable, the resistance to the flow of water isn't as strong and we see that for $\tilde{\Pi}$ greater than about 10, it becomes negligible.

6.6.3 The effect of initial radius

We can intuitively guess that rocks with smaller pre-existing faults will be less prone to fracturing at a certain undercooling. The maximum solid pressure on an ice-filled crack is given by the disjoining pressure as

$$p_s = p_l + p_T \leq p_T \leq \frac{\rho_s \mathcal{L} \Delta T}{T_m}, \tag{6.32}$$

as the liquid pressure p_l is negative. This means that the maximum possible pressure is dependent on the undercooling. The stress intensity factor at the tip is given as an integral of the solid pressure over the crack and we can see that its maximum value will come from the uniform $p_s(r,t) = p_T$ pressure distribution such that

$$K_I = \frac{2}{\sqrt{\pi R}} p_T \int_0^R \frac{r\ dr}{\sqrt{R^2 - r^2}} = \frac{2}{\sqrt{\pi}} p_T R^{1/2}. \tag{6.33}$$

This is simply the pressure distribution where the maximum solid pressure, given by equation (6.32), is attained along the whole crack. There is no propagation for $K_I < K$, where K is the fracture toughness of the material, hence, for a given undercooling ΔT, we need

$$R_0 > R_{\min} = \frac{\pi K^2 T_m^2}{4 \rho_s^2 \mathcal{L}^2 \Delta T^2} \tag{6.34}$$

for the initial cavity to start fracturing. Expressing the stress at the tip as the integral of the pressure over the crack shows that, if the pressure has a maximum value, the stress intensity factor will not reach the critical value when the

length of the crack is too small. As mentioned before, this estimate corresponds to completely ice-filled cracks, since it requires the disjoining pressure p_T to be applied along the whole crack surface. If the ice extends to only $\lambda R < R$, then the condition becomes

$$R_0 > \frac{R_{\min}}{1 - \sqrt{1 - \lambda^2}}. \tag{6.35}$$

Of course, the factor λ is a complicated function of the undercooling and the rock properties, and this criterion becomes less straightforward. We can view $R_{\min}$ as a lower bound for the minimum radius for propagation but remember that not all faults of initial radius greater than $R_{\min}$ are guaranteed to fracture. For the example presented in figure 6.11, which is a limestone with $K = 0.87\,\mathrm{MPa\,m^{1/2}}$ for undercooling of $\Delta T = 15\,\mathrm{K}$, we find that $R_{\min} \approx 0.21\,\mathrm{cm}$, which is in agreement with our numerical results. This is further investigated in section 7.4.2.

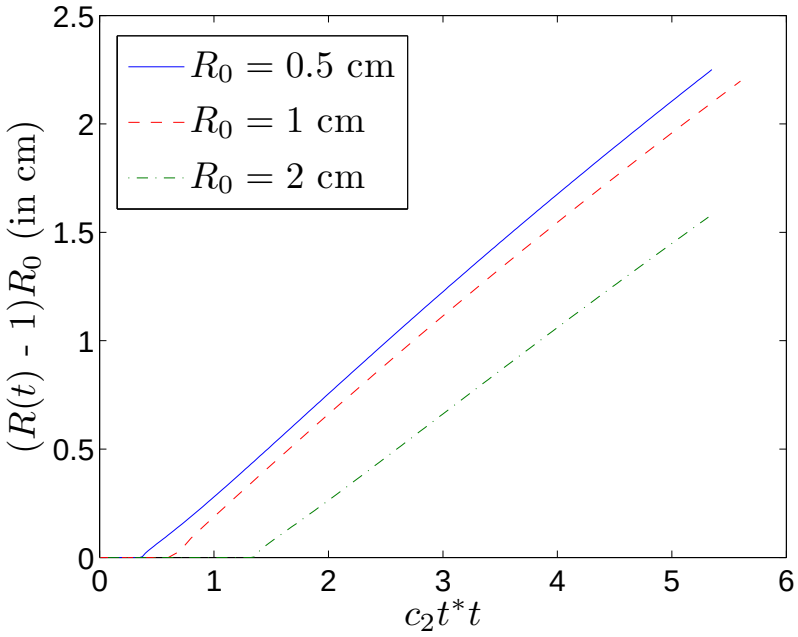

Figure 6.11: *Growth curves of the radius of the cavity $R(t)$ vs. time t for different values of the initial radius R_0. No propagation for $R_0 < 0.21\,\mathrm{cm}$.*

We are also interested in how the initial size of the cavity affects the propagation rate for initial radii $R_0 > R_{\min}$. In figure 6.11 we have plotted growth curves for three different values of R_0. In the main figure, we plot $(R(t) - 1)R_0$ against the time t which gives us the cavity *growth* against time. Since the timescale

$t^* \sim R_0^2$, we need to account for its dependence on the initial radius. We do that by plotting against the real time t^*t, multiplied by $c_2 = \frac{\pi^2 \Pi}{16\gamma^2 m\mu}\left(\frac{\rho_s \mathcal{L}\Delta T}{T_m}\right)^4$ to keep it dimensionless. We see that, the smaller the initial radius, the less time it takes for the critical stress condition to be reached and the propagation to start. This does not contradict the $R_{\min}$ conclusions above; the maximum pressure in a cavity is reached faster when the cavity is smaller as less freezing is required. If $R_0 < R_{\min}$, the tip stress caused by this maximum pressure is not enough to fracture the cavity. For $R_0 > R_{\min}$, the propagation will occur as soon as $K_I = K$.

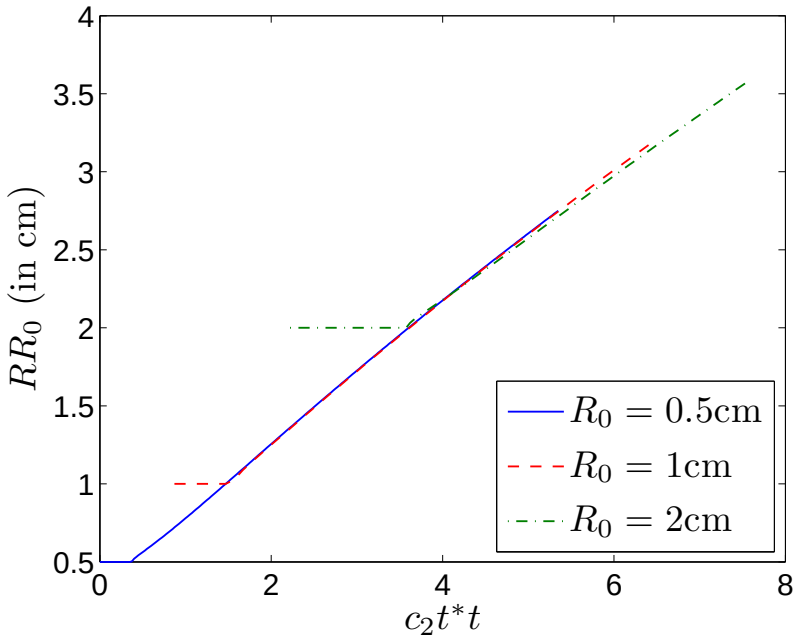

Figure 6.12: *Growth curves of the radius of the cavity $R(t)$ vs. time t for different values of the initial radius R_0. No propagation for $R_0 < 0.21\,\text{cm}$. Note that the time origin has been shifted between the curves.*

Comparing the three different growth curves we see that their slopes are very similar. We investigate this further by plotting the actual crack half radius $R(t)R_0$ against the time t in figure 6.12. Like in figure 6.12, we plot the radius against $c_2 t^* t$ to take into account the dependence of the timescale on R_0. The curves for $R_0 = 1\,\text{cm}$ and $R_0 = 2\,\text{cm}$ are shifted in time to match the $R_0 = 0.5\,\text{cm}$ curve at $R_0 R(t) = 1\,\text{cm}$ and $R_0 R(t) = 2\,\text{cm}$ respectively. It is interesting that the three curves appear now to completely coincide. This tells us that the propagation rate at any time is only dependent on the cavity radius at that time and not on the

initial radius R_0. Hence, a crack that started from an R_0-sized fault and one that started from a $2R_0$-sized fault will propagate in an almost identical way if we ignore the initial time it takes for the smaller cavity to reach $R(t) = 2R_0$. This important conclusion means that the initial condition we use only has an important effect on the fracturing potential of the crack rather than the rate of fracturing.

6.6.4 Growth characteristics

The rate of fracturing of the cavity depends on several parameters of the problem, a few of which we investigated in sections 6.6.1-6.6.3. The propagation rate depends on both the undercooling and the fracture toughness of the medium. A rock being prone to fracturing means that the fracture toughness K is small. Tough rocks will require large pressures for the stress at the tip to reach the critical value K. We saw that the maximum pressure is temperature dependent as described by equation (6.32) and that faster propagation is predicted for larger undercoolings, as the solidification is faster.

We plot the growth curves for both a weak (small K) and a tough (large K) rock in figures 6.13 and 6.14. We notice there is a qualitative difference between the two: for the weak rock, propagation is fastest for early times. Meanwhile, for the tough rock, early propagation is slow but speeds up for $t > 10$. This is accompanied by a contrasting behaviour of the solid and liquid pressures p_s and p_l, which are plotted, averaged over the length of the crack, on the right hand side of figures 6.13 and 6.14.

In both cases, there is a contrasting behaviour of the absolute values of the pressures: while $|p_l|$ increases with time, supplying the cavity with an increasing flux of water, p_s decreases. The latter behaviour is easily explained if we consider the integral expression (4.16) for the stress at the tip induced by a given solid pressure distribution: as the crack extends, the region over which the solid pressure acts is larger. The stress-intensity factor is the integrated p_s over the whole crack and, during propagation, is equal to the fracture toughness of the material which is a constant. As the cavity extends, the integral of the pressure over it remains

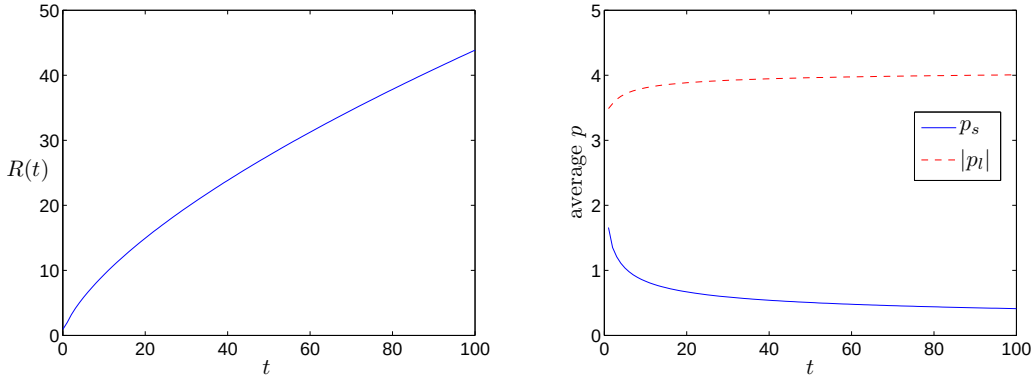

Figure 6.13: *The growth curve $R(t)$ (left) and average pressures $\bar{p}_s$ and $\bar{p}_l$ (right) against time t for a weak rock. The fracture toughness of the medium is $K = 0.5\,\mathrm{MPa} \cdot m^{1/2}$ and the undercooling is $\Delta T = 21K$.*

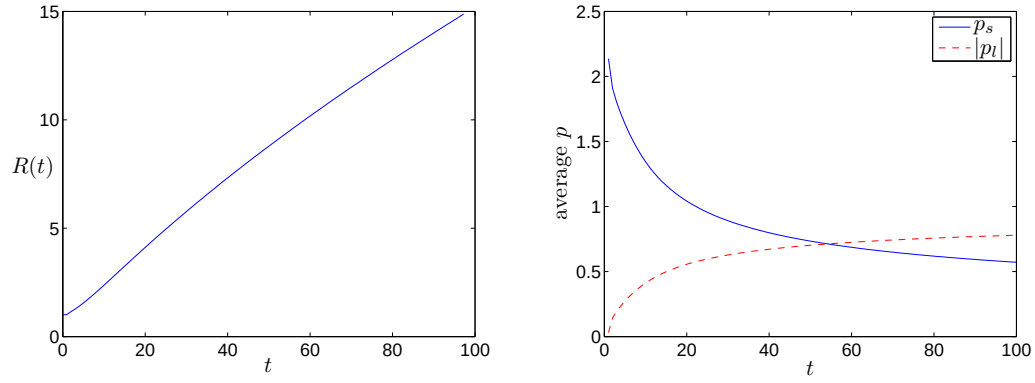

Figure 6.14: *The growth curve $R(t)$ (left) and average pressures $\bar{p}_s$ and $\bar{p}_l$ (right) against time t for a tough rock. The fracture toughness of the medium is $K = 2\,\mathrm{MPa} \cdot m^{1/2}$ and the undercooling is $\Delta T = 21K$.*

constant despite being integrated over a larger region and therefore, the value of p_s at every r is smaller.

The difference between the behaviour of the two growth curves is even clearer when we compare the liquid pressure graphs (dashed curve) on the right hand side of figures 6.13 and 6.14 . For the weak rock we see that the absolute value of the liquid pressure is much larger than the solid pressure, indicating fast freezing of the water and rock expansion which requires a lot of water. The situation is reversed for the tough rock, with the liquid pressure being several orders of magnitude smaller than the solid pressure at early times, but increasing as the

propagation continues. As expected, during the faster propagation stages, $|p_l|$ is larger than initially. When $|p_l| \ll p_s$, we have limited flow of water to the crack and hence slow freezing and pressure build-up. In all cases, the later stages of propagation are characterized by a liquid pressure of comparable or larger magnitude to the solid pressure.

In general, the ratio $|p_l|/p_s$ increases with time. The faster changes occur for $t < 1$, i.e. for times less than the timescale t^*. This timescale is derived by balancing the two pressures p_s and p_l and its value is given by the ratio of the coefficients of the pressure integrals, as described by equation (6.10). It is therefore expected that for $t \ll t^*$ we expect smaller $|p_l|/p_s$ ratios than for later times $t \gg t^*$.

For the example demonstrated in figures 6.13 and 6.14 we have used a value for the permeability corresponding to a limestone, which gives us a time scale of $t^* = 6$ sec. This shows that, in this case, the initial slow growth only occurs for the first minute of the propagation. As the timescale is inversely proportional to the permeability, for more impermeable media this behaviour can extend to hours.

6.7 Conclusions

In this chapter, we have developed a mathematical model for the fracturing of a penny-shaped cavity which incorporates both the tip stress rule for propagation as well as the curvature-induced melting phenomenon defining the ice extent. The time-dependent problem can be solved for a variety of temperature boundary conditions.

We have been able to capture both the initial stage of ice growth, where there is no fracturing and the pressure in the cavity is building up, as well as the fracturing regime. This has allowed us to identify parameter regimes for which ice growth and pressure build-up occur in an initial fault but do not cause fracturing. Small undercoolings in tough materials cause insufficient stress at the tip, while very stiff rocks result in thin cavities that limit ice growth due to the curvature-melting effect. All these can result in non-propagating cavities.

Assuming that the cavities are ice-filled, we have identified a lower bound for the initial radius of a pre-existing fault which will fracture under given fracture toughness and undercooling parameters. The expression can also be used to determine the minimum undercooling required to fracture a cavity of a given initial radius in a medium of a given fracture toughness.

We have also studied the effect of the different parameters of the problem on the growth rate of the cavity. Larger undercooling or smaller fracture toughness both result in faster fracturing. The permeability of the medium controls the flow of water towards the solidification front. This means that it has the potential to slow down the pressure build up and hence propagation, especially for relatively impermeable media with permeabilities less than about $10^{-11}\,\mathrm{cm}^2$.

We also find that, although the size of the initial cavity determines whether propagation occurs or not, according to equation (6.34), it doesn't have an effect on the later stages of propagation. Cavities that have reached the same size after starting from different initial radii will propagate in the same way.

The propagation characteristics were also discussed in relation to the balance of the liquid and solid pressures. We found that, in general, low $|p_l|$ corresponds to slow propagation and this normally occurs at the beginning of the fracturing of a tough rock. At later times, rocks can have liquid pressures of the order of the solid pressure.

In conclusion, the important features of crack propagation and their dependence on the several parameters of the problem have been identified and analysed. In the next chapter, we will apply the theory developed here to real-life scenarios and compare the results with existing studies in rock fracturing.

Chapter 7

Applications

In the last two chapters we explored the penny-shaped crack model for different undercooling laws. We found a similarity solution for specific undercooling conditions and solved the more general time-dependent problem. The geometry we considered is applicable to several real-life situations in which media with pre-existing faults are supercooled to some temperature from all sides. Examples include cracked pots, damaged buildings, historical monuments or statues and many more. Even when the precise geometry is not suitable, much can be deduced from the various scalings emerging from the modelling.

7.1 Past studies

The theoretical model for frost cracking developed by Walder & Hallet (1985) describes the propagation of an elliptical crack in a porous medium. The main conclusions of the study have been summarized in the introduction. Linear elasticity

was used to describe the pressure distribution, with the solid pressure uniformly distributed on the crack walls (see also the elliptical solution from section 4.2.1).

Unlike our model, in which we assume that propagation occurs only in the critical state $K_I = K$, Walder & Hallet consider subcritical growth of cracks, occurring for values of stress below the fracture toughness K. Subcritical fracturing can happen owing to several factors, the most usual being stress corrosion. The stress is still required to be above a critical value, which is called the stress-corrosion limit K_{s-c}. This is usually assumed to be in the region of $0.3K - 0.4K$, although difficulties in performing experiments while maintaining the stress at such low values creates some uncertainty. Sub-critical growth is assumed to occur for a range of values of the tip stress $K_I > K_{s-c}$, and not just one critical value. Because of this, it is necessary to determine the propagation rate of the crack caused by different stresses K_I. This is usually based on results from load-fracturing experiments, where a prescribed stress intensity K_I is imposed and the speed of the crack, V, is measured. Several equations, based on data from experiments described above, have been proposed to describe subcritical growth. The most used are the power law $V \sim (K_I/K)^n$ (Charles, 1958), the exponential $V \sim e^{K_I}$ (Wiederhorn & Bolz, 1970), as well as $V \sim e^{K_I^2/K^2}$ (Segall, 1984) which is the one used by Walder & Hallet. As discussed by Atkinson (1984), because the dependence of the crack growth rate V on the stress K_I is strong, and the data sets quite limited in range, it is difficult to distinguish between the different models. In addition to this, it is not clear if all materials have a stress-corrosion limit, and hence experience subcritical fracturing, as most experimental evidence concerns glasses and there is limited data on rocks and ceramics (Freiman, 1984).

The V vs. K_I law is coupled with a mass conservation of water, relating the amount of ice freezing inside the cavity and the water flow required for it, in terms of the hydraulic resistance of the cavity. Through that, Walder & Hallet compute the radius of the cavity against time. In contrast to this, our model only predicts cracking for $K_I = K$, hence the propagation rate is directly determined by the pressure balance across the premelted interface and does not rely on empirical observations. Two terms contribute to the resistance to the flow into the cavity: the permeability of the medium, and the resistance to flow from the liquid layer of thickness h at the crack wall. The inverses of the two terms, proportional to $1/\Pi$ and $1/h^3$, are added to give the flow resistance factor R_f. For example, a

larger permeability offers less resistance to the flow. The second term corresponds to the spreading of the water when it exits the pores of the surrounding medium into the liquid film inside the crack and, according to Walder & Hallet (1985), can dominate R_f for small undercoolings (not much pore ice) or coarse grains. In our model, we recognise that the premelted film is too thin for significant flow to be occurring along the length of the cavity (see section 4.1.3). We assume though that the size of the grains is small enough for the spreading of the water as it enters the film to not present significant resistance to the flow. While this can become significant for grain sizes of a few mm, the rocks considered here will have considerably smaller grains. For example, one of the most coarse-grained rocks is granite, with a grain size of 0.75 mm (Atkinson & Rawlings, 1981), but it is a relatively impermeable rock, hence its permeability dominates the flow resistance. More permeable media like limestones or clays are much finer-grained, resulting in a similar balance.

So far, we have ignored the effect that the porosity ϕ of the medium has on the flow of water into the cavity. In some cases though (e.g. clays), ϕ can be as large as $0.4 - 0.5$, and hence its effect can become important. This will be analysed in section 7.4.1. The existence of a frozen fringe is also discussed in later sections of this chapter.

Walder & Hallet applied their model to examples of granite and marble for both sustained freezing and gradual cooling with a linear temperature variation with time. The growth rates predicted are slow, of the order of mm in tens of hours. Especially at low temperatures, their theory predicts considerable amounts of pore ice and hence very low effective permeability which restricts the water flow towards the solidification front. This slows down the freezing and therefore the pressure build-up. As a result, they find that in most cases the most effective fracturing occurs at temperatures between -5° C and -14° C, as for smaller undercoolings there is not enough ice growth and pressure build-up, while at larger undercoolings the process is significantly slowed down owing to the large amount of pore ice restricting the water flow. This interval for "optimal fracturing" is supported experimentally by Hallet *et al.* (1991), who used acoustic emissions to detect fractures in a frozen rock. It is important to note here that, at low temperatures, the Walder & Hallet model predicts *slower* fracturing, rather than no fracturing at all. For example, the instantaneous growth rate for a crack in

granite is found (numerically) to be zero after 50 hours of freezing at -20° C, but after 100 hours, fracturing is predicted. This is in agreement with our model which predicts that fracturing of a cavity of a given size in a medium of a given toughness will always occur for undercoolings larger than a critical value, independent of parameters such as the permeability or the elasticity of the medium, which can only affect the timescale. This is discussed further in section 7.4.

As we have seen in chapter 6, the timescale of our model is much smaller than that predicted by Walder & Hallet, of the order of minutes for unfrozen granite. We have seen that the timescale is inversely proportional to the permeability of the medium, which indicates that the large discrepancies between ours and Walder & Hallet's numerical results are due to our different assumptions about the existence of pore ice. The differences between the two models, and how they affect the numerical results, are further discussed in section 7.2.

Murton *et al.* (2006) used Walder & Hallet's model coupled with heat and water transfer equations, given respectively by a thermal energy balance and Darcy's law. The pore ice content features explicitly in the energy balance equation and appears in the effective permeability with some free parameters determined by experimental measurements. Unlike Walder & Hallet, the sub-critical growth in this case was modelled by $V \sim e^{K_I/K}$. A year-long experiment was done on freezing of a block of chalk. The bottom was kept at temperatures below 0° C, simulating permafrost, while the upper half cycled above and below 0° C, simulating seasonal temperature variations. Numerical results are presented for crack length, solid pressure variations and depth at which fractures occurred, and the latter is compared to experimental data. The undercoolings are relatively small, which implies slow fracturing, and melting of the ice inside cracks can occur during the thaw cycles. Their numerical predictions for the depth at which cracks appear agree with their experimental findings when an initial distribution of 5 mm cracks is assumed. As noted in the paper, the choice of initial crack radius has a negligible effect on the long-time fracturing rate, which agrees with our findings in section 6.6.3. Despite this, we would expect it to have an important role in determining the depth at which the fractures appear, as the temperature field varies through the depth of the rock, with the colder region being at the bottom. As we will see in section 7.4.2, the undercooling required for a cavity to fracture is inversely proportional to the square root of the initial radius of the cavity. This

implies that a distribution of smaller cracks would result in the bigger fractures appearing towards the colder regions of the rock, i.e. towards the bottom. Moreover, the interaction of the cracks could have an important effect on the water content and availability, as several cracks were found in the experiment, in many cases located quite close together.

7.2 Rock fracturing

While in previous chapters we have discussed the propagation of a cavity in dimensionless terms and looked at the quantitative effect of the parameters, here we apply our model to specific examples of rocks. Table 7.1 lists the values for the physical constants relevant to water and ice, which are used for all the examples we consider. We also look at values of the fracture toughness K, the shear modulus G, Poisson's ratio ν, the porosity ϕ and the permeability Π for different types of rocks and clays, presented in table 7.2.

Parameter	Value
$\mathcal{L}$	334×10^7 cm^2/sec^2
ρ_s	0.92 g/cm^3
k_l	2×10^5 g $\cdot$ cm/ sec^3 $\cdot$ K
μ	1.79×10^{-2} g/ cm $\cdot$ sec
T_m	273 K
γ	33 g/ sec^2

Table 7.1: *The physical constants relevant to water and ice. Data from SnowCrystals.com (2011)*

Rock type	K(MPa $\cdot$ m$^{1/2}$)	G(GPa)	ν	ϕ	Π(cm^2)
Granite	1.74	40	0.2	0.01	10^{-15}
Limestone	0.7	13	0.2	0.2	10^{-13}
Clay	$2.75 \cdot 10^{-3}$	$3.85 \cdot 10^{-3}$	0.3	0.5	10^{-13}

Table 7.2: *The main rock properties used in the problem for different types of rock and clays. Data from Walder & Hallet (1985), Murton* et al. *(2006), Katz* et al. *(2000), Al-Shayea (2004), Schmidt (1976) and Konrad & Ayad (1997).*

Table 7.3 shows how the dimensionless parameters of the problem depend on the undercooling, the rock properties and the initial radius of the cavity. The values given for the permeability of the different media so far assume that there is no pore ice, or that its effect on the flow of water through the medium is negligible. An expression for an undercooling-dependent permeability is given in section 7.6.

Parameter*	Granite	Limestone	Clay
$\tilde{\Pi} = 10^{13}\Pi$	0.01	1	1
$\tilde{H} = 17R_0^{1/2}\Delta T/m^{1/2}$	$2.4R_0^{1/2}\Delta T$	$4.2R_0^{1/2}\Delta T$	$229R_0^{1/2}\Delta T$
$\tilde{K} = 155m^{1/2}K/E$	19.9	14	3.1

Table 7.3: *Expressions for the three dimensionless parameters of the problem in terms of the physical parameters and their values for different rock and clays. * Values of the rock properties are given in the units mentioned in table 7.2 while the undercooling ΔT is in K and the initial radius R_0 in cm.*

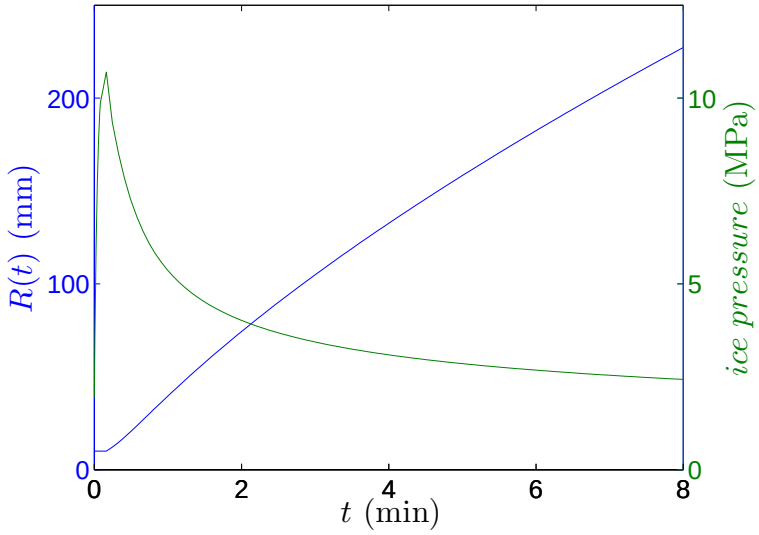

Figure 7.1: *A plot of the length $R(t)$ and average ice pressure against time for a limestone subjected to an undercooling of $\Delta T = 10\,\mathrm{K}$.*

We show the evolution of the radius of the cavity and the average pressure distribution with time for a representative example of a limestone-like rock in figure 7.1. The thickness of the cavity is shown in figure 7.2. We observe that the propagation is very fast, of the order of cm per minute. The solid pressure is plotted on the same figure as the growth of the cavity, and we can see that

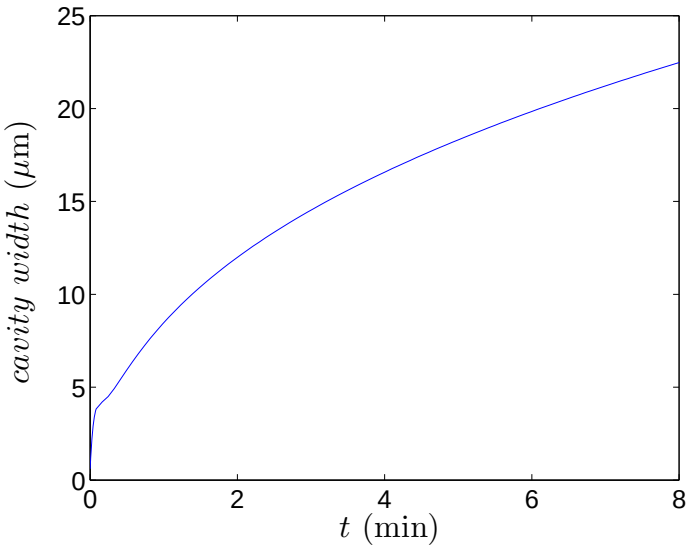

Figure 7.2: *A plot of the maximum thickness of the cavity against time for a limestone subjected to an undercooling of* $\Delta T = 10\,\mathrm{K}$.

the peak in pressure occurs at the point where the propagation begins. This is at the end of the pressure build-up phase, and the pressure drops as the crack extends since the stress at the tip needs to remain constant. The thickness of the cavity increases with time, although the most rapid increase is during the initial build-up phase where considerable amount of ice formation is required for the stress at the tip to reach the critical value. Since the radius is constant during that initial phase, the aspect ratio increases. As the cavity propagates, it becomes more slender, hence we expect the peak of the aspect ratio to coincide with the peak in the solid pressure.

7.3 Time scales

As we saw in section 6.2, the balance of the liquid and solid pressures determines the time scale of the system, given by equation (6.10). The timescale t^* is inversely proportional to the permeability of the medium, as the latter controls the flow of water through the pores. It is also inversely proportional to the elastic modulus of the rock, which affects the deformation caused by a given solid

pressure distribution. With the permeability Π having units of cm^2, the elastic modulus m in terms of GPa and the initial cavity radius R_0 in cm, we find

$$t^* = \frac{R_0^2}{\Pi m} 10^{-12} \mathrm{sec}. \tag{7.1}$$

The following table shows the time scale for different rocks, for initial radius of $R_0 = 1\,\mathrm{cm}$.

Time scale	Granite	Limestone	Clay
t^*	20 sec	0.6 sec	30 min

Table 7.4: *Values of the time scale for different rocks and clays. An initial radius of* $R_0 = 1\,\mathrm{cm}$ *has been used.*

Both the values for the time scale of the problem as well as the results shown in figure 7.1 indicate that the growth rates we find are much larger than the ones predicted by Walder & Hallet (1985). While we find significant growth in minutes or even seconds, the Walder & Hallet model predicts growth which takes tens of hours. We are therefore interested in investigating the differences between the two models and understanding where these time-scale discrepancies come from.

One important difference when it comes to comparing numerical results is that, as discussed in the beginning of this chapter, the Walder & Hallet model considers subcritical growth of cracks, which occurs for values of the stress lower than the fracture toughness K but above the "stress-corrosion limit" $K_{\text{s-c}}$. This is typically a fraction of the fracture toughness K, estimated at $K_{\text{s-c}} \approx 0.3K - 0.4K$. The main effect of this is that fracturing will be predicted for smaller undercoolings than the ones required by our theory. While this will not affect the time scale of propagation as much as the permeability and pore ice effect, it is still important to take it into account, since it strongly affects the potential of a pre-existing rock to fracture at a given undercooling (see section 6.6.1). The subcritical growth is described by an exponential law based on data from load-fracturing experiments. As discussed at the beginning of this chapter, our critical propagation rule comes from the balance of the pressures p_s, p_l and p_T and the linear elasticity theory and hence should be applicable to a larger range of material.

Furthermore, Walder & Hallet apply their model to relatively impermeable rocks and include the effect of a frozen fringe. It is important to point out here that since they are considering a frozen fringe, the effective permeability of the medium is significantly smaller than it would be in the absence of pore ice. The contribution to the "flow resistance" R_f from the frozen fringe alone makes for a rather large flow resistance, with the effective permeability at just 1°C of undercooling being of the order of 10^{-16}cm^2 (value derived from their data for the hydraulic conductivity of the medium), and inversely proportional to the squared power of the undercooling.

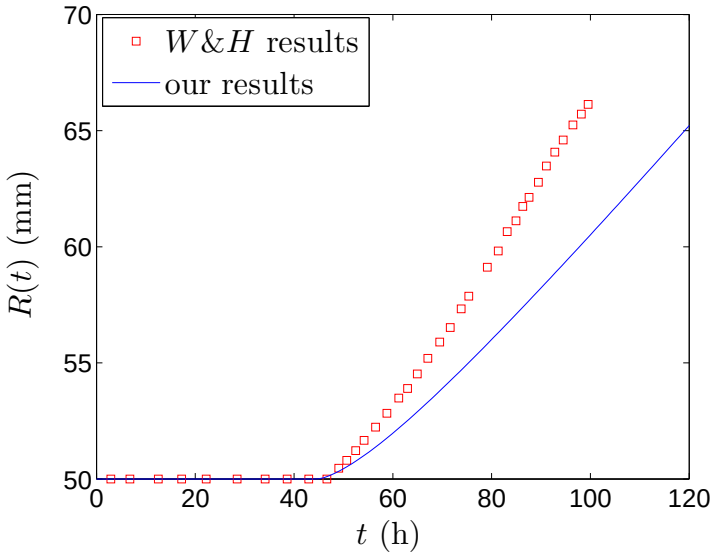

Figure 7.3: *Crack growth vs. time for a cavity of initial radius* $R_0 = 50\,\text{mm}$ *in granite, with undercooling of* $6\,^\circ C$*. The red squares represent numerical results from Walder & Hallet.*

With these differences taken into account, we can attempt a direct comparison of their numerical results with our theory. With the adjusted values for effective permeability due to pore ice, we find propagation rates much closer to those predicted by Walder & Hallet. Figures 7.3 and 7.4 show the evolution of the radius $R(t)$ and solid pressure p_s with time. We see that the agreement of the initial time it takes for the propagation to begin is good, and the peaks in the solid pressure are also in agreement. During the propagating phase, the Walder & Hallet model predicts slightly faster growth than ours. The difference in the pressure curves is consistent with the growth curves, as faster propagation means

faster drop in the pressure as the crack extends. This can be explained by an inherent difference in the two models: linear elasticity predicts stable propagation only in the critical state $K_I = K$. As we have modified the fracture toughness to agree with the Walder & Hallet model, this corresponds to $K_I = 0.3\,K$ here. The key point is that the critical stress at the tip remains constant throughout the fracturing process in our model. In contrast, the power law used by Walder & Hallet predicts propagation for $K_I > 0.3\,K$, hence the stress at the tip can take values larger than the stress-corrosion limit $K_{s-c} = 0.3\,K$. Indeed, the authors point out that the value of K_I continues to increase slightly after propagation has started. A larger stress K_I causes faster growth rate V, as described by the exponential growth law $V \sim e^{K_I^2/K^2}$.

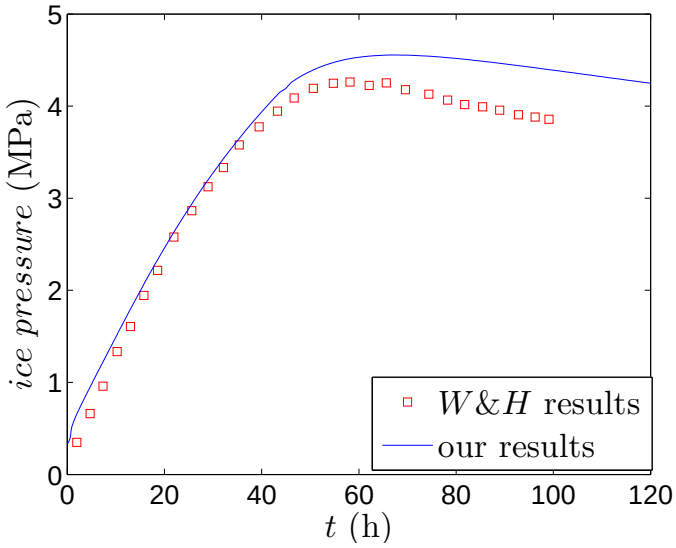

Figure 7.4: *Elastic pressure vs. time for a cavity of initial radius* $R_0 = 50\,\text{mm}$ *in granite, with undercooling of 6 °C. The red squares represent numerical results from Walder & Hallet.*

The question is, what is the effect of these very low "effective permeabilities" and how realistic are they? It has long been assumed that frozen fringes exist in freezing rocks and soils, and many theories developed for the prediction of ice lenses in particular require their existence (see O'Neill & Miller, 1985; Fowler, 1989; Rempel *et al.*, 2004). In contrast, there is evidence of ice lens growth in soils in the absence of a frozen fringe (Watanabe & Mizoguchi, 2000). Several

factors (curvature melting, premelting etc.) contribute towards the lowering of the freezing temperature inside small pores, so all of them have to be taken into account when predicting the existence of pore ice. While it is relatively easy to predict if ice can exist in a pore of a certain size (see appendix E), it is less straightforward to quantify the effect that the pore ice has on the overall permeability of the medium. This is discussed in more details in section 7.6. Our model shows that a frozen fringe is not necessary for frost fracturing. It also allows us to consider whether the existence of pore ice can lower the effective permeability enough to make expansion effects important, as was seen in chapter 3. At the end of section 3.2 it was shown that the expansion effect becomes important when

$$x \sim 10^{15} \Pi \, \mathrm{cm}^{-2}, \tag{7.2}$$

i.e. for large radii ($x \approx 1$) and small permeabilities ($\Pi < 10^{-15} \, \mathrm{cm}^2$). For a penny-shaped cavity, it is more complicated to quantify the expansion regime pressure, as the growth of the ice will be asymmetric. We can estimate though that the worst case scenario will again occur when $x \approx 1$, which corresponds to the case where a large part of the pre-existing fault is occupied with ice which is growing, but no considerable deformation of the cavity has occurred yet. The values of permeability for which the expansion can produce large pressures are not unreasonable for some of the frozen granites Walder & Hallet are considering. Even though this phenomenon is sensitive to the saturation of the medium as well as the exact process of ice growth at the early stages of solidification, we expect that in some cases, high pressures can develop not only during the premelting stage, where the pre-existing faults are ice-filled, but also during the initial stage of freezing.

Finally, it is important to note that, despite the two different sets of results not completely overlapping, our method can reproduce the qualitative features of the Walder & Hallet model, when we adjust the permeability and fracture toughness so that they reflect some of their assumptions. We note that the initially slow and then rapidly accelerating fracturing can be seen in both models. As discussed at the beginning of this chapter, the empirical law used by Walder & Hallet is not the only one that can be used to describe subcritical fracturing. Most laboratory experiments provide data of a small range, making it impossible to distinguish between the different laws discussed at the beginning of section 7.1.

When it comes to extrapolating to geophysical conditions though, the predictions of the different laws diverge considerably (Atkinson, 1984). Moreover, there is limited experimental evidence of subcritical fracturing in rocks. While our model describes critical rather than subcritical growth, it does not rely on empirical observations, hence it can potentially describe a greater range of situations arising in nature.

7.4 Frost-proof material

The theoretical model we have developed can be used to determine what properties a material should have to be able to withstand a certain amount of freezing. The timescale of the pressure build-up and fracturing is also important, as a material that requires hours or days to fracture would effectively be frost-proof in places where temperatures vary significantly below and above zero during the day-night cycle. The model of a rock cooled from the outside, with the temperature on its boundary uniform, can successfully describe many real-life situations, where the materials are exposed to the sub-zero atmosphere from all sides. While the crack model is of course idealized, the assumption of a flat, thin crack is a sensible one.

When the temperature of the far-field does not vary with time, the maximum solid pressure attainable is equal to the maximum disjoining pressure possible, which can be expressed in terms of the undercooling

$$p_{\max} = \frac{\rho_s \mathcal{L} \Delta T}{T_m}. \tag{7.3}$$

This indicates that only the undercooling of the environment and the fracture toughness of the medium, which represents how much pressure it can withstand, will determine whether a cavity of a given size will fracture. This might appear to be contradicting the analysis done in section 5.3.4, which found that the permeability of the medium affects the boundary between propagating and non-propagating solutions. In a warming environment though, the time scale of water transport is important for the pressure build up: water needs to flow to

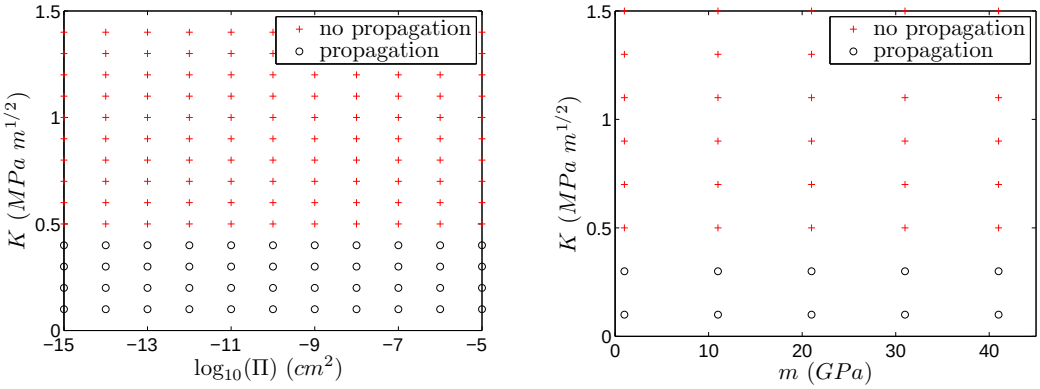

Figure 7.5: *(a) A phase plane showing propagating and non-propagating solutions for different values of the fracture toughness $\tilde{K}$ and of the permeability Π at undercooling $\Delta T = 5\,\mathrm{K}$, showing that the transition is independent of Π. (b) A similar phase plane showing the effect of the elastic modulus m vs. the fracture toughness K.*

the solidification front quickly as the longer it takes, the warmer the surrounding environment will be, resulting in a lower value of $p_{\max}$. Indeed, this agrees with equation (5.47) which shows that the permeability affects the fracturing of the medium only when it is small enough to limit the flow of water towards the solidification front. Therefore, we expect that when the undercooling of the surrounding environment does not vary with time, and therefore $p_{\max}$ is constant, the permeability of the medium will not affect the boundary between no propagation and fracturing. A phase plane for $\Delta T = 5$ (figure 7.5, left) of the fracture toughness K against the permeability Π, spanning 10 orders of magnitude of Π, does indeed show that the potential for fracturing for a given value of undercooling does not depend on how permeable the medium is. The graph on the right of figure 7.5 shows that the transition regime is also independent of the elastic modulus.

In both graphs, we see that there is a critical value of the fracture toughness K for the given undercooling ΔT above which the rock does not fracture. A similar argument to the one used to derive expression (6.34) gives us that, for a given ΔT and initial radius R_0, the maximum fracture toughness K for propagation to occur is

$$K_{\max} = \frac{2}{\sqrt{\pi}} R_0^{1/2} \frac{\rho_s \mathcal{L} \Delta T}{T_m}, \tag{7.4}$$

which is, as expected, independent of both Π and m. This theoretical prediction

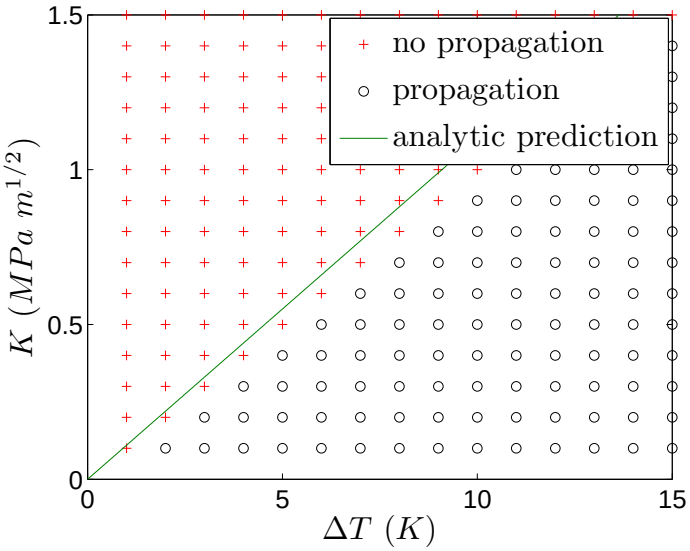

Figure 7.6: *A phase plane showing propagating and non-propagating solutions for different values of the fracture toughness $\tilde{K}$ and of the undercooling ΔT. The green line shows the theoretical prediction defined by equation* (7.4).

can be seen in figure 7.6, where we have plotted the slope between K and ΔT (green line). We see that the match is not perfect, which is a result of the cavity not being completely ice-filled, as was explained in section 5.3.2. The quantitative effect of $\lambda < 1$ on the above expression is described by equation (6.35).

From the above we can conclude that the most important parameters for the susceptibility of a medium to fracturing are the fracture toughness of the material and the undercooling of the environment. The size of the pre-existing faults also strongly influences the fracturing potential, as indicated by equation (7.4). We will discuss this further in section 7.4.2. We also found that the permeability and elasticity of the medium do not affect the potential for fracturing in the idealized situation of constant undercooling but have an important effect on the timescale of propagation, as we will see in section 7.5. In real situations, the temperature of the far field can vary significantly with time. As we saw in chapter 5, both the permeability and the elasticity of the material affect the potential for fracturing in a warming environment. In these cases, the timescale of pressure build-up becomes important when discussing the susceptibility of a material, as the conditions change with time.

7.4.1 Effect of porosity

When we derived the equations describing the flow of water through the medium and inside the crack in section 4.1.3, we ignored the porosity of the medium and approximated the volume outside the cavity as consisting of only rock when using mass conservation arguments. Considering the flow of water into the porous medium, we only included the component of the Darcy flow u as the contribution to the flux at the film–rock boundary $z = b$. In reality, a proportion ϕ of the rock is already occupied with water and hence, as the rock boundary deforms with velocity $\frac{\partial b}{\partial t}$, an additional term of $-\phi\frac{\partial b}{\partial t}$ needs to be included in the contribution of the flux at $z = b$. This indicates that in the frame of reference of the thin film, there is a component of the flow *out of* the cavity, acting in an opposing way to the Darcy flow. This makes sense physically; the term u expresses the flux of the water that flows towards the cavity to fill the opening gap which is created because areas previously occupied by rock need to be filled by water. In the limit of $\phi \to 1$, i.e. if the rock is very porous and consists mostly of water, the effect of the opening of the cavity is negligible, as very little space is occupied by the rock. In the opposite limit of $\phi \to 0$, we assume most of the cavity boundary is occupied by rock, which when it opens up frees the space to be filled by water. This limiting case represents the assumption we made when ignoring the porosity. The mass continuity equation in the thin film now gives

$$(1-\phi)\frac{\partial b}{\partial t} + \frac{1}{r}\frac{\partial}{\partial r}\left(r\frac{h^3}{12\mu}\frac{\partial p_l}{\partial r}\right) = -u(b) = \frac{\Pi}{\mu}\frac{\partial p}{\partial z}\Big|_{z=b}. \tag{7.5}$$

The factor $(1-\phi)$ now multiplies the liquid pressure integral, giving

$$p_l(r,t) = \frac{2}{\pi}\frac{\mu}{\Pi}(1-\phi)\int_0^{R(t)} K\left(\frac{2\sqrt{rs}}{r+s}\right)\frac{\partial b}{\partial t}\frac{s\,ds}{s+r} \quad \text{if } r \le \lambda R, \tag{7.6}$$

hence it can be absorbed in Π to give a new permeability

$$\Pi_\phi = \frac{\Pi}{1-\phi}. \tag{7.7}$$

As we have seen, a change in the permeability of the medium does not affect the fracturing potential of a cavity but just the timescale of the pressure build-up and subsequent fracturing. Similarly, the effect of the porosity is simply limited

to the timescales of the problem. A large porosity ϕ implies a larger value of the "effective permeability" Π_ϕ and hence easier flow of water through the medium and faster solidification and crack propagation. We see that the effect is quite small, unless we have a very porous medium with large ϕ, which increases the effective permeability.

For most materials we are concerned with, the porosity is small enough ($\phi < 0.3$ for rocks and $\phi < 0.5$ for clays) for its effect on the time scale to be quite unimportant. As McGreevy (1981) points out, experiments (Wiman, 1963; Potts, 1970; Keeble, 1971) have failed to provide evidence of a correlation between porosity and amounts of weathering, which is supported by our analysis.

7.4.2 Effect of initial crack radius

In section 6.6.3 we discussed how the initial radius of the crack affects the propagation. Two important points were found: firstly, two fracturing cracks that are of the same size at a given time t will propagate in identical ways even if they originated from different-sized initial faults. That is to say, the rate of propagation is only dependent on the radius of the cavity at that point in time rather than the initial size. Secondly, for a given medium and value of undercooling ΔT, pre-existing faults need to be larger than a minimum initial radius $R_{\min}$ to start propagating.

Figure 7.7 shows the propagating (black circles) and non-propagating (red crosses) solutions for different values of the initial radius R_0 and the undercooling ΔT. As we saw in section 6.6.3, there is a lower bound $R_{\min}$ for the initial radius of the cavity R_0 for fracturing to occur. This is not an exact minimum as it assumes that the cavity is completely ice-filled. This lower bound is given in terms of the fracture toughness of the rock and the undercooling of the medium

$$R_{\min} = \frac{\pi K^2 T_m^2}{4\rho_s^2 \mathcal{L}^2} \Delta T^{-2}. \tag{7.8}$$

For the example shown in figure 7.7, we have taken $K = 1\,\mathrm{MPa} \cdot \mathrm{m}^{1/2}$, and plotted the relation between ΔT and $R_{\min}$ that the criterion above defines (blue curve). As expected, the $R_{\min}$ curve doesn't quite match the boundary between

the propagating and non-propagating solutions, but slightly underestimates the undercooling required for fracturing. This agrees with our conclusion that $R_{\min}$ is only a lower bound. Furthermore, the boundary between propagation and non-propagation agrees with the prediction that $\Delta T^2 R_0 =$ constant and we can deduce that the slight difference in the constant is due to the λ correction for a cavity that isn't completely ice-filled (see also equation (6.35)).

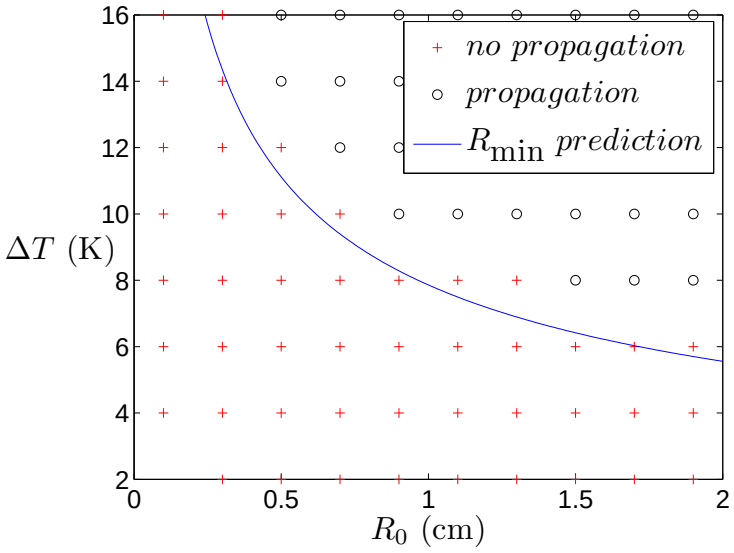

Figure 7.7: *A phase plane showing propagating and non-propagating solutions for different values of the undercooling ΔT and the initial radius R_0 for a limestone-like rock.*

The concept of the minimum size of a fault for fracturing was also described by Murton *et al.* (2006), who also find the minimum radius for fracturing to be related to the inverse square power of the undercooling, as in equation (7.8). Although an analytic expression is not given and hence we cannot compare it with ours directly, they mention that their theory predicts no fracturing for cavities of length smaller than 0.15mm at undercooling of -5 degrees. Their calculations were done for a limestone with fracture toughness $K = 0.2\,\mathrm{MPa}\cdot\mathrm{m}^{1/2}$. Using equation (6.34) we find that the minimum crack radius for propagation is $R_{\min} \approx 0.9\,\mathrm{mm}$, which is quite a bit larger than their prediction. Referring back to the Murton *et al.* (2006) model, we note that they use the same propagation criterion as Walder & Hallet (1985), predicting propagation for $K_I \geq K_{s-c}$, where K_{s-c} is the "stress-corrosion limit". Substituting the fracture toughness for $K_{s-c} = 0.3\,K$ in expression (6.34),

we find the minimum length of the initial crack to be $2R_0 \approx 0.16\,\mathrm{mm}$, in good agreement with the prediction of Murton *et al.*.

As expected, we have found that media with smaller pre-existing faults are less prone to fracturing as they can withstand the higher pressures caused by larger undercoolings ΔT. Furthermore, the criterion for the minimum radius for propagation that is developed here is in agreement with other theoretical models and, as we will see in section 7.7, with experimental observations too.

7.5 Timescale of pressure build-up

As we saw in the previous section, there are some parameters of the problem which do not determine whether a fault of a given initial size will fracture, but do affect the growth rate once the fracturing begins. The permeability of the medium controls the flow through the pores towards the solidification front and we saw in section 6.6.2 that it strongly influences the timescale of pressure build-up and growth, especially for impermeable media. It is also interesting to note that for a large enough permeability (larger than about $10^{-12}\,\mathrm{cm}^2$), the effect becomes negligible.

The elasticity of the medium is also important in determining the timescale of propagation. Figure 7.8 shows plots of the growth of the cavity $R(t)$ against time for different values of the shear modulus G. We see that the growth rate rapidly increases with G. A large elasticity modulus means that a given amount of pressure causes only a small amount of deformation. Two cavities of the same length in two media with different values of G will have different thicknesses when they are at the critical state $K_I = K$. Since the stress required for fracturing is the same in every case, as it is determined by the fracture toughness K, the pressure is equal and hence the cavity with the smaller G will have deformed more. The pressure that the ice exerts on the rock is relaxed by the rock deformation hence the more compliant the medium is, the longer it takes for the pressure to reach the critical value. This demonstrates that a very compliant medium fractures more slowly than a stiff one, even if the fracture toughness is the same, as can be seen in figure 7.8.

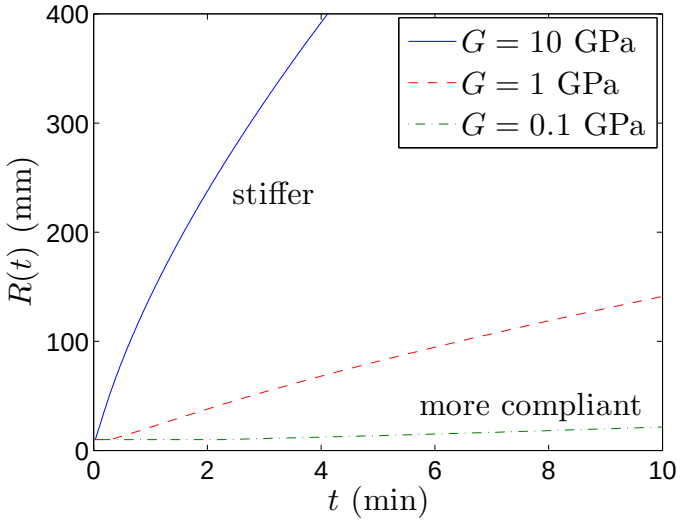

Figure 7.8: *The growth of the cavity $R(t)$ against time for different values of the elastic modulus G of the rock.*

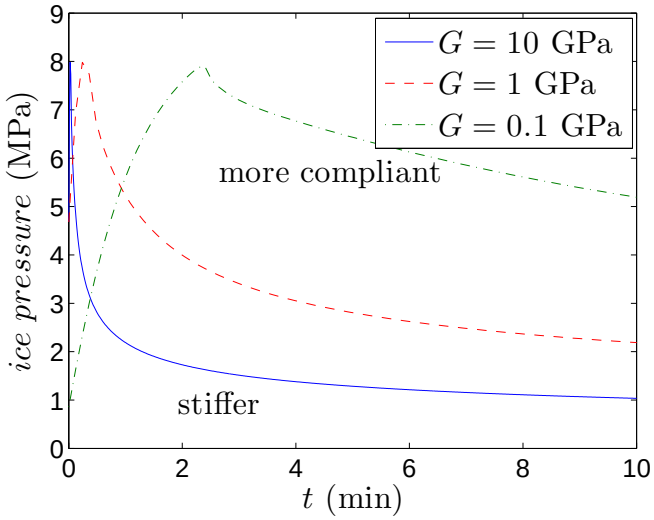

Figure 7.9: *Plots of the solid pressure against time for different values of the elastic modulus G of the rock.*

Figures 7.9 and 7.10 show how the solid pressure and the width of the cavity develop with time for the three different values of the shear modulus presented in figure 7.8. We note that the peak in the solid pressure is the same in all three cases, $p_s \approx 8\,\text{MPa}$. This is expected, as the peak occurs at the exact moment that

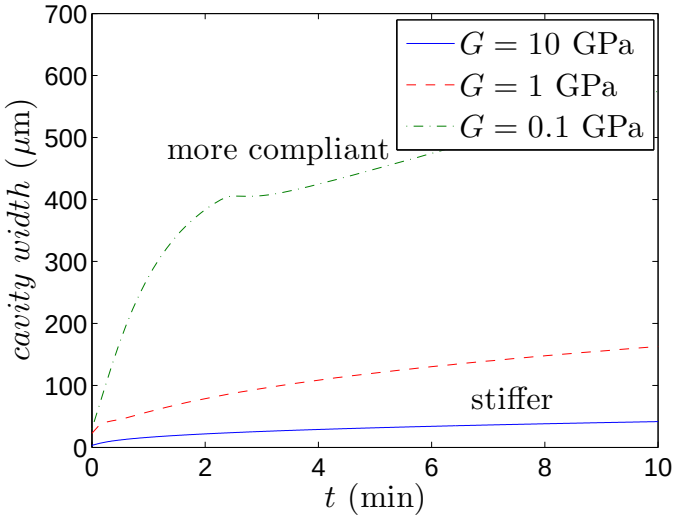

Figure 7.10: *Plots of the width of the cavity against time for different values of the elastic modulus G of the rock.*

the critical stress at the tip is reached and just before the fracturing begins. Since both the fracture toughness and the radius of the cavity (equal to the initial radius at that stage) are the same, we expect the maximum of p_s to be the same in all three cases. The pressure takes longer to build up to the maximum value and then drops away slowly in the compliant medium ($G = 0.1\,\text{Gpa}$). This is in agreement with the fact that the slowest growth occurs in the most compliant medium. As we have explained before, for a medium of a given fracture toughness, a larger cavity will require smaller pressure to propagate in the critical state $K_I = K$.

It is also clear that in the compliant medium, the thickness of the cavity is much larger than the one in the stiff medium. This is due to a combination of two factors: firstly, the pressure applied on the rock at a given time is larger in the compliant medium, owing to the smaller size of the cavity. Secondly, the deformation due to a given p_s is larger than it would be in a stiff medium.

Finally, we examine the behaviour of the crack during the pressure build-up phase. We define the time it takes for the stress to reach the critical value as t_{initial} and we plot its dependence on the shear modulus G in figure 7.11. The red curve behaves like G^{-1} and we can see that the agreement with the numerical

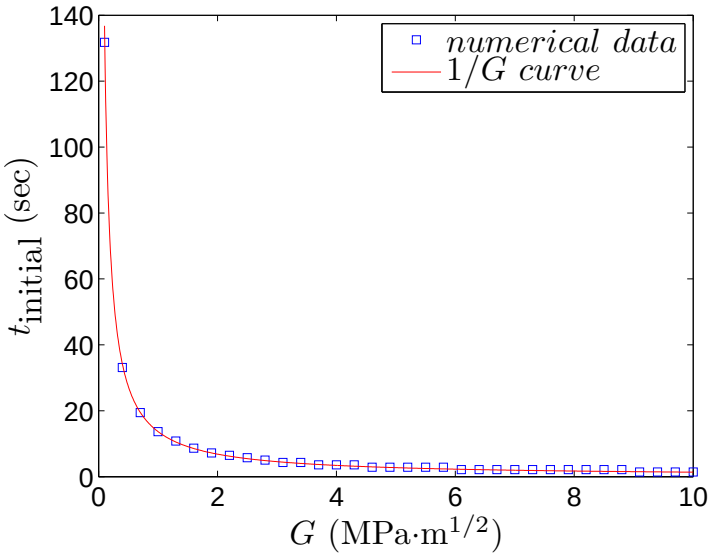

Figure 7.11: *Plot of the time it takes for the pressure to reach the critical value against the elastic modulus G of the rock. The red curve is $\sim G^{-1}$.*

results shown by the blue squares is excellent. This demonstrates that

$$t_{\text{initial}} \sim \frac{1}{G}, \tag{7.9}$$

a result also found by Walder & Hallet (1985). We also expect the time scale of the fracturing to have a similar dependence on the elasticity, which would be in qualitative agreement with figure 7.8. This can become important in the case of very compliant materials, when the value of m can be several orders of magnitude smaller than in rocks. In those cases, the predicted pressure build up can take up to hours, even without considering a frozen fringe and the resulting low permeability. For real materials, a small value of the elastic modulus is usually accompanied by a fracture toughness a few orders of magnitude smaller than in rocks. This means that fracturing can occur at much lower undercoolings. Clays are typical examples of materials with such properties and the application of our theory to them will be discussed in section 7.7.

7.6 Frozen fringe

The theory developed in this thesis predicts fracturing of pre-existing faults in rocks without the need for a frozen fringe. Previous studies of rock fracturing (Walder & Hallet, 1985; Murton *et al.*, 2006) have assumed the existence of pore ice, while studies of frost heave (Rempel *et al.*, 2004) predict no ice lens formation in the absence of a frozen fringe. Physically, when a water-saturated porous medium is subjected to sub-zero temperatures, water inside the bigger pores can freeze, restricting the hydraulic connectivity of the medium. The extent of the freezing depends on the freezing-point depression, which is a result of curvature melting or the disjoining forces between rock and ice. Quantifying this effect is difficult, as pore size varies from material to material, and there can be a large range of pore diameters within one material too. For example, while most limestones have pore sizes of the order of $0.1-1\,\mu$m, marbles and lithographic limestones can have an average pore size of about $0.005\,\mu$m (Lautridou & Ozouf, 1982). The critical nucleation radius for an undercooling of $\Delta T = 1\,\mathrm{K}$ is approximately $0.1\,\mu$m and, while inversely proportional to ΔT, we see that even for low temperatures, curvature melting can stop ice from growing inside porous material. While we have assumed no pore ice, it is a concept that is easily incorporated into our model. The existence of ice in the pores of a medium primarily affects the permeability and limits the flow of water towards the solidification front. We expect the change in permeability to have an effect on the time scale of pressure build-up and propagation, but not on the fracturing potential of a fault (see sections 6.6.2 and 7.4).

Both Walder & Hallet (1985) and Murton *et al.* (2006) consider the effect of pore ice on the permeability of the medium. The former use a modified hydraulic conductivity for the medium of the form $k = \kappa_1 \Delta T^{-2}$, where the parameter κ_1 is found from experimental data. The value of κ_1 used in their work corresponds to a permeability of $\Pi = 10^{-16}\,\mathrm{cm}^2$ at an undercooling of $1^\circ\,\mathrm{C}$ for a granite. In contrast, Murton *et al.* include an 'ice content' term in the heat equation which is then used to determine the permeability which behaves like $\Pi \sim (1-I)^\gamma$, where I is the volumetric ice fraction and γ is determined experimentally and usually ranges between 6 and 9.

The permeability is closely related to the size of the pores, and can be shown (Bear, 1988) to be proportional to the square of the average pore diameter

$$\Pi = Cd^2, \tag{7.10}$$

where C is a constant relating to the flow paths connecting the pores. If we consider the growth of ice in a small spherical pore, two effects contribute to the depression of the freezing temperature: the curvature-induced melting, and the disjoining forces which become important when the pore is almost ice-filled, as explained in chapter 3. It can be shown that, at first order, the smallest depression of the freezing temperature is determined by the curvature melting effect (i.e. dictated by the Gibbs–Thompson relation). In that case, the ice is close enough to the rock for the curvature to be approximately given by $\kappa = 1/d$, where d is the diameter of the pore, but not close enough for the disjoining forces to become important, hence causing further depression of the melting temperature. The details of the calculation are shown in appendix E.

For a given undercooling ΔT, pores that are larger than the corresponding $d_{\Delta T}$ diameter

$$d_{\Delta T} = \frac{\gamma T_m}{\rho_s \mathcal{L} \Delta T} \tag{7.11}$$

will be almost completely ice-filled, reducing the overall average pore diameter of the medium to $\tilde{d} < d$. We expect this new average diameter $\tilde{d}$ to be a function of both the initial average pore diameter d as well as the freezing pore diameter $d_{\Delta T}$. When $\Delta T = 0$, hence $d_{\Delta T} \to \infty$, no ice grows inside the pores and therefore the average diameter remains unchanged, $\tilde{d} = d$. As the temperature drops, $d_{\Delta T}$ becomes smaller and hence some of the pores can fill with ice. This reduces the overall average pore size. This analysis implies a relationship between $\tilde{d}$, d and $d_{\Delta T}$ of the form

$$\frac{1}{\tilde{d}} = \sqrt{\frac{1}{d^2} + \frac{\alpha}{d_{\Delta T}^2}}, \tag{7.12}$$

where α is a parameter to be determined and relates to the distribution of pore sizes of the medium. We have used the quadratic average (or root mean square) of $1/d$ and $1/d_{\Delta T}$, rather than the mean, as this includes a measure of the spread of the values. For example, when $d_{\Delta T}$ is large (i.e. ΔT is small) and hence $1/d_{\Delta T}$ is much smaller than $1/d$, the quadratic average means that the effect of $1/d_{\Delta T}$

will be small. This makes sense physically as we expect only a few pores to be large enough for ice to grow inside them at small undercoolings. Therefore, when ΔT is small, we expect the average pore size to remain more or less unchanged, and hence the effective permeability to be very close to the unfrozen value.

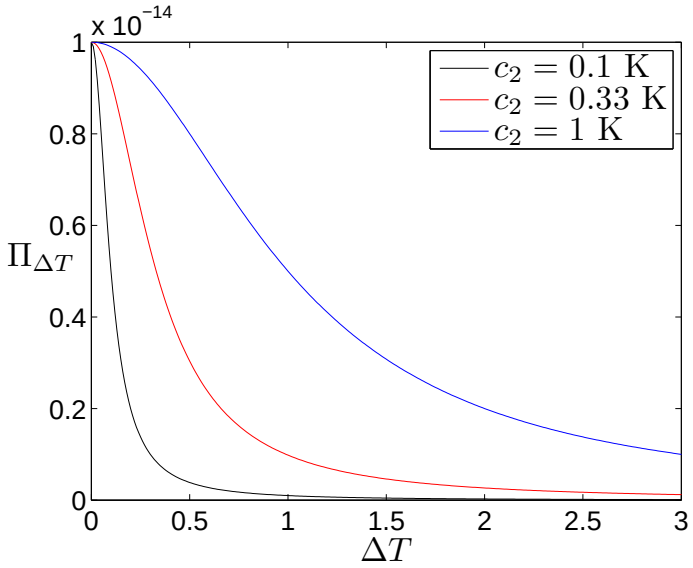

Figure 7.12: *The effect of pore ice on the effective permeability shown through plots of* $\Pi_{\Delta T}$ *vs.* ΔT*, for different values of the parameter* c_2*.*

The effective permeability $\Pi_{\Delta T}$ at an undercooling ΔT will be proportional to $\tilde{d}^2$, according to equation (7.10). We can then express the permeability of the medium $\Pi_{\Delta T}$ in terms of the undercooling ΔT and the unfrozen permeability of the medium

$$\Pi_{\Delta T} = \frac{c_1}{\Delta T^2 + c_2^2}\Pi. \tag{7.13}$$

The parameters c_1 and c_2 have units of K^2 and K respectively, and depend on the medium characteristics, such as the pore size distribution. We note that the frozen permeability is inversely proportional to ΔT^2, as in Walder & Hallet (1985). One of the parameters c_1 and c_2 can be easily fixed by the condition that $\Pi_{\Delta T} = \Pi$ for $\Delta T = 0$, from which we deduce that $c_1 = c_2^2$. To fix the second parameter, we need to determine the effective permeability at a given undercooling. For example, if $c_2 = 0.1\,\mathrm{K}$, an undercooling of just 1 °C will cause a permeability 100 times smaller than the permeability of the unfrozen medium, while $c_2 = 0.33\,\mathrm{K}$

means that, at $\Delta T = 1\,\mathrm{K}$, the permeability is 10 times smaller than the unfrozen value.

Picking an appropriate value for c_2, which is dependent on the properties of the specific medium, requires experimental data. For the following example we consider a granite with unfrozen permeability of $\Pi = 10^{-15}\,\mathrm{cm}^2$. We take $c_2 = 0.33\,\mathrm{K}$, corresponding to an average permeability of $\Pi_{\Delta T} = 10^{-16}\,\mathrm{cm}^2$ at an undercooling of $\Delta T = 1\,\mathrm{K}$, which is in agreement with the values used by Walder & Hallet (1985).

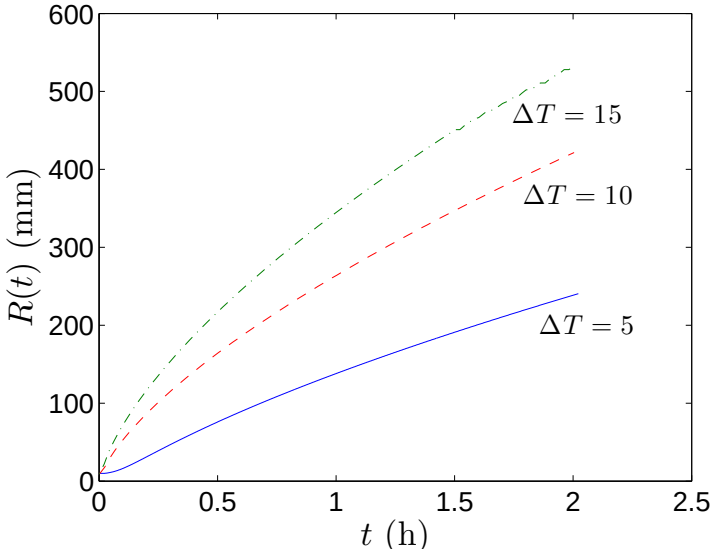

Figure 7.13: *Growth curves of the radius of the cavity $R(t)$ vs. time t for different values of the undercooling ΔT.*

We saw in section 6.6.1 that the growth rate of a crack increases with the undercooling. This can also be seen in figure 7.13 where we have plotted the growth curves $R(t)$ vs. t for three different values of undercooling, $\Delta T = 5\,\mathrm{K}$, $10\,\mathrm{K}$ and $15\,\mathrm{K}$. It is clear that the fracturing is fastest in the coldest environment. However, if we assume the existence of pore ice and approximate the undercooling-dependent permeability of the medium by expression (7.13) then the effect of an increased ΔT will be more complicated. While a large undercooling speeds up fracturing, it also reduces the permeability as equation (7.13) describes. A smaller permeability Π means that flow through the porous medium is more restricted,

hence the propagation slows down. These two effects act in opposing ways and the balance of the two will determine how an increase in ΔT changes the growth curves. An example can be seen in figure 7.14. The overall growth rate is about 100 times smaller than the example shown in figure 7.13, hence the effect of pore ice is significant. Interestingly, we see that the relation between the three curves has changed significantly. Especially at long times, the effect of undercooling is reversed and the faster propagation occurs in the warmest environment, which now has the largest permeability. This effect can also be seen in figure 7.15, where we have plotted the instantaneous (left) and average (right) growth rate of a crack after 2 hours of freezing and 20 hours of freezing respectively. We discover a similar behaviour to that found by Walder & Hallet (1985), with the most effective fracturing occurring at temperatures higher than $-5°\,\mathrm{C}$ and the fracturing rate decreasing for large values of the undercooling, as there is more pore ice restricting the flow of the water. The rates of freezing are of the order of $10^{-4}\,\mathrm{mm/sec}$ which is in agreement with the $10^{-7} - 10^{-8}\,\mathrm{m/sec}$ rates found by Walder & Hallet (1985).

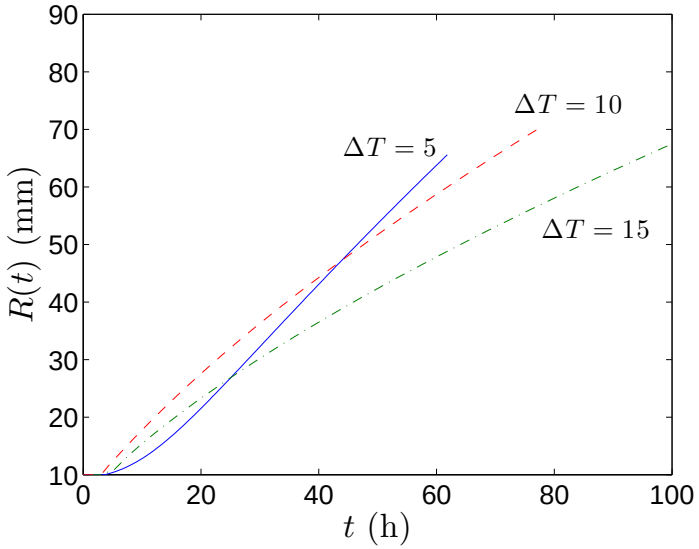

Figure 7.14: *Growth curves of the radius of the cavity $R(t)$ vs. time t for different values of the undercooling ΔT. The permeability of the medium is adjusted to account for the existence of ice pore, according to equation* (7.13)*. We have taken $c_2 = 0.33\,\mathrm{K}$.*

In conclusion, both the existence of a frozen fringe and its exact quantitative effect on the fracturing rate are difficult to determine, since they require detailed

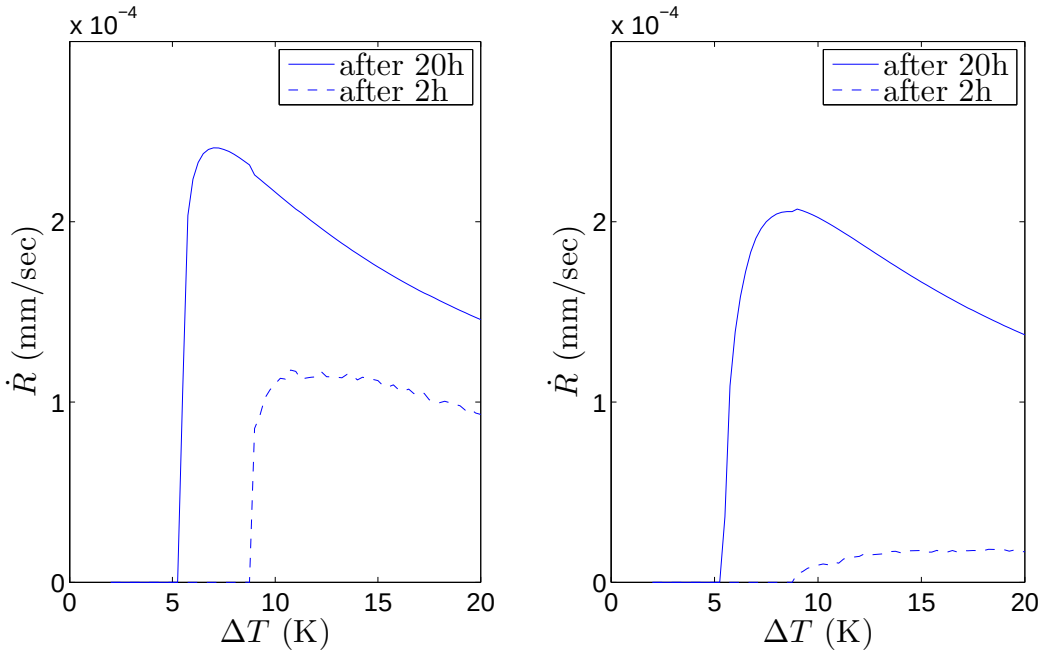

Figure 7.15: *A plot of the instantaneous growth rate $\dot{R}$ (left) and the average growth rate (right) of a cavity in a granite, of initial radius $R_0 = 1\,\mathrm{cm}$ after 2 hours of freezing (dashed curve) and 20 hours of freezing (solid curve). The permeability of the medium is adjusted to account for the existence of ice pore, according to equation* (7.13)*. We have taken $c_2 = 0.33\,\mathrm{K}$.*

data on the pore size distribution of a medium. It should be pointed out that the effect of the permeability through the undercooling is dependent on the value of c_2. We have used $c_2 = 0.33\,\mathrm{K}$ here but a larger value would result in the effect of $\Pi_{\Delta T}$ being weaker and we could see the propagation rate increasing with ΔT even with the decreasing permeability. Experimental work could provide further useful insight here, in particular in investigating the existence of pore ice, determining c_2 and validating expression (7.13).

7.7 Fracturing of clays

While the method developed in this thesis has primarily been used to model rock fracturing, its applications are not limited to rocks. It has been shown that the formation of blocks of ice, or ice lenses, in materials such as clays is

the predominant cause of frost heave, as can be seen in the Taber (1929; 1930) experiments. The ice-filled cavities in rocks work in similar ways to these ice lenses in soils. In both cases, the premelting pressure between the ice and the medium has been identified as the force driving the flow of water towards the solidification front, causing further growth of the ice and the displacement of the medium. Most soil studies have assumed that the similarities between frost heave and frost fracturing are limited to the thermodynamics of the problem. Many of these studies, with Rempel *et al.* (2004) one of the most recent ones, assume that the existence of a frozen fringe is necessary for the formation of ice lenses.

Style *et al.* (2011) recently developed a model for ice lens formation in soils which does not require the existence of a frozen fringe. The main ideas of ice lens growth are similar to the ones presented in this thesis: the difference between the solid and liquid pressures inside a pre-existing flaw filled with water are balanced by disjoining forces. The cavity grows when the pressure inside it causes the stress at the tip to reach the critical value K. When the fracture has extended all the way to the edges of the column, this becomes a new ice lens.

The paper by Style *et al.* (2011) represents a change in the approach used when discussing the growth of ice lenses in soils. The cohesion between particles is now seen as a phenomenon which can be described using linear elasticity and fracture mechanics. Arenson *et al.* (2008) and Style *et al.* (2011) have observed crack-like ice segregation in soils, with new ice lenses forming off vertical shrinkage cracks. The growth velocities observed by Style *et al.* are of the order of mm/min, which is of similar order of magnitude as the results seen in figure 7.16 and 7.18. Furthermore, freezing experiments have shown that ice lenses form at smaller undercoolings for materials with smaller tensile strength (Akagawa *et al.*, 2006). In addition to this, Graham & Houlsby (1983) observed linear elastic behaviour in soils. Linear elastic fracture mechanics (LEFM) were also used by Konrad & Ayad (1997) to model vertical tension cracks in clays. All this indicates that saturated soils do indeed exhibit linear elastic behaviour, and hence LEFM is an appropriate way of approximating soil fracturing under stress.

Clays are characterized by small fracture toughnesses and elastic moduli. This means that they require a small amount of stress to fracture. Also, a given amount of pressure will cause a much larger deformation than it would in a rock.

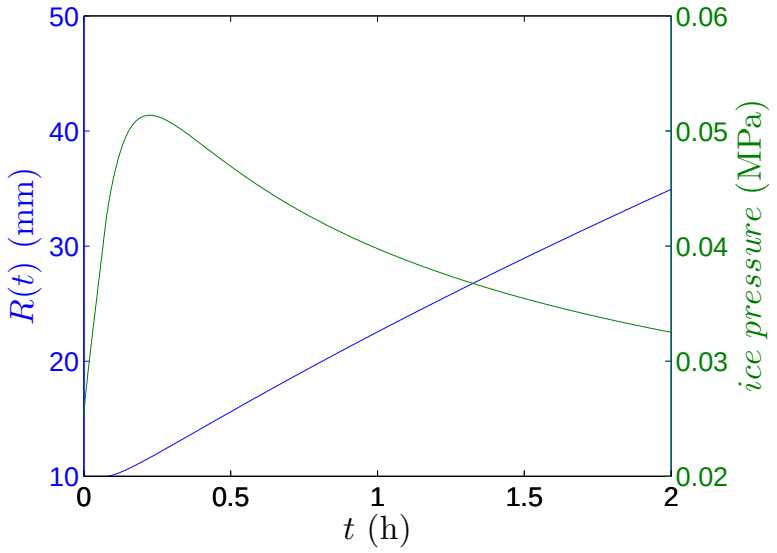

Figure 7.16: *A plot of the growth rate and pressure distribution against time for a clay subjected to an undercooling of* $\Delta T = 0.1\,\mathrm{K}$*, for an initial radius of* $R_0 = 1\,\mathrm{cm}$*.*

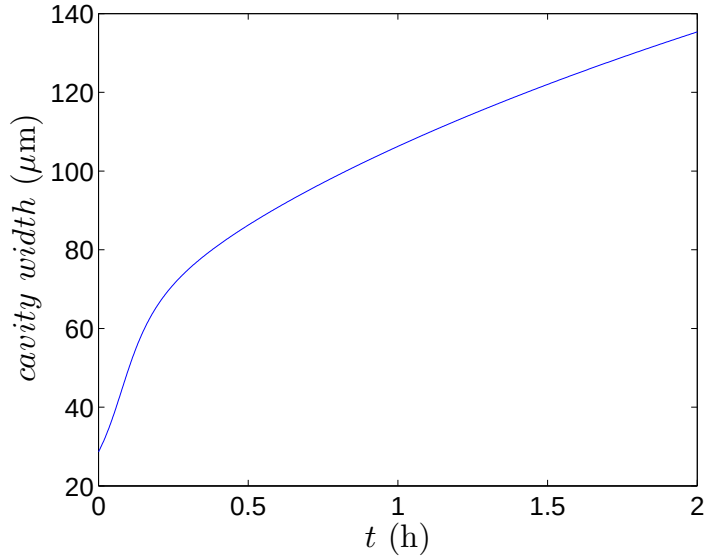

Figure 7.17: *A plot of the maximum thickness of the cavity against time for a clay subjected to an undercooling of* $\Delta T = 0.1\,\mathrm{K}$*, for an initial radius of* $R_0 = 1\,\mathrm{cm}$*.*

Hence, even though the pressures inside a cavity are small when the cavity is propagating, the cavity thickness can still be of the same order as in rocks. We therefore expect similar values of the ice extent λ. Another feature that can be

seen in our results (figure 7.17) is that during the initial $\sim 15\,\text{min}$, the thickness of the cavity increases rapidly, while the freezing slows down after that. This initial "surge" of heave has also been observed experimentally (Penner, 1986).

Owing to the small fracture toughness K, propagation can occur even for small undercoolings. We recall that the transition from non-propagating to propagating cavities is characterized by a linear relationship between K and ΔT. Since K can be more than 100 times smaller in clays than in rocks, we expect fracturing to occur even for undercoolings of tenths of a degree. Figure 7.16 shows the growth rate and pressure distribution with time for a cavity in a clay subjected to $\Delta T = 0.1\,\text{K}$. The propagation is slow, as expected, because of the small value of undercooling and because the medium is much more compliant compared to a rock. The pressure is two orders of magnitude smaller than in rocks, as only a small stress is required at the tip for fracturing. The thickness of the cavity is shown in figure 7.17 and it is interesting to note that it is comparable to cracks in rocks, despite the difference in the pressure applied. This is due to the medium being much more compliant than a rock and therefore deforming considerably even if only a small pressure is applied.

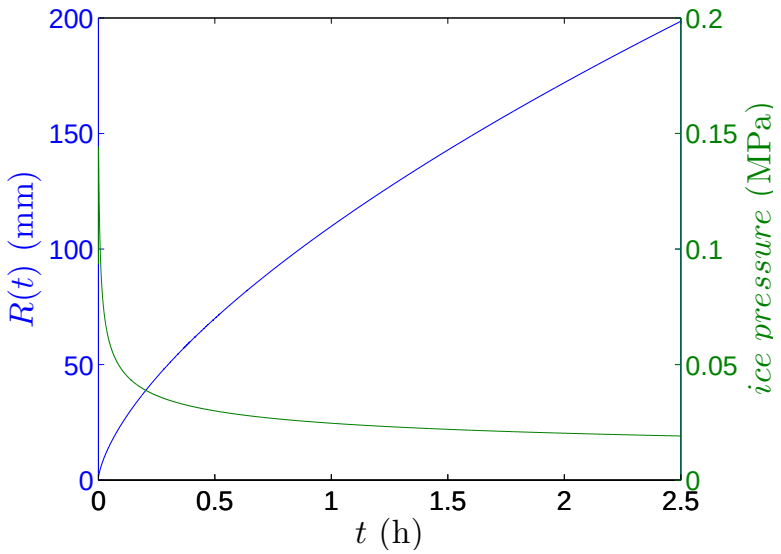

Figure 7.18: *A plot of the growth rate and pressure distribution against time for a clay subjected to an undercooling of* $\Delta T = 1\,\text{K}$*, for an initial radius of* $R_0 = 1\,\text{mm}$*.*

Similarly, equation 7.8 demonstrates that in weak materials (i.e. with a small value of K) even small pre-existing faults can fracture. For example, at $\Delta T = 1\,\text{K}$,

an initial cavity of just $R_0 = 1\,\mathrm{mm}$ propagates rapidly as described in figure 7.18. In this case, the pressures are still small compared to rocks but larger than in figure 7.16. This is possible due to the higher value of undercooling and is necessary for propagation because, although the fracture toughness is the same in the two cases, the area over which the pressure is acting is much smaller in the $R_0 = 1\,\mathrm{mm}$ case.

Watanabe (2002) performed experiments of freezing of a water-saturated powder and found that the growth rate of ice lenses is proportional to the undercooling, a relation that can also be seen in our figure 7.13 which, even though it uses values representative of a rock, can be used to qualitatively describe soils too. This indicates that, for the temperature range used in Watanabe's experiments ($< 1^\circ\,\mathrm{C}$), either no pore ice exists or its effect on the permeability was negligible. Indeed, Watanabe *et al.* (1997) observed the microstructure near the freezing front of an ice lens in a soil and found no pore ice. The heaving rate in the silt, i.e. the rate of the thickness increase of the ice lens, was found to be $1\,\mu\mathrm{m\,sec}^{-1}\,{}^\circ\,\mathrm{C}^{-1}$. As we have found typical aspect ratios of ice lenses in soils to be about 10^{-3}, we deduce that this approximately corresponds to a fracturing rate of $0.1\,\mathrm{mm\,min}^{-1}\,{}^\circ\,\mathrm{C}^{-1}$, which is similar to what our theory predicts. As we mentioned earlier, similar order of magnitude growth rates were observed by Style *et al.* (2011). While there is some uncertainty over the exact values of initial cavity radius and medium permeability used in the experiments, it is important to point out here that these should not affect the agreement with the growth rates much. First of all, we have seen that the growth rate of a crack is not very sensitive to the initial radius (see section 6.6.3). Secondly, the value for the permeability used for the examples shown in figures 7.16-7.18 is representative of a clay and close to the critical value ($\Pi \approx 10^{-12}\,\mathrm{cm}^2$) above which the effect of Π on the timescale of the propagation becomes negligible (see also section 6.6.2). Clays are unlikely to have permeabilities smaller than the ones used here, unless they are affected by a large amount of pore ice, which wasn't observed experimentally.

Some evidence also exists on the temperature required for the first ice lens to grow. Watanabe (2002), during his experiments in a system of silica microspheres, observed new ice lenses at an undercooling of just 0.02 K. Using a fracture toughness of $K = 10^2\,\mathrm{Pa}\cdot\,\mathrm{m}^{1/2}$ and an initial radius of $R_0 = 0.0011\,\mathrm{cm}$ (values taken from Style *et al.*, 2011), our theory predicts that the minimum temperature

for fracturing to occur is $\Delta T = 0.024\,\mathrm{K}$. In experiments with kaolinite clay with $K = 1.5\,\mathrm{MPa}\cdot\,\mathrm{m}^{1/2}$ and $R_0 = 0.001\,\mathrm{cm}$, Style *et al.* (2011) observed lenses forming at temperatures of $-0.3^\circ\,\mathrm{C}$, where our theory predicts a minimum undercooling of $0.37\,\mathrm{K}$ required for fracturing. The agreement with predictions from both experiments is good. This reinforces the idea that ice lens formation in soils can be described by ideas similar to fracturing in rocks, and our model seems to be in good agreement with existing observations and experimental data in soils.

7.8 Conclusions

In this chapter, our aim has been to further explore the model developed and solved in chapter 6 to understand some real-life situations of frost fracturing. We have also discussed some existing models and determined ways in which our work complements and extends past studies.

We have discussed the work of Walder & Hallet (1985) and compared our predictions for the growth rate of a cavity to theirs. After incorporating some of the features of their model in ours we have managed to achieve good agreement and understand where the small differences in predictions come from. We have also discussed some aspects of the work of Murton *et al.* (2006) and found that our estimates for the minimum radii for propagation are in good agreement.

Extending the work done in chapter 6, we have studied the effect of several parameters on the fracturing potential of an existing fault. This has led us to some important conclusions about the properties required for a material to be frost-proof. Interestingly, it is only the fracture toughness of the material and the size of pre-existing faults that affect the potential for fracturing at a given temperature, while all other material parameters can only affect the time scale of the process once it occurs.

Following from the discussion of the existence of pore ice, motivated by the work of Walder & Hallet (1985) and Murton *et al.* (2006), we have attempted to incorporate a frozen fringe in our model. We suggested a rule to describe the undercooling-dependent permeability and demonstrated the effect that a variable

permeability has on the propagation rate. The existence of pore ice is a non-straightforward subject that requires a lot more theoretical work, coupled with experimental evidence, which is beyond the scope of this thesis. We have shown though that our model is flexible enough to include these ideas.

Finally, we have explained how our model can be used to describe fracturing in clays, and analyzed the main features that differentiate this from rock fracturing. With the studies of rock fracturing and frost heaving revealing many similarities between the two processes, our work can serve as a theoretical model for the analysis of a large variety of frost fracturing problems. Our model agrees with experimental data of the prediction of the temperature needed for ice lenses to grow, as well as evidence on ice lens growth rates. It also reproduces other features that have been observed experimentally, such as the sudden surge of heave at the initial stages of ice lens formation.

Chapter 8

Conclusions and future work

The aim of this thesis has been to study the phenomenon of frost fracturing of rocks due to water freezing inside them at low temperatures, and develop a theoretical model describing ice growth and crack propagation from fundamental physical principles. We summarized past theoretical and experimental studies in chapter 1, where we identified considerable progress in the theoretical modelling of frost cracking. The important role played by unfrozen films of water between ice and rock has been identified by several studies. The physics causing and governing these films were presented in chapter 2. The balance of pressures across these premelted films determines the fracturing of an ice-filled crack and forms the basis of our theoretical model.

The first problem we discussed was that of ice growth inside a spherical cavity in a porous, elastic medium. The aim of using this simple geometry was to

compare the contributions of two different processes on the pressure acting on the rock: the expansion of water during freezing, and the disjoining forces acting across the thin premelted film in almost-filled cavities. The important conclusion here was that the effect of expansion on the pressure applied to the rock is negligible for media more permeable than about $\Pi \approx 10^{-15}\,\mathrm{cm}^2$.

The ideas deduced from the spherical model allowed us to develop a theoretical model for a more realistic geometry, concentrating on the important premelting stage rather than the initial ice growth. The 3D penny-shaped crack problem, first developed in chapter 4, was studied both in the framework of a similarity solution for a warming environment, and as a time-dependent problem. Both these approaches provided us with the opportunity to study the existence of solutions for different values of the rock parameters, as well as the undercooling of the environment. The different regimes were summarized in figure 5.7, and we developed a criterion predicting whether a pre-existing fault will fracture. This can be expressed in terms of the fracture toughness of the material, over the undercooling of the environment

$$\frac{K}{\Delta T} < \frac{2}{\sqrt{\pi}} R_0^{1/2} \frac{\rho_s \mathcal{L}}{T_m}. \tag{8.1}$$

In the case where this condition is not met, ice can still grow inside the cavity and deform it without fracturing it. The process continues with the thickness of the cavity increasing until an equilibrium is reached where the disjoining pressure between the ice and the rock is balanced by the elastic response of the medium.

We also established that for the permeability of the medium to affect the fracturing potential of a fault, the undercooling of the environment needs to vary with time. For example, in the case of a warming environment described in chapter 5, the maximum value of $K/\Delta T$ for which fracturing can occur behaves as

$$\beta = \max\{\frac{\tilde{K}}{\tilde{H}}\} \sim \frac{\tilde{\Pi}^{1/4}}{(1+\tilde{\Pi})^{1/4}}. \tag{8.2}$$

In cases with constant ΔT, the permeability of the medium only affects the timescale of growth. In either situation, only permeabilities smaller than about $10^{-12}\,\mathrm{cm}^2$ have an important effect on either the fracturing potential or the fracturing rate. A similar behaviour was found with the elastic modulus m, which

also affects only the timescale of the problem.

Another interesting result is associated with the initial size of a fault. As expected, media with smaller faults are less prone to fracturing (see section 7.4.2) as, due to their shorter length, larger pressure is required for the stress at the tip to reach the critical value. We did see in section 6.6.3 though that the fracturing rate of a crack is dependent only on its current size rather than its initial size, which means that the growth curves of two cracks of different initial sizes will coincide if all other parameters are the same.

General patterns of dependence of the growth curves of a cavity on different parameters of the problem were established. The ratio of fracture toughness to undercooling not only determines the susceptibility of a medium to fracturing, but also strongly affects the propagation rate, with a larger $K/\Delta T$ ratio resulting in slower propagation. The growth rate is also proportional to the elastic modulus of the medium, hence stiff rocks are expected to fracture quickly. The fast growth rates (mm/ sec) found for some rocks can be attributed to the fact that we have considered the permeability of the medium to remain unchanged even for low temperatures, but the concept of pore ice is easy to incorporate in our model. We considered under which conditions a pore of a given size will become ice-filled. This allowed us to construct an expression for the effective permeability of a medium with pore ice as an attempt to quantify its effect on the water flow through the medium. We found that, in the presence of pore ice, maximum growth rates come from undercoolings of around $5 - 10^{\circ}$ C. We believe that it is important to establish a better understanding of the existence of pore ice in frozen media, through either experimental or field observations.

An important point of the thesis is that the model developed here can also be used to describe the growth of ice lenses in soils, as these have been observed to have crack-like behaviour. Treating saturated soils as elastic media means that ice lens growth is predicted without the need for a frozen fringe, which is in agreement with observations. The results from our model agree with experimental observations of the warmest temperature at which an ice lens can form. It is also in good agreement with the order of magnitude of ice lens growth observed in experiments. The surge in heave during early times, which has been seen experimentally, is also present in our results.

In conclusion, we have developed a theoretical model which we believe can describe both fracturing in rocks as well as ice lens growth in cohesive soils. The model is based on fundamental physical ideas, and explains the nature of the thin films of water existing between ice and medium which are critical in the process of fracturing. We have shown that different features can be incorporated into the model, such as a variable permeability or temperature, to obtain results for specific environmental conditions. Much experimental work done in previous decades was focused around concepts such as the expansion of water upon freezing, which resulted in the study of only specific parameters of the problem and environmental conditions necessary for the expansion effect to be important. The existence of a theoretical model and the analysis of the several parameters of the problem that we have performed in this thesis can assist with steering future experimental work in the right direction. In addition to this, if phenomena like pore ice or freezing rates are found to be important, the model is capable of coupling a time-dependent temperature with the resulting effective permeability to investigate their effect on the growth rate of cracks.

While we believe that the penny-shaped geometry here is applicable to many real-life situations, and we do not expect the results to be very sensitive to it, the mathematical and physical ideas that we have developed can be modified for different geometries too. For example, ice lenses in soils have been observed to grow off vertical ice-filled cracks (Arenson *et al.*, 2008; Style *et al.*, 2011). This indicates that a 2D wedge geometry could be applicable. Suitable solutions for both the solid and liquid pressure fields can be found for a quarter plane configuration, which could then be used to develop a similar model for the wedge geometry.

Appendix A

Linear Elasticity

A.1 The biharmonic equation in cylindricals

In cylindricals, the equations relating the stress to the displacement can be written in the form:

$$\sigma_{rr} = (\lambda + 2G)\frac{\partial u_r}{\partial r} + \lambda\frac{u_r}{r} + \lambda\frac{\partial u_z}{\partial z}, \tag{A.1}$$

$$\sigma_{\theta\theta} = \lambda\frac{\partial u_r}{\partial r} + (\lambda + 2G)\frac{u_r}{r} + \lambda\frac{\partial u_z}{\partial z}, \tag{A.2}$$

$$\sigma_{zz} = \lambda\frac{\partial u_r}{\partial r} + \lambda\frac{u_r}{r} + (\lambda + 2G)\frac{\partial u_z}{\partial z}, \tag{A.3}$$

$$\sigma_{rz} = G\left(\frac{\partial u_r}{\partial z} + \frac{\partial u_z}{\partial r}\right), \tag{A.4}$$

where the subscripts represent components of the stress tensor σ and the displacement vector $\mathbf{u}$. Lamé's first parameter is represented by λ, while G is the shear modulus. Now, if we let

$$u_r = \frac{\lambda + G}{G} \Phi_{rz}, \tag{A.5}$$

$$u_z = \frac{\lambda + 2G}{G} \nabla^2 \Phi - \frac{\lambda + G}{G} \Phi_{zz}, \tag{A.6}$$

where the subscripts of the function $\Phi(r, z)$ describe partial differentiation. Then, the expressions for the stress components become

$$\sigma_{rr} = \lambda \nabla^2 \Phi_z - 2(\lambda + G)\Phi_{rrz}, \tag{A.7}$$

$$\sigma_{zz} = (3\lambda + 4G)\nabla^2 \Phi_z - 2(\lambda + G)\Phi_{zzz}, \tag{A.8}$$

$$\sigma_{\theta\theta} = \nabla^2 \Phi_z - \frac{2}{r}(\lambda + G)\Phi_{zr}, \tag{A.9}$$

$$\sigma_{rz} = (\lambda + 2G)\frac{\partial}{\partial r}\nabla^2 \Phi - 2(\lambda + G)\Phi_{zzr}, \tag{A.10}$$

which, when substituted into the equilibrium equations, imply that $\Phi(r, z)$ must satisfy the biharmonic equation:

$$\nabla^4 \Phi = 0. \tag{A.11}$$

A.2 Pressure and displacement fields in terms of Bessel functions

We want to use the function Φ to find an expression relating the displacement and press distribution fields. In cylindrical coordinates we note the following identity

$$\int_0^\infty r \nabla^2 f J_0(\xi r)\, dr = \left(\frac{\mathrm{d}^2}{\mathrm{d}z^2} - \xi^2\right) \int_0^\infty r f J_0(\xi r)\, dr. \tag{A.12}$$

where J_0 is the Bessel function of the first kind of order zero. If we use this with $f = \nabla^2 \Phi$ and then again with $f = \Phi$ we find

$$\left(\frac{\mathrm{d}^2}{\mathrm{d}z^2} - \xi^2\right)^2 F(\xi, z) = \int_0^\infty r \nabla^4 \Phi J_0(\xi r)\, dr = 0, \tag{A.13}$$

where

$$F(\xi, z) = \int_0^\infty r\Phi J_0(\xi r)\, dr. \tag{A.14}$$

The solution to equation $(A.13)$ is

$$F(\xi, z) = [A(\xi) + zB(\xi)]\, e^{-\xi z}, \tag{A.15}$$

where we have assumed that Φ decays at infinity. Now, by multiplying equation (A.5) by $rJ_1(\xi r)$ and integrating from 0 to ∞ we find

$$\int_0^\infty r u_r J_1(\xi r)\, dr = \frac{\lambda + G}{G} \xi \frac{dF}{dz}. \tag{A.16}$$

We use the following identity to invert the integral

$$\int_0^\infty J_n(xu)(xu)^{1/2}\, du \int_0^\infty J_n(yu)(yu)^{1/2} f(y)\, dy = f(x) \quad \text{for} \quad n \geq -\frac{1}{2} \tag{A.17}$$

and find an expression for u_r:

$$u_r = \frac{\lambda + G}{G} \int_0^\infty \xi^2 \frac{dF}{dz} J_1(\xi r)\, d\xi. \tag{A.18}$$

Similarly,

$$u_z = \int_0^\infty \xi \left(\frac{d^2F}{dz^2} - \frac{\lambda + 2G}{G} \xi^2 F \right) J_0(\xi r)\, d\xi, \tag{A.19}$$

$$\sigma_{zz} = \int_0^\infty \xi \left[(\lambda + 2G) \frac{d^3F}{dz^3} - (3\lambda + 4G)\xi^2 \frac{dF}{dz} \right] J_0(\xi r)\, d\xi, \tag{A.20}$$

$$\sigma_{rz} = \int_0^\infty \xi^2 \left[\lambda \frac{d^2F}{dz^2} + (\lambda + 2G)\xi^2 F \right] J_1(\xi r)\, d\xi \tag{A.21}$$

,

$$\sigma_{rr} + \sigma_{\theta\theta} = 2 \int_0^\infty \xi \left(\lambda \frac{d^3F}{dz^3} + G\xi^2 \frac{dF}{dz} \right) J_0(\xi r)\, d\xi. \tag{A.22}$$

We can use the equation of equilibrium

$$\frac{\partial}{\partial r} \left(r^2 \sigma_{rr} \right) = r(\sigma_{rr} + \sigma_{\theta\theta}) - r^2 \frac{\partial \sigma_{rz}}{\partial z}. \tag{A.23}$$

We substitute for the expressions for $\sigma_{rr} + \sigma_{\theta\theta}$ and σ_{rz} and integrate to find

$$\sigma_{rr} = \int_0^\infty \xi \left[\lambda \frac{d^3F}{dz^3} + (\lambda + 2G)\xi^2 \frac{dF}{dz} \right] J_0(\xi r)\, d\xi - \frac{2(\lambda + G)}{r} \int_0^\infty \xi^2 \frac{dF}{dz} J_1(\xi r)\, d\xi \tag{A.24}$$

and therefore

$$\sigma_{\theta\theta} = \lambda \int_0^\infty \xi \left(\frac{d^3F}{dz^3} - \xi^2 \frac{dF}{dz} \right) J_0(\xi r)\, d\xi + \frac{2(\lambda + G)}{r} \int_0^\infty \xi^2 \frac{dF}{dz} J_1(\xi r)\, d\xi. \tag{A.25}$$

Appendix B

Numerical method for time-dependent penny-shaped problem

We use a mid-point rule to represent the cavity shape which means that inside the nth interval

$$B^i = \frac{B^i_n + B^i_{n+1}}{2} \tag{B.1}$$

at the i-th iteration in time. Then

$$\frac{\partial B^i}{\partial \eta} = N(B^i_{n+1} - B^i_n) \tag{B.2}$$

and

$$\frac{\partial B^i_n}{\partial t} \approx \frac{B^i - B^{i-1}}{\Delta t} = \frac{B^i_n + B^i_{n+1} - B^{i-1}_n - B^{i-1}_{n+1}}{2\Delta t} \tag{B.3}$$

We will treat the interval which includes the tip of the ice a bit more carefully. We define $\Lambda = \lceil \lambda N \rceil$, so that the ice tip is in the Λth interval. Then, we

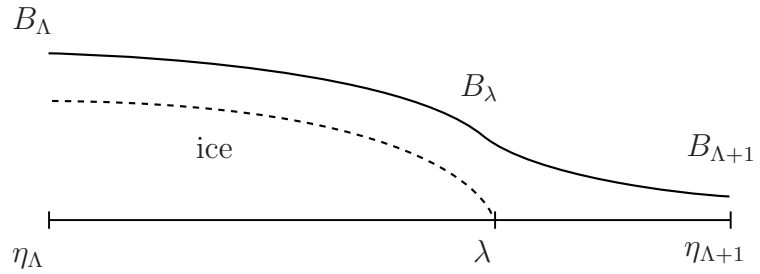

approximate the width of the ice at $\eta = \lambda$ as

$$B^i_\lambda = B^i(\lambda) = N(\eta_{\Lambda+1} - \lambda^i)B^i_\Lambda + N(\lambda^i - \eta_\Lambda)B^i_{\Lambda+1} \tag{B.4}$$

Then, inside the Λth interval (as shown in figure B) we have

$$B^i = \frac{B^i_\Lambda + B^i_\lambda}{2} = \frac{1}{2}\left[(N\eta_{\Lambda+1} - N\lambda^i + 1) + N(\lambda^i - \eta_\Lambda)B^i_{\Lambda+1}\right], \tag{B.5}$$

$$\tag{B.6}$$

$$\frac{\partial B^i}{\partial \eta} = \frac{B^i_\lambda - B^i_\Lambda}{\lambda^i - \eta_\Lambda} = N(B^i_{\Lambda+1} - B^i_\Lambda) \tag{B.7}$$

and

$$\frac{\partial B^i}{\partial t} = \frac{B^i - B^{i-1}}{\Delta t} = \frac{1}{2\Delta t}\left[(N\eta_{\Lambda+1} - N\lambda^i + 1)B^i_\Lambda + N(\lambda^i - \eta_\Lambda)B^i_{\Lambda+1} - \right.$$

$$\left. - (N\eta^i_{\Lambda+1} - N\lambda^{i-1} + 1)B^{i-1}_\Lambda - N(\lambda^{i-1} - \eta^i_\Lambda)B^{i-1}_{\Lambda+1}\right] \tag{B.8}$$

We denote the midpoint of each interval with $\sigma_n = (2n-1)/2N$ and use the midpoint rule to approximate the integral expressions for P_s, P_l and Θ^I as follows

$$P^i_s(\eta_j) = -\sum_{n=1}^{N} f^i_s(\eta_j, \sigma_n) \tag{B.9}$$

$$P^i_l(\eta_j) = \begin{cases} -\sum_{n=1}^{N} f^i_l(\eta_j, \sigma_n) & , j \le \Lambda \\ \\ -\sum_{n=1}^{N} f^i_l(\eta_\Lambda, \sigma_n) & , j > \Lambda \end{cases} \tag{B.10}$$

$$\Theta^{I^i}(\eta_j) = \sum_{n=1}^{\Lambda^i - 1} f_l^i(\eta_j, \sigma_n) + f_l^i(\eta_j, \sigma_\lambda^i) \tag{B.11}$$

where $\sigma_\lambda^i = (\eta_{\Lambda^i} + \lambda^i)/2$. The new functions f_s^i and f_l^i that we have introduced are given by

$$f_s^i(\eta_j, \sigma_n) = \frac{1}{\sigma_n} M^* \left(\frac{\eta_j}{\sigma_n} \right) (B_{n+1}^i - B_n^i) \tag{B.12}$$

$$\begin{aligned} f_l^i(\eta_j, \sigma_n) &= \alpha_{jn} R^i \left\{ \left[(2n+1)R^i - 2nR^{i-1} \right] B_n^i - R^i B_n^{i-1} + \right. \\ &+ \left. \left[(3-2n)R^i + (2n-2)R^{i-1} \right] B_{n+1}^i - R^i B_{n+1}^{i-1} \right\} \end{aligned} \tag{B.13}$$

$$\tag{B.14}$$

and

$$\begin{aligned} f_l^i(\eta_j, \sigma_\lambda^i) &= \alpha_{j\lambda} R^i \left\{ \left[(3N\eta_\Lambda - N\lambda^i + 4)R^i + 2(N\eta_\Lambda + 1)R^{i-1} \right] B_\Lambda^i \right. \\ &+ -(N\eta_\Lambda - N\lambda^i + 2)R^i B_\Lambda^{i-1} + \left[N(\lambda^i - 3\eta_\Lambda)R^i + 2N\eta_\Lambda R^{i-1} \right] B_{\Lambda+1}^i - \\ &+ \left. -N(\lambda^i - \eta_\Lambda)R^i B_{\Lambda+1}^{i-1} \right\} \end{aligned} \tag{B.15}$$

$$\tag{B.16}$$

We now have

$$P_s^i(\eta_j) = \sum_{n=1}^{N} (\mu_{jn} - \mu_{j(n-1)}) B_n^i \quad \text{where} \quad \mu_{jn} = \frac{1}{\sigma_n} M^* \left(\frac{\eta_j}{\sigma_n} \right) \tag{B.17}$$

$$P_l^i(\eta_j) = \begin{cases} -\sum_{n=1}^{N} (\alpha_{jn}\beta_n^i + \alpha_{j(n-1)}\gamma_n^i) B_n^i + \sum_{n=1}^{N} (\alpha_{jn} + \alpha_{j(n-1)}) R^{i^2} B_n^{i-1} & , j \le \Lambda \\ -\sum_{n=1}^{N} (\alpha_{\Lambda n}\beta_n^i + \alpha_{\Lambda(n-1)}\gamma_n^i) B_n^i + \sum_{n=1}^{N} (\alpha_{\Lambda n} + \alpha_{\Lambda(n-1)}) R^{i^2} B_n^{i-1} & , j > \Lambda \end{cases} \tag{B.18}$$

with

$$\alpha_{jn} = \frac{1}{2N\Delta t} \frac{\sigma_n}{\eta_j + \sigma_n} K \left(\frac{2\sqrt{\eta_j \sigma_n}}{\eta_j + \sigma_n} \right) \quad \text{and} \quad \begin{aligned} \beta_n^i &= (2n+1)R^{i^2} - 2nR^i R^{i-1} \\ \gamma_n^i &= (5-2n)R^{i^2} - (2n-4)R^i R^{i-1} \end{aligned} \tag{B.19}$$

$$\begin{aligned}\Theta^{I^i}(\eta_j) &= \sum_{n=1}^{\Lambda-1}(\alpha_{jn}\beta_n^i + \alpha_{j(n-1)}\gamma_n^i)B_n^i + (\alpha_{j(\Lambda-1)}\gamma_\Lambda^i + \alpha_{j\lambda}^i\beta_\lambda^i)B_\Lambda^i + \alpha_{j\lambda}^i\gamma_\lambda^i B_{\Lambda+1}^i - \\ &- \sum_{n=1}^{\Lambda-1}(\alpha_{jn} + \alpha_{j(n-1)})R^{i^2}B_n^{i-1} - (\alpha_{j(\Lambda-1)}R^{i^2} + \alpha_{j\lambda}^i\delta_\lambda^i)B_\Lambda^{i-1} - \alpha_{j\lambda}^i\epsilon_\lambda^i B_{\Lambda+1}^{i-1}\end{aligned} \tag{B.20}$$

where

$$\alpha_{j\lambda}^i = \frac{\lambda^i - \eta_\Lambda}{2\Delta t}\frac{\sigma_\lambda}{\eta_j + \sigma_\lambda}K\left(\frac{2\sqrt{\eta_j\sigma_\lambda}}{\eta_j + \sigma_\lambda}\right) \tag{B.21}$$

$$\beta_\lambda^i = (3N\eta_\Lambda - N\lambda^i + 4)R^{i^2} - 2(N\eta_\Lambda + 1)R^iR^{i-1} \tag{B.22}$$

$$\gamma_\lambda^i = N(\lambda^i - 3\eta_\Lambda)R^{i^2} + 2N\eta_\Lambda R^iR^{i-1} \tag{B.23}$$

$$\delta_\lambda^i = (N\eta_\Lambda - N\lambda^i + 2)R^{i^2} \tag{B.24}$$

$$\epsilon_\lambda^i = N(\lambda^i - \eta_\Lambda)R^{i^2} \tag{B.25}$$

$$\tag{B.26}$$

Pressure balance:

$$P_s^i(\eta_j) - P_l^i(\eta_j) = \begin{cases} = \tilde{H}\tilde{K}^{-1} - \tilde{\Pi}\Theta^{I^i}(\eta_j) & \text{if } j < \Lambda \\ = N(\lambda^i - \eta_\Lambda)\left(\tilde{H}\tilde{K}^{-1} - \tilde{\Pi}\Theta^{I^i}(\eta_j)\right) & \text{if } j = \Lambda \\ = 0 & \text{if } j > \Lambda \end{cases} \tag{B.27}$$

Appendix C

Method for estimating integrals over intervals with pole singularities

In general, we integrate numerically by using a gaussian quadrature, which can deal with weak singularities at an endpoints c like $\log(x-c)$ and $1/\sqrt{x-c}$. Some intervals though require special treatment because they have stronger singularities. The kernel $M(\eta/\sigma)$ has a pole singularity at $\sigma = \eta$. The elliptic integrals $K(z)$ and $E(z)$ have the following expansions around $z = 1$:

$$K(z) \approx -\frac{1}{2}\log(1-z)\,(1+O(z-1)) + \log 4 + O(z-1) \tag{C.1}$$

and

$$E(z) \approx 1 + \log(1-z)O(z-1) + O(z-1), \tag{C.2}$$

hence the singularities are at most logarithmic. For S_{nn} and T_{nn} (i.e. the intervals that include the pole singularity) we use the following method. Suppose we want

to integrate

$$I = \fint_{\eta_{n-1}}^{\eta_n} \frac{f(\sigma,\eta)\,d\sigma}{(\sigma-\eta)\sqrt{1-\sigma^2}} = I_- + I_+ = \tag{C.3}$$

$$= \lim_{\epsilon\to 0^+}\left[\int_{\eta_{n-1}}^{\eta-\epsilon} \frac{f_1(\sigma,\eta)\,d\sigma}{(\sigma-\eta)\sqrt{1-\sigma^2}} + \int_{\eta+\epsilon}^{\eta_n} \frac{f_2(\sigma,\eta)\,d\sigma}{(\sigma-\eta)\sqrt{1-\sigma^2}}\right] \tag{C.4}$$

We want to subtract the singularity in order to be left with some integral that can be integrated numerically using a gaussian quadrature. To do so, we subtract the residue in the following way:

$$I_- = \int_{\eta_{n-1}}^{\eta-\epsilon} \frac{f_1(\sigma,\eta)-f_1(\eta,\eta)}{(\sigma-\eta)\sqrt{1-\sigma^2}}\,d\sigma + f_1(\eta,\eta)\int_{\eta_{n-1}}^{\eta-\epsilon} \frac{d\sigma}{(\sigma-\eta)\sqrt{1-\sigma^2}} =$$

$$\approx \int_{\eta_{n-1}}^{\eta-\epsilon} \frac{{f_1}'(\sigma,\eta)}{\sqrt{1-\sigma^2}}\,d\sigma + f_1(\eta,\eta)\int_{\eta_{n-1}}^{\eta-\epsilon} \frac{d\sigma}{(\sigma-\eta)\sqrt{1-\sigma^2}}, \tag{C.5}$$

which then gives for the whole integral

$$I = \int_{\eta_{n-1}}^{\eta} \frac{{f_1}'(\sigma,\eta)}{\sqrt{1-\sigma^2}}\,d\sigma + \int_{\eta}^{\eta_n} \frac{{f_2}'(\sigma,\eta)}{\sqrt{1-\sigma^2}}\,d\sigma + f(\eta,\eta)\fint_{\eta_{n-1}}^{\eta_n} \frac{d\sigma}{(\sigma-\eta)\sqrt{1-\sigma^2}}, \tag{C.6}$$

where $f(\eta,\eta) = f_1(\eta,\eta) = f_2(\eta,\eta)$ since $f(\sigma,\eta)$ is continuous at $\sigma=\eta$. The last integral is a Cauchy principal value integral and when evaluated gives

$$\fint_{\eta_{n-1}}^{\eta_n} \frac{d\sigma}{(\sigma-\eta)\sqrt{1-\sigma^2}} = \frac{1}{\sqrt{1-\eta^2}}\log\left(\frac{1+\sqrt{1-\eta^2}\sqrt{1-\eta_{n-1}^2}-\eta\eta_{n-1}}{1+\sqrt{1-\eta^2}\sqrt{1-\eta_n^2}-\eta\eta_n}\right). \tag{C.7}$$

The remaining integrals are approximated numerically using a Gaussian quadrature since their singularities are weak enough. This analysis can be applied for both S_{nn} and T_{nn}.

Appendix D

Assumption of uniform pressure in the tip of the crack

In chapter 5, we used the thin film approximation inside all of the cavity in order to describe the flow of water. This assumed that both the premelted film occupying $r < \lambda R$ as well as the cavity at $r > \lambda R$ are thin enough for the flow along them to be negligible. If this is not true for the $r > \lambda R$ region, we can instead use the uniform pressure assumption, which implies that the flow along the cavity dominates the flow from the porous medium into the cavity, so that any pressure variations are evened out quickly. These two ideas represent the opposite ends of the spectrum but we will see that they make only a small difference to the overall characteristics of the problem.

The liquid pressure in the porous medium is given as an integral of the flux

into the cavity $q(r,t)$

$$p_l(r,t) = \frac{1}{\pi}\frac{\mu}{\Pi}\int_0^{R(t)} K\left(\frac{2\sqrt{rs}}{r+s}\right) q(s,t)\frac{s\,ds}{s+r}, \tag{D.1}$$

The flux is related to the derivative of the liquid pressure through

$$q(r,t) = -\frac{2\Pi}{\mu}\lim_{z\to 0}\frac{\partial p}{\partial z} \tag{D.2}$$

and for the ice-occupied region, lubrication theory gives

$$q(r,t) = -\frac{2\Pi}{\mu}\lim_{z\to 0}\frac{\partial p}{\partial z} = -2\frac{\partial b}{\partial t}. \tag{D.3}$$

The liquid pressure now becomes

$$\begin{aligned} p_l(r,t) &= -\frac{2}{\pi}\frac{\mu}{\Pi}\int_0^{\lambda R(t)} K\left(\frac{2\sqrt{rs}}{r+s}\right)\frac{\partial b}{\partial t}\frac{s\,ds}{s+r} - \\ &\quad -\frac{2}{\pi}\frac{\mu}{\Pi}\int_{\lambda R(t)}^{R(t)} K\left(\frac{2\sqrt{rs}}{r+s}\right)\left.\frac{\partial p_l}{\partial z}\right|_{z=0}\frac{s\,ds}{s+r}, \end{aligned} \tag{D.4}$$

with the condition of uniform pressure in the water-filled tip of the crack

$$p_l(r,t) = p_l(\lambda R,t) \quad \text{for} \quad r > \lambda R. \tag{D.5}$$

Following the same process as in chapter 5, we can write down the equations describing the similarity solution for $\Delta T = Ht^{-1/4}$. The dimensionless liquid pressure is given by

$$\begin{aligned} P_l(\eta) &= -k^2\int_0^{\lambda} K\left(\frac{2\sqrt{\eta\sigma}}{\eta+\sigma}\right)\left[\frac{1}{4}B(\sigma) - \frac{1}{2}\sigma B'(\sigma)\right]\frac{\sigma d\sigma}{\eta+\sigma} - \\ &\quad -\frac{2k}{\pi}\int_{\lambda}^{1} K\left(\frac{2\sqrt{\eta\sigma}}{\eta+\sigma}\right) P_l^z(\sigma)\frac{\sigma d\sigma}{\eta+\sigma}, \end{aligned} \tag{D.6}$$

where we denote $P_l^z(\sigma) = \left.\dfrac{\partial P_l(\sigma,z)}{\partial z}\right|_{z=0}$. The temperature is given by equa-

tion (5.23) as in chapter 5, hence the liquid pressure can be written as

$$P_l(\eta) = -\Theta^I(\eta) - \frac{2k}{\pi}\int_\lambda^1 K\left(\frac{2\sqrt{\eta\sigma}}{\eta+\sigma}\right) P_l^z(\sigma)\frac{\sigma d\sigma}{\eta+\sigma} \equiv -\Theta^I(\eta) - \Phi(\eta). \quad \text{(D.7)}$$

The pressure balance can then be re-written as

$$\begin{aligned} P_s(\eta) &= (\tilde{\Pi}+1)P_l(\eta) + \tilde{\Pi}\Phi(\eta) + \tilde{\Pi}C \quad \text{for} \quad \eta < \lambda. \\ &= P_l(\eta) \qquad\qquad\qquad\qquad\quad \text{for} \quad \eta > \lambda. \end{aligned} \quad \text{(D.8)}$$

We use the same discretization method as in section 5.2.1. The difference here is that since the terms P_l^z cannot be written in terms of the cavity thickness B, they have to be determined from the matrix problem. The simplest way to write it is to assume $2N$ unknowns, $[B_1, ...B_N]$ and $[P_{l_1}, ...P_{l_\Lambda}, P^z_{l_{\Lambda+1}}, ...P^z_{l_N}]$, where $P_{l_n} = P_l(\eta_n)$. We have N conditions from the expression for the liquid pressure (D.7)

$$\delta_{jn}P_{l_n} + \frac{8k}{\pi}\sum_{n=\Lambda+1}^{N}(\lambda_{jn}+\nu_{jn})P^z_{l_n} + k^2\sum_{n=1}^{\Lambda-1}(\lambda_{jn}+\nu_{j(n-1)})B_n + \\ +k^2(\nu_{j(n-1)} + I_j^\lambda)B_\Lambda + k^2 J_j^\lambda B_{\Lambda+1} = 0, \quad \text{(D.9)}$$

which is valid for $j \leq \Lambda$, while for $j > \Lambda$ the first term is replaced by P_{l_Λ} to account for the uniform pressure condition in the water-filled tip. The pressure balance in the ice-filled region provides us with a further Λ conditions for $j \leq \Lambda$

$$(\tilde{\Pi}+1)\delta_{jn}P_{l_n} + \frac{8k}{\pi}\tilde{\Pi}\sum_{n=\Lambda+1}^{N}(\lambda_{jn}+\nu_{jn})P^z_{l_n} - \\ -\sum_{n=1}(\mu_{jn}-\mu_{j(n-1)})B_n = -\tilde{\Pi}C, \quad \text{(D.10)}$$

while for $j > \Lambda$ we have the following $N - \Lambda$ conditions

$$P_{l_\Lambda} - \sum_{n=1}(\mu_{jn}-\mu_{j(n-1)})B_n = 0. \quad \text{(D.11)}$$

The $2N$ linear relations described by equations (D.9)-(D.11) replace the matrix equation of section 5.2.1.

We produce a phase plane of the solutions for different values of the parameters for $\tilde{H}$ and $\tilde{K}$ produced by both this method and the lubrication approximation method first presented in chapter 5. The comparison can be seen in figure D.1

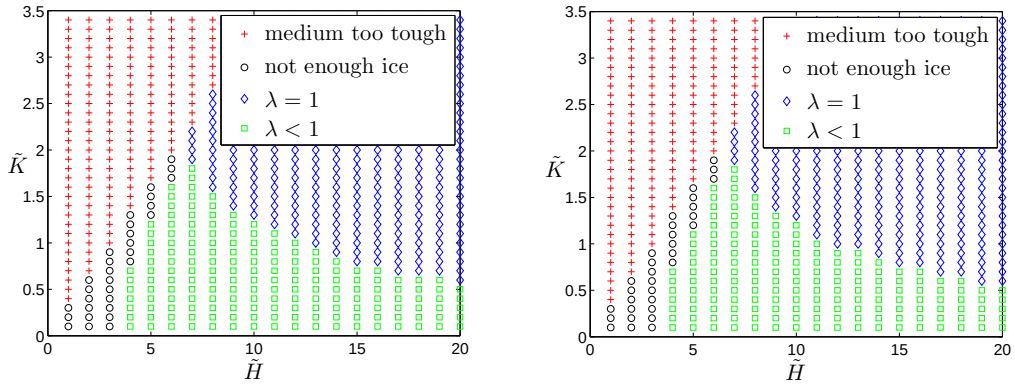

Figure D.1: *A plot of $\tilde{K}$ against $\tilde{H}$ for $\tilde{\Pi} = 2$ showing the regions of existence of fast solutions as produced by the lubrication approximation method (left) and the method of uniform pressure in the tip, presented in this appendix (right).*

where the two graphs are presented and they look identical. Indeed, only 4 points belong to different regimes in the two plots. The (5, 1.2) changes from the propagating green squares regime to the black circles, which describes cavities where the ice cannot grow far enough towards the tip to cause high enough stresses for fracturing. Points (11, 1.1), (12, 1) and (19, 0.6) describe partially filled cavities in the phase plane on the left, but become fully ice-filled when we assume uniform pressure in the tip, in the phase plane on the right. These points are on the boundary between different regimes which indicates that the differences are small.

Appendix E

Freezing temperature depression of a spherical nucleus in a spherical pore

Consider a spherical pore of radius R with ice growing inside it. Two effects contribute to the depression of the freezing temperature: the curvature of the spherical ice nucleus, and the disjoining forces which become important when the pore is almost filled with ice. This is shown by the following relation

$$\rho_s \mathcal{L} \frac{T_m - T}{T_m} = p_T + \kappa\gamma = \frac{\mathcal{A}}{6\pi(R-a)^3} + \frac{2\gamma}{a}, \tag{E.1}$$

where we have assumed that the ice is also spherical, with radius a. The depression of T due to curvature melting decreases as the ice grows, whereas the disjoining pressure p_T becomes larger the closer the ice is to the rock. Since these two effects act in opposing ways, there is a radius of ice for which the depression of

the freezing temperature is minimised. This is of interest when considering the existence of pore ice in a porous medium. If the minimum $T_m - T$ occurs for an almost ice-filled cavity, we can assume that at a given undercooling all pores larger than a given size are completely ice-filled, while the smaller ones are devoid of ice. It is also useful to determine which term dominates the depression of the temperature at that stage. Minimising the right-hand-side of equation (E.1) with respect to a, we find

$$(R-a)^4 - \frac{\mathcal{A}}{4\pi\gamma}a^2 = 0. \tag{E.2}$$

Defining $c = \mathcal{A}/(4\pi\gamma)$, we find

$$R = a \pm c^{1/4}a^{1/2}. \tag{E.3}$$

Setting $x = a^{1/2}$ we have two quadratic equations for x

$$x^2 \pm c^{1/4}x - R = 0 \tag{E.4}$$

with four solutions

$$x = \frac{\mp c^{1/4} \pm \sqrt{c^{1/2} + 4R}}{2}. \tag{E.5}$$

Of these solutions, only one satisfies $0 < a < R$ (the first minus and the second plus) and gives

$$a_{\min} = R + \frac{1}{2}c^{1/4}\left(c^{1/4} - \sqrt{c^{1/2} + 4R}\right). \tag{E.6}$$

For typical values of the parameters, R is about 7 orders of magnitude larger than $c^{1/2}$ which means that we can expand the square root to find

$$a_{\min} = R - c^{1/4}R^{1/2} + \frac{1}{2}c^{1/2} + c^{1/4}O(\epsilon^2), \tag{E.7}$$

where $\epsilon^2 = c^{1/2}/R = O(10^{-7})$ and the terms on the right-hand-side are ordered in decreasing size. This shows that the first and second order terms are $R(1-\epsilon)$, where $\epsilon = O(10^{-3}) - O(10^{-4})$. Substituting into equation (E.1) we find the

minimum undercooling

$$\begin{aligned}
\min \frac{\rho_s \mathcal{L} \Delta T}{2\gamma T_m} &= \frac{1}{3} c (R - a_{\min})^{-3} + a_{\min}^{-1} \\
&= \frac{1}{3} c (c^{1/4} R^{1/2} - \frac{1}{2} c^{1/2})^{-3} + (R - c^{1/4} R^{1/2} + \frac{1}{2} c^{1/2})^{-1} \\
&= \frac{1}{3} c^{1/4} R^{-3/2} (1 - O(\epsilon))^{-3} + R^{-1} (1 - O(\epsilon))^{-1} \\
&= R^{-1} O(\epsilon)(1 - O(\epsilon)) + R^{-1} (1 + O(\epsilon)) \\
&= R^{-1} (1 + O(\epsilon)), \qquad \text{(E.8)}
\end{aligned}$$

which shows that the largest contribution comes from the curvature melting term, and it is 3–4 orders of magnitude larger than the disjoining forces effect. In conclusion, the above analysis shows that the minimum temperature depression is found for ice which is as large as possible (to minimize curvature melting effect) but not close enough to the rock to cause the disjoining pressure effect to become large. This occurs for ice which is $10^{-3}R - 10^{-4}R$ away from the pore boundary, hence the pore can be considered ice-filled when we discuss the effect of pore ice on the permeability of the medium.

Bibliography

Akagawa, S., Satoh, M., Kanie, S. & Mikami, T. 2006 Effect of tensile strength on ice lens initiation temperature. ASCE.

Al-Shayea, N.A. 2004 Effects of testing methods and conditions on the elastic properties of limestone rock. *Engineering geology* **74** (1-2), 139–156.

Arenson, L.U., Azmatch, T.F., Sego, D.C. & Biggar, KW 2008 A new hypothesis on ice lens formation in frost-susceptible soils. In *Proceedings of the Ninth International Conference on Permafrost, Fairbanks, Alaska, June 29–July 3, 2008*.

Atkinson, B.K. 1984 Subcritical crack growth in geological materials. *Journal of Geophysical Research* **89** (B6), 4077–4114.

Atkinson, BK & Rawlings, RD 1981 Acoustic emission during stress corrosion cracking in rocks. *Richards, PG (Ed.), Earthquake prediction* pp. 605–616.

Battle, WRB 1960 Temperature observations in bergschrunds and their relationship to frost shattering. *Norwegian cirque glaciers* **4**, 83–95.

Bear, J. 1988 *Dynamics of fluids in porous media*. Dover publications.

Center, Hilton Pond 2000 Frost heave.

Charles, RJ 1958 Static fatigue of glass. i. *Journal of Applied Physics* **29** (11), 1549–1553.

Davis, S.H. 2001 *Theory of solidification*. Cambridge Univ Pr.

Embleton, C. & King, C.A. 1975 SERIES TITLE: YEAR: 1975 .

Everett, D.H. 1961 The thermodynamics of frost damage to porous solids. *Transactions of the Faraday Society* **57**, 1541–1551.

Faraday, M. 1859 Note on regelation. *Proceedings of the Royal Society of London* **10**, 440–450.

Fowler, AC 1989 Secondary frost heave in freezing soils. *SIAM Journal on Applied Mathematics* pp. 991–1008.

Fowler, A.C. & Krantz, W.B. 1994 A generalized secondary frost heave model. *Siam Journal on Applied Mathematics* pp. 1650–1675.

Freiman, SW 1984 Effects of chemical environments on slow crack growth in glasses and ceramics. *Journal of Geophysical Research* **89** (B6), 4072–4076.

Fukuda, M. 1983 The pore water pressure profile in porous rocks during freezing. In *Proceedings. Fourth International Conference on Permafrost. National Academy Press, Washington, DC*, , vol. 322, p. 327.

de Gennes, P.G. 1985 Wetting: statics and dynamics. *Reviews of Modern Physics* **57** (3), 827.

Gilpin, R.R. 1979 A model of the "liquid-like"layer between ice and a substrate with applications to wire regelation and particle migration. *J. Colloid Interface Sci* **68**, 235–251.

Gilpin, R.R. 1980 A Model for the Prediction of Ice Lensing and Frost Heave in Soils. *Water Resources Research* **16** (5).

Graham, J. & Houlsby, GT 1983 Anisotropic elasticity of a natural clay. *Geotechnique* **33** (2), 165–180.

Hallet, B., Walder, JS & Stubbs, CW 1991 Weathering by segregation ice growth in microcracks at sustained subzero temperatures: verification from an experimental study using acoustic emissions. *Permafrost and Periglacial Processes* **2** (4), 283–300.

Katz, O., Reches, Z. & Roegiers, JC 2000 Evaluation of mechanical rock properties using a schmidt hammer. *International Journal of Rock Mechanics and Mining Sciences* **37** (4), 723.

Keeble, AB 1971 Freeze-thaw cycles and rock weathering in alberta. *Albertan Geogr* **7**, 34–42.

Kessler, MA & Werner, BT 2003 Self-organization of sorted patterned ground. *Science* **299** (5605), 380.

Konrad, J.M. & Ayad, R. 1997 A idealized framework for the analysis of cohesive soils undergoing desiccation. *Canadian Geotechnical Journal* **34** (4), 477–488.

Lautridou, JP & Ozouf, J.C. 1982 Experimental frost shattering. *Progress in Physical Geography* **6** (2), 215.

Lawler, DM 1988 A bibliography of needle ice. *Cold Regions Science and Technology* **15** (3), 295–310.

Lawn, B.R. 1993 *Fracture of brittle solids*. Cambridge Univ Pr.

Matsuoka, N. & Murton, J. 2008 Frost weathering: recent advances and future directions. *Permafrost and Periglacial Processes* **19** (2), 195–210.

McGreevy, JP 1981 Some perspectives on frost shattering. *Progress in Physical Geography* **5** (1), 56.

McGreevy, JP & Whalley, WB 1985 Rock moisture content and frost weathering under natural and experimental conditions: a comparative discussion. *Arctic and Alpine Research* **17** (3), 337–346.

Mellor, M. 1970 Phase composition of pore water in cold rocks. *Tech. Rep.*. DTIC Document.

Mizusaki, T. & Hiroi, M. 1995 Frost heave in He. *Physica B: Physics of Condensed Matter* **210** (3-4), 403–410.

Murton, J.B., Peterson, R. & Ozouf, J.C. 2006 Bedrock fracture by ice segregation in cold regions. *Science* **314** (5802), 1127.

O'Neill, K. & Miller, R.D. 1985 Exploration of a rigid ice model of frost heave. *Water Resources Research* **21** (3), 281–296.

Penner, E. 1986 Aspects of ice lens growth in soils. *Cold regions science and technology* **13** (1), 91–100.

Potts, A.S. 1970 Frost action in rocks: some experimental data. *Transactions of the Institute of British Geographers* pp. 109–124.

Raviv, U. & Klein, J. 2002 Fluidity of Bound Hydration Layers.

Reif, F. 1965 *Fundamentals of Statistical and Thermal Physics (McGraw-Hill Series in Fundamentals of Physics)*. McGraw-Hill Science/Engineering/Math.

Rempel, AW, Wettlaufer, JS & Worster, MG 2001 Interfacial premelting and the thermomolecular force: Thermodynamic buoyancy. *Physical Review Letters* **87** (8), 88501.

Rempel, A.W., Wettlaufer, JS & Worster, M.G. 2004 Premelting dynamics in a continuum model of frost heave. *Journal of Fluid Mechanics* **498**, 227–244.

Rice, J.R. 1968 Mathematical analysis in the mechanics of fracture. *Fracture: an advanced treatise* **2**, 191–311.

Savitski, AA & Detournay, E. 2002 Propagation of a penny-shaped fluid-driven fracture in an impermeable rock: asymptotic solutions. *International journal of solids and structures* **39** (26), 6311–6337.

Schmidt, R.A. 1976 Fracture-toughness testing of limestone. *Experimental Mechanics* **16** (5), 161–167.

Schutter, Paul De 2004 Pingos. `http://ougseurope.org/rockon/surface/pingos.asp`.

Segall, P. 1984 Rate-dependent extensional deformation resulting from crack growth in rock. *Journal of Geophysical Research* **89** (B6), 4185–4195.

Sneddon, I.N. 1951 *Fourier Transformations*. McGraw-Hill.

Sneddon, I.N. & Lowengrub, M. 1969 *Crack problems in the classical theory of elasticity*. Wiley New York.

SnowCrystals.com 2011 Physical properties of ice. `http://www.its.caltech.edu/~atomic/snowcrystals/ice/ice.htm`.

Spence, D.A. & Sharp, P. 1985 Self-Similar Solutions for Elastohydrodynamic Cavity Flow. *Proceedings of the Royal Society of London. Series A, Mathematical and Physical Sciences (1934-1990)* **400** (1819), 289–313.

Style, R.W., Peppin, S.S.L., Cocks, A.C.F. & Wettlaufer, J.S. 2011 Ice-lens formation and geometrical supercooling in soils and other colloidal materials. *Physical Review E* **84** (4), 041402.

Taber, S. 1929 Frost heaving. *Journal of Geology* **37** (5), 428–461.

Taber, S. 1930 The mechanism of frost heaving. *Journal of Geology* **38**, 303–317.

Taber, S. 1950 Intensive frost action along lake shores [new york]. *American Journal of Science* **248** (11), 784.

Telford, JW & Turner, JS 1963 The motion of a wire through ice. *Philosophical Magazine* **8** (87), 527–531.

Tharp, TM 1983 A fracture mechanics analysis of frost wedging. *Geological Society of America Abstracts with Pro-grams* **15**, 705.

Tyndall, J. 1858 On some physical properties of ice. *Philosophical Transactions of the Royal Society of London* **148**, 211–229.

Vignes-Adler, M. 1977 On the origin of the water aspiration in a freezing dispersed medium. *J. Colloid Interface Sci* **60** (1), 162–171.

Walder, J.S. & Hallet, B. 1985 A theoretical model of the fracture of rock during freezing. *Bulletin of the Geological Society of America* **96** (3), 336–346.

Washburn, A.L. 1980 Geocryology: a survey of periglacial processes and environments .

Watanabe, K. 2002 Relationship between growth rate and supercooling in the formation of ice lenses in a glass powder. *Journal of crystal growth* **237**, 2194–2198.

Watanabe, K. & Flury, M. 2008 Capillary bundle model of hydraulic conductivity for frozen soil. *Water Resour. Res* **44**, W12402.

Watanabe, K. & Mizoguchi, M. 2000 Ice configuration near a growing ice lens in a freezing porous medium consisting of micro glass particles. *Journal of Crystal Growth* **213** (1), 135–140.

Watanabe, K., Mizoguchi, M., Ishizaki, T. & Fukuda, M. 1997 Experimental study on microstructure near freezing front during soil freezing. *Transactions of the Japanese Society of Irrigation, Drainage and Reclamation Engineering* pp. 53–58.

Website, AA Ireland 2011 Potholes. `http://blog.aaireland.ie/index.php/2011/03/28/uncategorized/sign-our-po%thole-petition-here`.

Wettlaufer, JS & Worster, MG 1995 Dynamics of premelted films: frost heave in a capillary. *Physical Review E* **51** (5), 4679.

Wettlaufer, J.S. & Worster, M.G. 2006 Premelting Dynamics. *Annual Review of Fluid Mechanics* **38**, 427.

Wiederhorn, SM & Bolz, LH 1970 Stress corrosion and static fatigue of glass. *Journal of the American Ceramic Society* **53** (10), 543–548.

Wiman, S. 1963 A preliminary study of experimental frost weathering. *Geografiska annaler* **45** (2/3), 113–121.

Worster, MG 2000 *Perspectives in Fluid Dynamics – a Collective Introduction to Current Research*, chap. Solidification of Fluids, pp. 393–446. CUP.

Zhu, D.M., Vilches, O.E., Dash, J.G., Sing, B. & Wettlaufer, J.S. 2000 Frost Heave in Argon. *Physical Review Letters* **85** (23), 4908–4911.